UNIVERSITY of CALIFORNIA
Santa Barbara

Deformation of Polymer Composites in Force Protection Systems

A Dissertation submitted in partial satisfaction of the
requirements for the degree

Doctor of Philosophy
In
Materials

By

Oshin Nazarian

Committee in charge:

Professor Frank W. Zok, Chair
Professor Robert M. McMeeking
Professor Matthew R. Begley
Professor G. Robert Odette
Professor Thomas Mackin

June 2014

The dissertation of Oshin Nazarian is approved.

_____

Professor Robert M. McMeeking

_____

Professor Matthew R. Begley

_____

Professor G. Robert Odette

_____

Professor Thomas Mackin

_____

Professor Frank W. Zok, Committee Chair

March 2014

Deformation of Polymer Composites in Force Protection Systems

Oshin Nazarian

Curriculum Vitæ

Oshin Nazarian

Education

2002-2006	B.S. in Physics University of California Santa Barbara, California
2007-2014	Ph.D. in Materials University of California Santa Barbara, California

Publications

O. Nazarian, F. W. Zok. Constitutive model for the shear response of Dyneema® fiber composites. *Submitted, Composites Part A.*

O. Nazarian, F.W. Zok, M. R. Begley. Selecting protective materials for mitigating brain injury during blunt impact. *Submitted, Journal of Impact Engineering.*

O. Nazarian, F. W. Zok. Shear-dominated dynamic behavior of a cross-ply Dyneema® composite. *In preparation.*

O. Nazarian, F.W. Zok, Composite systems for mitigating brain injury during blunt impact. *In preparation.*

Abstract

Deformation of Polymer Composites in Force Protection Systems

by

Oshin Nazarian

Systems used for protecting personnel, vehicles and infrastructure from ballistic and blast threats derive their performance from a combination of the intrinsic properties of the constituent materials and the way in which the materials are arranged and attached to one another. The present work addresses outstanding issues in both the intrinsic properties of high-performance fiber composites and the consequences of how such composites are integrated into force protection systems. One aim is to develop a constitutive model for the large-strain intralaminar shear deformation of an ultra-high molecular weight polyethylene (UHMWPE) fiber-reinforced composite. To this end, an analytical model based on a binary representation of the constituent phases is developed and validated using finite element analyses. The model is assessed through comparisons with experimental measurements on cross-ply composite specimens in the $\pm 45^{\circ}$ orientation. The hardening behavior and the limiting tensile strain are attributable to rotations of fibers in the plastic domain and the effects of these rotations on the

internal stress state. The model is further assessed through quasi-static punch experiments and dynamic impact tests using metal foam projectiles. The finite element model based on this model accurately captures both the back-face deflection-time history and the final plate profile (especially the changes caused by fiber pull-in).

A separate analytical framework for describing the accelerations caused by head impact during, for example, the secondary collision of a vehicle occupant with the cabin interior during an external event is also presented. The severity of impact, characterized by the Head Injury Criterion (HIC), is used to assess the efficacy of crushable foams in mitigating head injury. The framework is used to identify the optimal foam strength that minimizes the HIC for prescribed mass and velocity, subject to constraints on foam thickness. The predictive capability of the model is evaluated through comparisons with a series of experimental measurements from impacts of an instrumented headform onto several commercial foams. Additional comparisons are made with the results of finite element simulations. An analytical model for the planar impact of a cylindrical mass on a foam is also developed. This model sets a theoretical bound for the reduction in HIC by utilizing a "plate-on-foam" design. Experimental results of impact tests on foams coupled with stiff composite plates are presented, with comparisons to the theoretical limits predicted by the analytical model. Design maps are developed from the analytical models, illustrating the variations in the HIC with foam strength and impact velocity.

Contents

List of Figures

List of Tables

Chapter 1

Introduction

1.1 Background

Systems used for protecting personnel, vehicles and infrastructure from ballistic and blast threats derive their performance from a combination of: (i) the intrinsic properties of the constituent materials (e.g. strength, stiffness, ductility); and (ii) the way in which the materials are arranged spatially and attached to one another. For instance, armors used for protecting military vehicles from ballistic threats typically consist of multiple layers of ceramics, metals and fiber composites. The ceramic is placed at or near the impacting surface; its high hardness serves to blunt an incoming projectile and spread the impact forces over larger areas. Layers of metals or fiber composites are placed at the back of the armor in order to "catch" the debris from the damaged ceramic and prevent further penetration of the projectile. Alternative strategies are required to protect against blast loads that accompany, for example, a detonated improvised explosive device (IED). Personnel within affected military vehicles are protected from the transmitted stress waves through intermediate systems with relatively high compliance and high energy-absorption capability. The present study addresses outstanding issues

in both the intrinsic properties of high-performance fiber composites and the consequences of how such composites are integrated into force protection systems.

One of the principal classes of materials of interest here are composites based on ultra-high molecular weight polyethylene (UHMWPE) in soft polymer matrices. The selection of these fibers stems from the combination of high strength and modulus along with low mass density. For example, the Dyneema® SK76 UHMWPE fiber, manufactured by DSM Dyneema, exhibits mechanical properties that are comparable to or better than those of aramid fibers such as Kevlar®, with a density that is about 40% lower. Additionally, these fibers can be repeatedly bent without loss in strength and do not exhibit a ductile-to-brittle transition even at cryogenic temperatures. Dyneema® fibers are also cut-, tear-, and abrasion-resistant and are not susceptible to water absorption (unlike other polymer fibers). Because of these properties, Dyneema® fibers are used not only in force prtection systems but also in cut-resistant gloves, ropes, fishing lines, motorcycle safety equipment and high-performance sports apparel.

One metric that has proved to be useful in ranking the ballistic performance of reinforcing fibers is the so-called Cunniff parameter [1,2]. It is defined by:

$$C = \left(\frac{\sigma_u \cdot \varepsilon_u}{2\rho_f} \sqrt{\frac{E_f}{\rho_f}}\right)^{1/3} \tag{1.1}$$

where σ_u is the ultimate tensile strength, ε_u is the tensile failure strain, ρ_f is mass density, and E_f is Young's modulus. The parameter represents the product of the specific toughness (*i.e.*, the area under the tensile stress-strain curve divided by density) and the elastic wave speed. High values of each of these two parameters separately are

desirable in ballistic applications, so combining them in this manner is appealing. The specific toughness of various fibers is plotted on Figure 1.1 as a function of the extensional wavespeed in the fiber. The dashed lines on this material map represent fibers with an equivalent value of C. On this basis, the polyethylene fibers used for reinforcing the Dyneema® composites (e.g. SK75 and SK76) emerge as the preeminent choices among all fibers that are commercially available today.

One proposed armor design that incorporates Dyneema® composites is shown in Figure 1.2. Here, hard prismatic tiles of alumina are placed in the voids of a corrugated cellular panel extruded from a ductile aluminum alloy ($Al6061-T6$). Subsequently, the structure is wrapped in a $[0/90\,°]$ layup of unidirectional laminae comprising Dyneema® SK76 fibers. In this design, damaged ceramic elements are isolated from their neighbors by the Al members and the Dyneema "over-wrap", improving the survivability of the structure beyond a single impact event. Use of the fiber composite in this manner has been shown to increase the ballistic limit of the structure by 85%, as shown in Figure 1.3 [3].

Interestingly, Dyneema® composites are extremely anisotropic. When loaded in tension along one of the fiber directions, their response is dominated by the fibers, with little contribution from the soft matrix, and hence they exhibit high strength and failure strain. Some representative test results are plotted on Figure 1.6. In contrast, because of the presence of a soft matrix and the inherent anisotropy of heavily drawn fibers, the inter- and intra-laminar strengths are very low. Results for interlaminar shear loading are shown in Figure 1.7. The degree of anisotropy, characterized by the ratio of the

tensile strength to the shear strength, is about 400: about an order of magnitude greater than that of other fiber composites. One of the principal goals of the present study is to develop a better understanding of the mechanics of shear deformation of cross-ply Dyneema® composites. This understanding is expected to aid in the design of armor systems that attempt to exploit the desirable characteristics of Dyneema composites.

Additional issues arise in the design of systems that are intended to protect occupants in military vehicles during an IED event against the secondary impact of the occupants with the cabin interior. Here the threat of head injury due to blunt impact is a key consideration. Protective systems for this type of impact are based on open-celled viscoelastic foams [4–9]. These systems are designed to reduce the acceleration of the head by spreading the impact event over a relatively long period of time. Their effectiveness is limited largely by constraints on the allowable foam thickness in the cabin interior.

Studies performed over the past half-century have revealed strong correlations between various measures of impact severity based on acceleration-time histories and the degree of injury. The measures originated through impact studies on skulls of human cadavers and live animals [10]. The data were used to construct the so-called Wayne State Tolerance Curve: the locus of average acceleration and impact duration below which skull fracture would not occur. A stronger correlation of the data was obtained using other measures of impact severity, based on weighted averages of acceleration-time profiles. The first of these was the Gadd Severity Index (GSI) [11], defined by:

$$GSI = \int_0^{\bar{t}} [a(t)]^{5/2}\, dt \tag{1.2}$$

where a is deceleration in units of g (the acceleration due to gravity), t is time and $\bar{t}$ is the impact duration. Yet a stronger correlation was obtained using the Head Injury Criterion (HIC), defined by [10–14]:

$$HIC = \max_{t_1,t_2}\left\{\left[\frac{\int_{t_1}^{t_2} a(t)dt}{t_2-t_1}\right]^{5/2} (t_2 - t_1)\right\} \tag{1.3}$$

where t_2 and t_1 are the two times that maximize the quantity in $\{...\}$, subject to the constraint that the two times not differ from one another by more than a prescribed amount, t_c (typically 15 ms) (Figure 1.4). The HIC is essentially a product of a power-weighted time-averaged acceleration and the corresponding time duration. Because of the weightings, the HIC is more sensitive to acceleration than duration time. The time restriction reflects the fact that low acceleration levels over extended periods of time pose low risk of injury. The connections between the *HIC* value and the probability of sustaining a head injury of specified severity are illustrated in Figure 1.5 [15,16]. A value of 1400 corresponds to a 50% probability of producing a life-threatening head injury.

The Head Injury Criterion (HIC) has been adopted by the US National Highway Traffic Safety Administration [17] and is currently the standard used by the US Insurance Institute for Highway Safety for rating automobile safety in collisions. It is also used by manufacturers of motorcycle helmets and protective equipment for sporting applications (e.g. football, hockey, soccer, snow boarding [18,19] and is employed in

assessing head injury risk potential of various surfaces used on playgrounds [20,21] and for cheerleading [22].

1.2 Objectives and outline

The overarching goal of this work is two-fold: (i) to advance the understanding of the deformation mechanics governing the behavior of Dyneema® fiber composites and (ii) to develop tools that can aid in the design of composite protection systems. Two model problems have been identified. The first is the distributed pressure-load exerted on a catch-plate in an armor system that has been impacted by a projectile. The pertinent time scale of these events is on the order of hundreds of microseconds. The second model problem is that of blunt impact of a human head on a rigid target. Here the impact persists for time periods on the order of tens of milliseconds. In both scenarios, fiber composites prove to be very beneficial.

The dissertation is organized in the following manner. The following two chapters address the mechanics of deformation of Dyneema® fiber composites. Chapter 2 focuses on the tensile response of cross-ply composites loaded in the $[\pm 45^{\circ}]$. In parallel, an analytical model based on a binary representation of the constitutent phases is presented and validated using finite element analyses.

In Chapter 3, the model is extended to encompass other types of loading and dynamic effects. First, quasi-static punch tests on clamped plates are used to validate the predictive capability of the model presented in Chapter 2. The nature of the clamped boundaries prove to play an important role in the manner in which material is drawn

into the punch region. Next, tests based on high velocity impact of similarly-clamped plates by metal foam projectiles are used to identify the dynamic effects operative in punch-type loadings. Finite element simulations are again used for assessing features of the material model.

Chapters 4 focuses on the design of systems for mitigating head injuries during blunt impact. The Head Injury Criterion (HIC) underpins this work. An analytical model for predicting the accelerations transferred to a human head during moderate-velocity impacts is presented. The minimum values for the HIC along with the optimal foam strength are presented for both planar and spherical impacts. Finite element simulations are used to validate the analytical model.

Building on the analyses of the preceding chapter, Chapter 5 presents the results of an experimental study on the effects of a composite plate placed on top of a protective foam in further mitigating the HIC value for a prescribed impact velocity. These results are compared to those on foam-only systems. The benefits associated with the plates are rationalized on the basis of the load distributions at the impact site and the resulting acceleration-time history experienced by the impacting head.

Lastly, Chapter 6 summarizes the key findings and presents future opportunities for research.

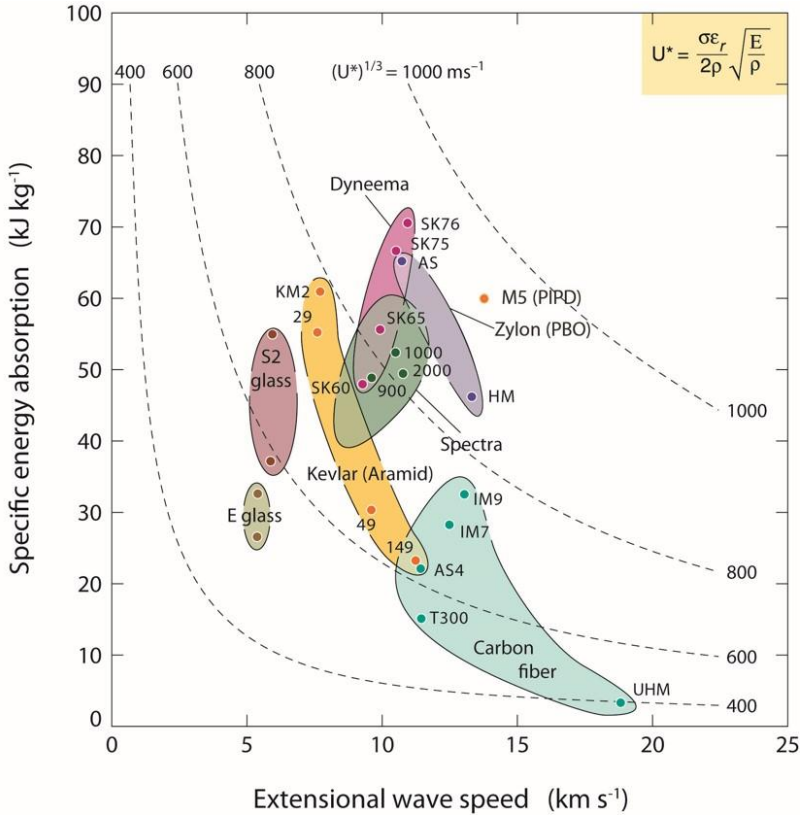

Figure 1.1: The specific energy absorption of commercially available fibers plotted as a function of extensional wave speed. Dashed lines represent equivalent value of the Cunniff parameter. (Adapted from [3])

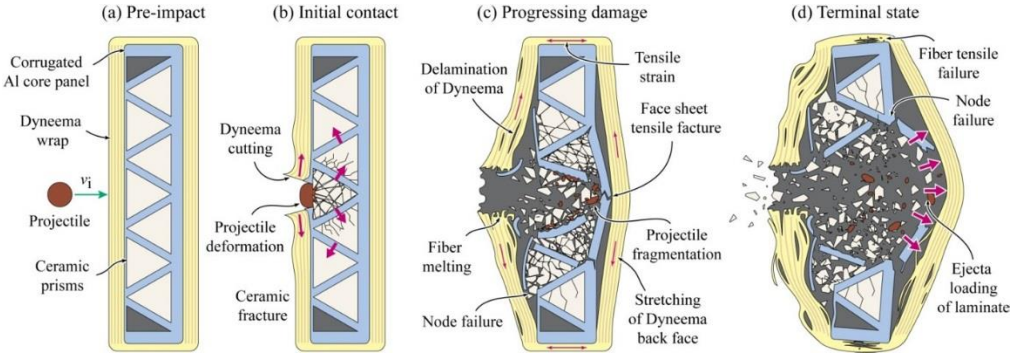

Figure 1.2: Schematic of the response of a (a) composite armor system subject to impact by a high-speed projectile at a velocity v_i. The response is characterized by (b) cutting of the fibers on the front face and deformation of the projectile on the surface of the ceramic prism followed by (c) pulverization of the panel components. This ultimately results in (d) a distributed load on the back face of the Dyneema® laminate [3].

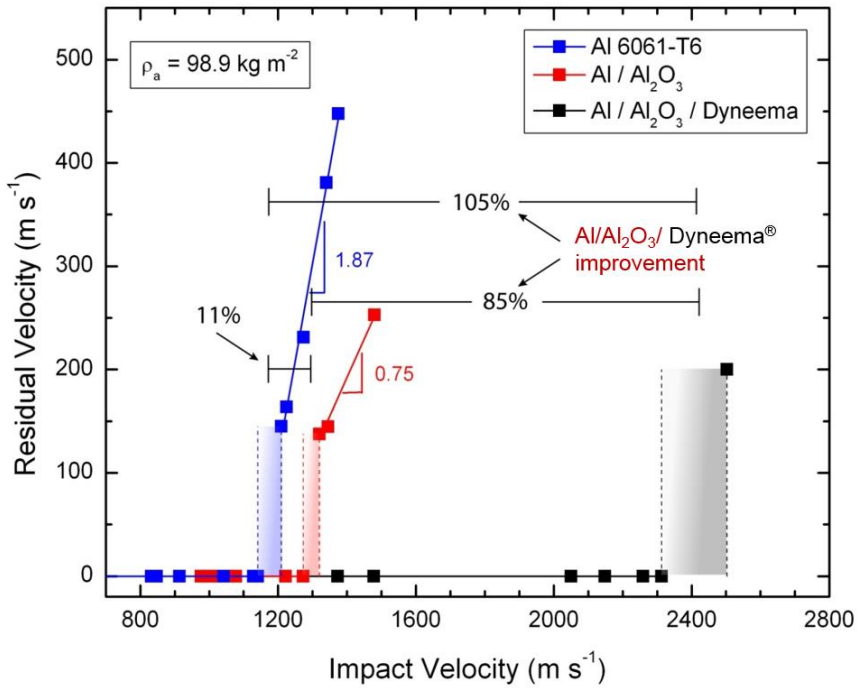

Figure 1.3: The residual velocity of spherical steel projectiles after impact with three different armor structures of equivalent density as a function of impact velocity. Estimates of the ballistic limit of the structures is highlighted by the shaded regions. (Adapted from [3])

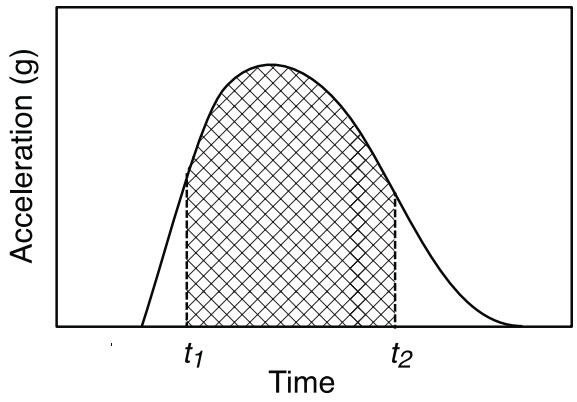

Figure 1.4: Schematic of acceleration-time profile and the two times bounding the calculation of the *HIC* [23,24].

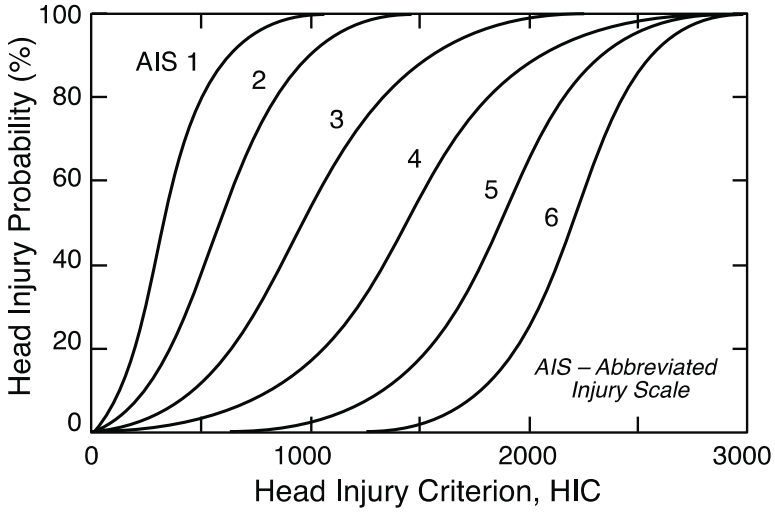

Figure 1.5: Effects of HIC on probability of sustaining head injuries of varying severity (from 1 to 6 on the Abbreviated Injury Scale). The Abbreviated Injury Scale was developed by the Association for the Advancement of Automotive Medicine. On this scale, 1 is minor and 6 is fatal. (Adapted from [15])

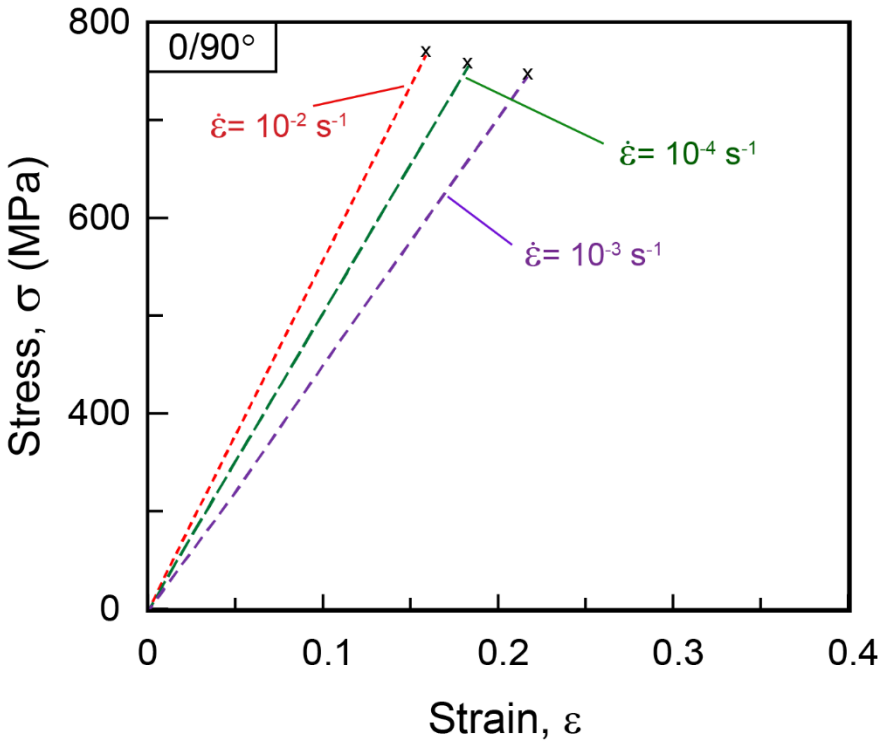

Figure 1.6: Schematic of the tensile stress-strain response of Dyneema® HB26 laminates at various low strain rates. (Adapted from [25])

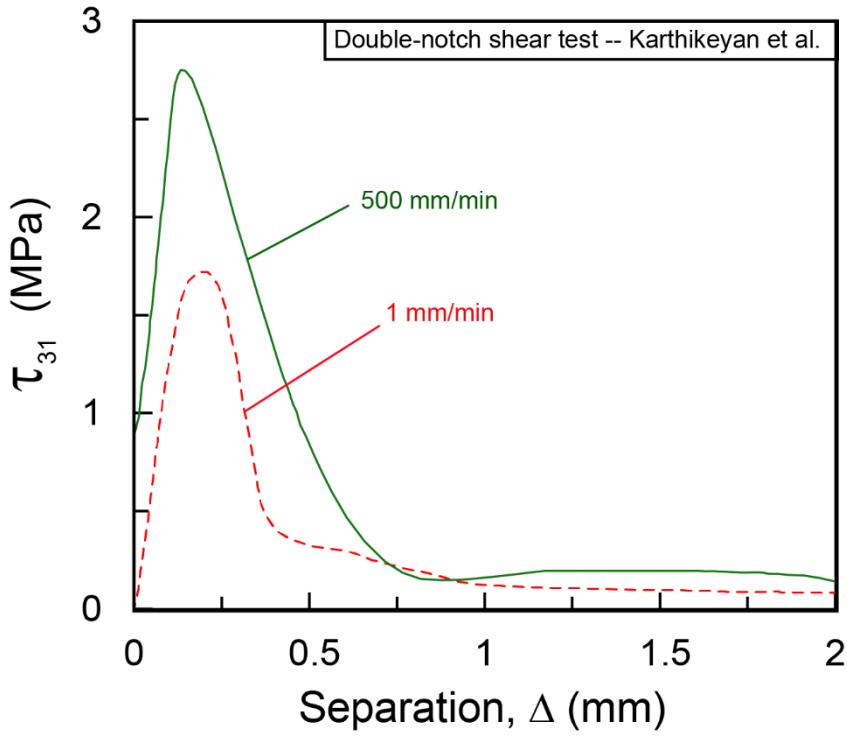

Figure 1.7: The measured inter-laminar shear stress, τ_{31}, as a function of shear displacement, Δ, for Dyneema® HB26. (Adapted from [26])

Chapter 2

In-plane shear behavior of Dyneema® fiber composites

2.1 Introduction

The performance of Dyneema® composites in absorbing blast energy depends heavily on the ultimate tensile strength and failure strain of the underlying fibers. However, recent studies on the soft-impact performance of Dyneema® HB26 and other fiber composites have demonstrated an important role of the matrix properties. Karthikeyan *et al*. [26,27] performed comparisons of the dynamic responses of beams and plates made from two grades of carbon fiber reinforced plastics (CFRP) – one with a cured matrix and one with an uncured matrix – and two grades of Dyneema® composites (HB26 and HB50), both containing the same fibers but with different matrices. They found that, for each pair of materials, the one with the lower matrix yield strength outperformed the other. They therefore concluded that the Cunniff parameter alone cannot distinguish and rank these materials (since the parameter does not depend on the matrix

shear strength).

Our own work in this area has suggested an important role of the intralaminar shear strength of Dyneema® composites under impact loading. Figure 2.1 shows an example of a Dyneema® [0°/90°] HB26 plate that had been situated behind a 6 mm-thick alumina tile (Corbit 98, Bitossi Industries) during impact by a 7.62 mm-diameter steel projectile at 1200 m/s. The two plates had been clamped snugly together in a circular fixture with a 75 mm-diameter open window. The images include both *in situ* observations of the back face of the HB26 plate taken with a high-speed video camera (in (a)) as well as post-test photographs of the same plate in plan and side views after removal from the test fixture (in (b)). The extensive bulging of the plate had been accommodated largely through shear deformation parallel to the fiber directions, as manifested in distortion of fiducial lines on the plate surface as well as extensive pull-in of material from the distal regions of the plate. (Measurements of the total length of fiducial lines show that the plate had undergone minimal stretching in either of the two fiber directions.) The peak nominal shear strain exceeds 0.2.

As discussed in Chapter 1, considerable research has been conducted on Dyneema® SK76 fibers and composites containing these fibers (Figure 1.6). Here, the on-axis response is dominated by the fibers. Because of the extremely low strength and stiffness of the matrix in comparison to the fibers, little insight is obtained from these tests regarding the contribution of the matrix to the composite behavior. Instead, measurements of the off-axis response, as manifested, for example, in the tensile response in cross-ply laminates in the ±45° orientation, are necessary.

The objectives of this chapter are twofold: (i) to develop an improved understanding of the mechanics of large-strain deformation of Dyneema® composites under intralaminar shear loading and (ii) to utilize this understanding in developing an elastic-plastic constitutive model for use in design and analysis of armors and other systems containing these composites. The experimental portion of the study presented in this chapter focuses on the quasi-static tensile response of one specific cross-ply Dyneema® composite in the [±45°] orientation. In addition to the usual instrumentation used in tensile tests, we employ 3D digital image correlation for strain mapping. We also develop an analytical model for the composite response that accounts for the large fiber rotations that accompany deformation in these tests. The analytical model is assessed through comparisons with numerical simulations based on a closely-analogous finite element model. The use of the latter model in simulating tests of the type shown in Figure 2.1 is presented in Chapter 3.

2.2 Materials and test methods

All tests were performed on samples cut from panels of Dyneema® HB26 (provided by DSM Dyneema, The Netherlands). The panels comprise 83% ultra-high molecular weight polyethylene fibers, each 17 microns in diameter, and 17% polyurethane matrix with a $[0°/90°]_{48}$ fiber lay-up. The ply thickness was 68 microns and the panel thickness was 3.3 mm. The panels had been consolidated through a proprietary hot-pressing process.

Test coupons for optical microscopy were mounted in a low-viscosity epoxy (Buehler Inc.), hand-ground down to 1200 grit SiC paper, and then polished on an automated turntable using a 1 μm colloidal alumina solution (Allied High Tech Products, Inc.). The polished sections were viewed using dark-field microscopy; this imaging mode has been found to be effective in distinguishing between the highly-crystalline fibers and the amorphous matrix [25]. A representative micrograph is shown in Figure 2.2. The majority of the fibers are evenly dispersed with a small amount of matrix material surrounding each fiber.

Uniaxial tension tests were conducted on dog-bone coupons, 13 mm wide and 50 mm long in the gauge section, in accordance with the Type-I geometry in ASTM standard D638 [28]). Rectangular coupons in the [±45°] orientation were first cut out of the panel using a band saw. These coupons were mounted between two aluminum blocks and dry-cut with a high-speed milling tool bit on a computer numerical control (CNC) mill. This procedure yielded smooth surfaces and sharp edges without fraying. Finally, in preparation for strain mapping, one of the broad faces of each test coupon was lightly misted with black spray paint (Krylon®). The resulting speckles had an average diameter of about 250 μm.

The coupons were tested in a hydraulic mechanical test system using hydraulic wedge grips. Prior to testing, the grips were aligned by clamping both ends of a steel bar and locking the grips in place. The tests were performed at a nominal strain rate of $10^{-3}\ s^{-1}$. Displacements on the painted surface were measured using a 3D digital image correlation (DIC) system (Vic-3D, Correlated Solutions, Inc.). The two principal

in-plane strains were calculated using the Vic-3D correlation software. Out-of-plane strains were estimated from the DIC out-of-plane displacement fields, assuming uniform through-thickness straining; that is, the nominal strain was calculated as the through-thickness displacement on one face divided by half the plate thickness. The effective magnification of the images ranged from 25 to 40 pixels/mm. The subset size used for correlation was 31–40 pixels and the step size was selected to be about 10% of the subset size [29]. Incremental correlation was used to assist in feature tracking at large plastic strains.

Strain distributions acquired by the DIC system during the experiments were processed using the computational and visualization tool Mathematica® (Wolfram Research). Line scans of the three principal strains across the samples were used to assess the uniformity of the deformation. Examinations of these scans along with full-field strain maps led to the identification of a central rectangular region within which the strains were indeed uniform. The average strain values within this region were used to characterize the global deformation response.

2.3 Test results

The nominal tensile stress-strain curves for several test coupons are shown in Figure 2.3(a). Tensile strains were taken from an average of five virtual extensometers within the gauge section of each coupon using DIC. These strains represent the global nominal tensile strain with the standard definition $\tilde{\varepsilon}_{xx} = \frac{\Delta l}{l_o}$, where l_o is an initial gauge

length and Δl is the corresponding change in that length[1]. The onset of inelasticity occurs at $\tilde{\varepsilon}_{xx} = 0.02$ at a stress $\tilde{\sigma}_{xx} = 2.2$ MPa. The initial elastic modulus is $E_{xx} = 110$ MPa. Appreciable hardening is seen up to strains of $\tilde{\varepsilon}_{xx} \approx 0.3$, with an almost-constant tangent modulus of about 50 MPa (essentially half of the initial elastic modulus). Thereafter, at strains $\tilde{\varepsilon}_{xx} > 0.3$, the tangent modulus increases by about an order of magnitude. As demonstrated below, hardening is attributable largely to the fiber rotations that accompany large deformations and the associated changes in stress state within the matrix. Failure occurs consistently at a critical nominal tensile strain of 0.37±0.01

Figure 2.4 shows representative line scans of the two transverse strains, $\tilde{\varepsilon}_{yy}$ and $\tilde{\varepsilon}_{zz}$, across the sample width at various axial strain levels ($\tilde{\varepsilon}_{yy}$ = 0.05–0.35). The strains exhibit edge effects which manifest at strains $\tilde{\varepsilon}_{xx} > 0.15$ but remain largely confined to the outer 15-20% of the sample width. In light of these variations, the strains reported subsequently are based on values averaged over a central rectangular region comprising about 75% of the specimen width.

The two transverse strains (averaged accordingly) are plotted against axial strain in Figure 2.5. The in-plane component, $\tilde{\varepsilon}_{yy}$, is roughly proportional to the axial strain at

[1] Following convention, the true strains and true stresses are denoted as ε_{ij} and σ_{ij}, respectively, and the corresponding deviatoric components e_{ij} and s_{ij}; the engineering (or nominal) values are indicated with a tilde over the symbols. Furthermore, the global Cartesian coordinate system is denoted as (*x*,*y*,*z*) where *x* is aligned with the tensile loading direction, *y* is the in-plane transverse direction, and *z* is the through-thickness direction. The local coordinates within an individual lamina are denoted (*1*,*2*,*3*), where *1* is aligned with the fiber direction.

strains $\tilde{\varepsilon}_{xx} \leq 0.2$, with a "plastic" Poisson's ratio of $v_{12}^{p} \approx 1.25$. In contrast, over the same strain range, the out-of-plane strain $\tilde{\varepsilon}_{zz}$ is of opposite sign, yielding a "plastic" Poisson's ratio $v_{13}^{p} \approx$ -1.5. The magnitudes of both v_{12}^{p} and v_{13}^{p} increase with applied strain; that is, $\tilde{\varepsilon}_{yy}$ becomes increasingly more negative and $\tilde{\varepsilon}_{zz}$ becomes more positive with increasing $\tilde{\varepsilon}_{xx}$. Additionally, the volumetric strain (plotted in Figure 2.5(b)) is initially negligible but then begins to rise at a nominal axial strain of about 0.1 and attains values as high as 0.3 at fracture. This trend suggests the development of micro-structural damage.

Images of a fractured tensile specimen and transverse cross-sections taken at various positions along its gauge length relative to the fracture location are shown in Figure 2.6. Fracture occurs via both extensive shear deformation within the plies and, because of ply symmetry, delamination between plies, with no apparent fiber fracture. Sections within the fracture zone reveal the delaminations. Away from the fracture zone, there is some evidence of delamination near the edges; but the density of these delaminations and their penetration depth appear to be relatively small in comparison to the total interlaminar area. Higher magnification optical examinations were unable to reveal any finer-scale damage, possibly a consequence of smearing of the soft matrix during polishing. Nevertheless, the measured volumetric strains strongly suggest that damage within the matrix is likely substantial.

2.4 Analytical model

2.4.1 Preliminaries

Here an analytical model for the elastic-plastic response of the HB26 composite loaded in tension in the ±45° orientation is presented. For this purpose, a binary representation of the constituent phases is adopted, closely analogous to that employed elsewhere [30]. The fibers are treated as a series of line-spring elements aligned with the fiber directions. These elements are embedded in an *effective medium* with properties affected by (but not equal to) those of the matrix. The latter properties incorporate all of the off-axis composite properties (e.g. strengths and stiffness in shear and transverse tension) as well as the axial composite stiffness and strength that are not attributable to the fibers. No attempt is made to predict the effective medium properties on the basis of the fundamental constituent properties; instead, they are inferred from them comparisons of predicted and measured responses.

It is assumed that the fibers are axially inextensible. (Finite element simulations presented in Section 2.5.3 demonstrate that elastic straining of the fibers has negligible effect on the tensile response in the orientation of interest). Three constitutive laws for the effective medium are considered. Two are based on Mises-type elastic-plastic behavior: one being perfectly-plastic and the other with linear hardening after yield. The third is based on the linear Drucker-Prager yield criterion with associated flow and no hardening. As usually done in these types of analyses, the strain increments are partitioned into elastic and plastic components. The finite element simulations presented in

Section 2.5.3 demonstrate that the analytical model predictions are highly accurate.

The model follows naturally from the observation that, with stiff fibers in a ±45° lay-up, a finite tensile strain leads to rotations of the two sets of fibers towards the tensile loading direction. Furthermore, the in-plane *strain* state in the effective medium is governed entirely by the degree of such rotations; the functional relationship between strains and rotations are readily ascertained from geometry. With knowledge of the strain state and an assumed form for the constitutive law of the effective medium, the stresses acting on the effective medium and the fibers are obtained. Then, upon performing an appropriate averaging, the composite stress-strain response is ascertained.

2.4.2 Elastic response

The small-strain elastic response is obtained using classical laminate theory, with a slight modification to account for the binary representation of the constituents. Specifically, since the fibers are treated as line-springs with no cross-sectional area, the axial and transverse Young's moduli of a single lamina are given by [30,31]:

$$E_1 = V_f \cdot E_f + E_{em} \tag{2.1}$$

$$E_2 = E_{em} \tag{2.2}$$

where V_f is the volume fraction of fibers, E_f is the fiber modulus, and E_{em} is the modulus of the effective medium. (Note that, in contrast to conventional composite models, the term containing the effective medium modulus in Eqn. (2.1) is *not* weighted by the matrix volume fraction.) Details of the analysis are contained in Appendix A. The key

result, for the Young's modulus of the laminate measured in the *x*-direction (with fibers in the ±45° orientation), is

$$E_x = \frac{V_f E_f + 2(1+v)E_{em}}{\frac{(1+v)V_f E_f}{2E_{em}} + (2+v)} \tag{2.3}$$

When $E_f \gg E_{em}$ (as it is in the Dyneema® composites), Eqn. (2.3) reduces to:

$$E_x \approx \frac{2E_{em}}{(1+v)} \tag{2.4}$$

Eqn. (2.4) has been used to infer E_{em} from the measured composite modulus, E_x, and an estimate of v. From Figure 2.3 the measured modulus is $E_x = 110 \pm 15$ MPa. Assuming that the Poisson's ratio of the effective medium is $v = 0.4$, the inferred effective medium modulus is $E_{em} = 68$ MPa. This value is employed in subsequent sections for computing the elastic strain components in the post-yielding domain.

2.4.3 The strain state

Following a straightforward analysis of the geometric changes associated with the rotation of *inextensible* fibers in an angle-ply laminate, the principal in-plane strain increments, $d\varepsilon_{\mathrm{xx}}$ and $d\varepsilon_{\mathrm{yy}}$, in the axial and transverse directions, respectively, can be expressed as:

$$d\varepsilon_{\mathrm{xx}} = -\tan(\theta)\ d\theta \tag{2.5a}$$

$$d\varepsilon_{\mathrm{yy}} = \cot(\theta)\ d\theta \tag{2.5b}$$

Upon integration, the total (true) strains become:

$$\varepsilon_{xx} = \ln\left[\frac{\cos(\theta)}{\cos(\theta_o)}\right] \tag{2.6a}$$

$$\varepsilon_{yy} = \ln\left[\frac{\sin(\theta)}{\sin(\theta_o)}\right] \tag{2.6b}$$

where θ_o and θ are the initial and current fiber angles, respectively. Combining these results leads to a direct relationship between the two strains, notably:

$$\varepsilon_{yy} = \ln\left[\frac{\sin\left(\cos^{-1}[\cos(\theta_o)\cdot\exp(\varepsilon_{xx})]\right)}{\sin(\theta_o)}\right] \tag{2.7}$$

This relationship is *independent of the constitutive law for the effective medium*.

When the deformation is volume-conserving – as it would be, for example, in a rigid-plastic Mises-type solid – the through-thickness strain can be expressed in terms of the other two strains via:

$$\varepsilon_{zz} = -\left[\varepsilon_{xx} + \varepsilon_{yy}\right] = -\left[\varepsilon_{xx} + \ln\left[\frac{\sin\left(\cos^{-1}[\cos(\theta_o)\cdot\exp(\varepsilon_{xx})]\right)}{\sin(\theta_o)}\right]\right] \tag{2.8}$$

Eqns. (2.7) and (2.8) can be re-cast in terms of the *nominal* strains, $\tilde{\varepsilon}_{xx}$, $\tilde{\varepsilon}_{yy}$ and $\tilde{\varepsilon}_{zz}$, yielding:

$$\tilde{\varepsilon}_{yy} = \left[\frac{\sin\left(\cos^{-1}[\cos\theta_o\cdot(1+\tilde{\varepsilon}_{xx})]\right)}{\sin\theta_o}\right] - 1 \tag{2.9a}$$

$$\tilde{\varepsilon}_{zz} = \left[(1+\tilde{\varepsilon}_{xx})\cdot\left(\frac{\sin\left(\cos^{-1}[\cos\theta_o\cdot(1+\tilde{\varepsilon}_{xx})]\right)}{\sin\theta_o}\right)\right] - 1 \tag{2.9b}$$

The predicted variations in $\tilde{\varepsilon}_{yy}$ and $\tilde{\varepsilon}_{zz}$ with $\tilde{\varepsilon}_{xx}$ are compared with the corresponding experimental measurements in Figure 2.5. Excellent agreement is obtained for $\tilde{\varepsilon}_{yy}$ over the entire strain range (up to fracture). One inference is that the assumption that the fibers are inextensible is indeed a very good one. In contrast, although the predicted

curve of $\tilde{\varepsilon}_{zz}$ vs. $\tilde{\varepsilon}_{xx}$ exhibits features that are qualitatively consistent with the experiments, it falls somewhat below the experimental curve, especially at large strains (>0.1). The latter strain domain is the one in which dilatation is appreciable.

Further comparisons are made regarding the failure strain. From Eqn. (2.6a), the limiting nominal tensile strain – when the fibers have reached alignment with the tensile axis (θ=0°) – is $\csc\theta_o - 1 \approx 0.41$. By comparison, the measured failure strains are only slightly lower, at 0.37±0.1. This correlation re-affirms the dominant role of fiber rotation in the deformation response of these composites.

Henceforth the challenges are to (i) ascertain the effective medium and fiber stresses that are consistent with the strains imposed by the rotations and (ii) average the stresses accordingly in order to obtain the composite stress as a function of the imposed strain.

2.4.4 Effective medium stresses

Here a framework within which the effective medium stresses can be computed, subject to the strain path dictated by fiber rotation, is presented. When combined with the results in the next section, the corresponding composite tensile stress-strain relation is obtained.

In its most rudimentary form, the model is based on the assumption that the effective medium is a Mises-type solid. The yield function *f* is defined by

$$f = \sigma_e^2 - [F(e_e^p)]^2 = 0 \tag{2.10}$$

where

$$\sigma_e = \sqrt{\frac{3}{2} s_{ij} \cdot s_{ij}} \tag{2.11}$$

and

$$e_e^p = \int de_e^p = \int \sqrt{\frac{2}{3} de_{ij}^p \cdot de_{ij}^p} \tag{2.12}$$

Here σ_e and e_e^p are the equivalent stress and equivalent plastic strain, respectively; s_{ij} and e_{ij} are the components of the deviatoric stress and strain tensors, respectively; and $F(e_e^p)$ is the plastic part of the tensile stress-strain curve. (Hereafter the superscript "*em"* is dropped since the entire analysis in this section pertains *only* to the effective medium). Assuming associated flow:

$$de_{ij}^p = \lambda \frac{df}{d(s_{ij})} = \frac{3 d\sigma_e}{2 h \sigma_e} \cdot s_{ij} \tag{2.13}$$

with

$$d\sigma_e = \frac{G \; s_{ij} \cdot de_{ij}}{\sigma_e \left[\frac{1}{3} + \frac{G}{h}\right]} \tag{2.14}$$

where $h = \frac{dF}{de_e^p}$ is the post-yielding tangent modulus in a uniaxial tension test and λ is the plastic multiplier. Summing the elastic and plastic components yields the total deviatoric strain increment, de_{ij}:

$$de_{ij} = \frac{1}{2G} ds_{ij} + \frac{3 d\sigma_e}{2 h \sigma_e} \cdot s_{ij} \tag{2.15}$$

where G is the shear modulus of the effective medium. Combining the preceding results, the increment of deviatoric stress is found to be:

$$ds_{ij} = 2G\left[de_{ij} - \frac{3}{2}\frac{s_{ij}}{\sigma_e}\cdot\frac{G\ s_{kl}\cdot de_{kl}}{\sigma_e\left[\frac{h}{3}+G\right]}\right] \tag{2.16}$$

Further assuming that the effective medium is perfectly-plastic ($h = 0$), Eqn. (2.16) reduces to

$$ds_{ij} = 2G\left[de_{ij} - \frac{3}{2}\cdot\frac{s_{ij}\ s_{kl}\cdot de_{kl}}{\sigma_e^2}\right] \tag{2.17}$$

Adding the non-deviatoric components of strain and stress, the total stress increment becomes:

$$d\sigma_{ij} = ds_{ij} + \frac{1}{3}d\sigma_{kk}\cdot\delta_{ij} \tag{2.18a}$$

or $$d\sigma_{ij} = 2G\left[d\varepsilon_{ij} + \frac{v}{1-2v}d\varepsilon_{kk}\delta_{ij} - \frac{3}{2}\frac{s_{ij}s_{kl}d\varepsilon_{kl}}{\sigma_e^2}\right] \tag{2.18b}$$

where δ_{ij} is the Kronecker delta. Finally, assuming plane stress conditions ($\sigma_{zz} = 0$), the out-of-plane strain increment becomes:

$$d\varepsilon_{zz} = -\frac{d\varepsilon_{xx}\left[\frac{v}{1-2v}-\frac{3}{2}\frac{s_{zz}\cdot s_{xx}}{\sigma_e^2}\right] + d\varepsilon_{yy}\left[\frac{v}{1-2v}-\frac{3}{2}\frac{s_{zz}\cdot s_{yy}}{\sigma_e^2}\right]}{\left[\frac{v}{1-2v}-\frac{3}{2}\frac{s_{zz}\cdot s_{zz}}{\sigma_e^2}\right]} \tag{2.19}$$

and the in-plane stress increments (from (2.18(b)) are:

$$d\sigma_{xx} = 2G\left[d\varepsilon_{xx} + \frac{v}{1-2v}d\varepsilon_{kk} - \frac{3}{2}\frac{s_{xx}\ s_{kl}\cdot d\varepsilon_{kl}}{\sigma_e^2}\right] \tag{2.20a}$$

$$d\sigma_{yy} = 2G\left[d\varepsilon_{yy} + \frac{v}{1-2v}d\varepsilon_{kk} - \frac{3}{2}\frac{s_{yy}\ s_{kl}\cdot d\varepsilon_{kl}}{\sigma_e^2}\right] \tag{2.20b}$$

In this form the stress increments only depend explicitly on the current deviatoric stress,

s_{ij}, and the incremental tensile strain, $d\varepsilon_{\mathrm{xx}}$ ($d\varepsilon_{\mathrm{yy}}$ being related to $d\varepsilon_{\mathrm{xx}}$ via (2.7)). Eqns. (2.20a) and (2.20b) have been combined with (2.6a) and (2.6b) and the results integrated numerically to evaluate the effective medium stresses in terms of the total axial strain.

A typical set of results from this procedure is shown in Figure 2.7. Two features are noteworthy. First, because $d\varepsilon_{\mathrm{xx}} = -d\varepsilon_{\mathrm{yy}}$ at small strains, the two stresses are related by $\sigma_{\mathrm{xx}} = -\sigma_{\mathrm{yy}}$. That is, the effective medium is in a state of pure shear. Second, as the fiber rotations increase, both stresses decrease in value; indeed, σ_{xx} becomes negative beyond strains of about 0.16. In effect, the fiber rotations cause the stresses in the effective medium to migrate along the yield surface in the way shown by the schematic inset of this figure. Accordingly, the stress triaxiality within the effective medium becomes increasingly *negative* as the tensile strain increases: a non-intuitive and unexpected result.

Analogous results (not shown) have been obtained for effective media that exhibit linear strain hardening beyond yield. The effect of hardening on the predicted composite response below in Section 2.4.4.

2.4.5 Laminate stresses

The axial stress σ_{xx}^{lam} borne by the laminate is obtained by adding the contributions from the fibers (σ_f) and the effective medium (σ_{xx}^{em}), with the fiber contribution being resolved into the approriate direction. This process yields:

$$\sigma_{xx}^{lam} = \sigma_{xx}^{em} + V_f \cdot \sigma_f \cdot \cos^2[\cos^{-1}([\cos(\theta_o) \cdot \exp(\varepsilon_{xx})])] \tag{2.21}$$

To obtain σ_f, use is made of the fact that the net stress in the *y*-direction is identically zero; that is, the *y*-component of tension supported by the fibers, given by $V_f \cdot \sigma_f \cdot \sin^2(\theta)$, must be balanced by the compression within the effective medium elements, $-\sigma_{yy}^{em}$. This equilibrium condition yields:

$$V_f \cdot \sigma_f \cdot \sin^2(\cos^{-1}[\cos(\theta_o) \cdot \exp(\varepsilon_{xx})]) = \sigma_{yy}^{em} \tag{2.22}$$

Combining (2.21) and (2.22) gives the true axial laminate stress:

$$\sigma_{xx}^{lam} = \sigma_{xx}^{em} + \sigma_{yy}^{em} \cdot \cot^2\left[\cos^{-1}\left(\cos(\theta_o) \cdot \exp(\varepsilon_{xx})\right)\right] \tag{2.23}$$

The corresponding *nominal* stress-strain relation is readily computed by invoking volume conservation, whereupon:

$$\tilde{\sigma}_{xx}^{lam} = \frac{\sigma_{xx}^{em} + \sigma_{yy}^{em} \cdot \{\cot^2[\cos^{-1}(\cos(\theta_o) \cdot (1+\tilde{\varepsilon}_{xx}))]\}}{1+\tilde{\varepsilon}_{xx}} \tag{2.24}$$

Eqn. (2.24) in combination with (2.20a) and (2.20b) represent key results of this chapter.

The nominal stress-strain curves predicted by (2.20a), (2.20b) and (2.24) for various values of the effective medium yield stress (from 2 to 4 MPa) and the elastic modulus inferred in Section 2.4.2 along with representative experimental data are plotted on Figure 2.3(a). Although qualitatively in good agreement, the model predictions either match the experimental data well at low strains and underestimate them at high strains, or vice versa, depending on the selection of σ_o.

Additional theoretical results for a linear-hardening Mises-material with tangent

moduli h=0–30 MPa are plotted in Figure 3(b). The selection of h values was guided by previously-reported experimental measurements on the tensile response of the neat polyurethane matrix used in HB26, which reveal a post-yielding tangent modulus of 10-15 MPa [3]. To re-iterate a point made earlier in Section 2.4.1, in the way it is defined here the effective medium has properties that are strongly influenced by but not equivalent to the properties of the matrix. Thus, the post-yield tangent modulus of the effective medium is expected to be of the same order of magnitude as that measured on the neat matrix material, but may vary somewhat about this value. Here, again, the correlations between theoretical predictions and experimental measurements are mixed; the tensile response at either small or large strains can be adequately captured by varying one of the parameter values, yet the response over the entire strain range is not captured by any one of the individual cases. These discrepancies, coupled with the measured dilatational strains, are interpreted as being strong indications of microstructural damage. Such effects are addressed by using a phenomenological strain-softening constitutive law for the effective medium elements, presented below in Section 2.5.

2.5 Finite element analyses

2.5.1 The model

An assessment of the preceding analytical model was made through comparisons with finite element (FE) analyses. For consistency, the FE model was comprised of

arrays of line elements to represent the fibers, implemented as rebar elements in the Abaqus FE code. This selection was based on the understanding that, under large shear deformations, rebar elements are able to rotate and remain aligned with the element's isoparametric directions, as illustrated in Figure 2.8. Other approaches for modeling anisotropic materials, such as that based on the Hill yield condition, fail to properly capture such rotations and retain the correct orientation relationships.

The dimensions of the specimen in the finite element model were chosen to match those employed in the experiments. The specimen was modeled as a collection of 16 sheets of continuum shell elements, each containing unidirectionally-aligned rebar (line) elements at either 45° or -45° to the loading direction. The in-plane element dimensions were chosen to meet two competing criteria: (i) they must be large enough in comparison to the element thickness to prevent shear-locking, and (ii) they must be small enough to properly resolve the details of in-plane deformation. These criteria were satisfied using elements that were 1 mm x 1 mm in-plane and 100 μm through-thickness. A mesh-sensitivity study was conducted by altering the element width from 2.15 mm to 0.5 mm. The results for stresses and strains for 1 mm and 0.5 mm elements were indistinguishable from one another and thus all subsequent calculations were performed using the higher value. The thickness of the model was 1.6 mm. An out-of-plane symmetry boundary condition was implemented, thereby yielding a model that was 3.2 mm thick (essentially the same as the thickness of the actual test specimen).

The boundary conditions at the two opposing ends of the sample were chosen to reflect the conditions imposed by the wedge grips in the experiments. At one end, the

displacements in the three principal directions were prescribed to be $u_x = u_y = u_z = 0$; at the other end, they were $u_y = u_z = 0$ and $\dot{u}_x = u_x^o * t_c$ where u_x^o is the final displacement and t_c is the total computation time. Since the computations were performed using an explicit solver, the displacement rates were chosen such that the kinetic energy was always much smaller than the total internal energy.

2.5.2 Constitutive laws

The effective area and stiffness of the rebar elements were selected to be consistent with the fiber volume fraction ($V_f = 0.83$) and the fiber Young's modulus ($E_f = 100$ GPa) of HB26 [31]. The elastic properties of the shell elements were taken to be the same as those of the effective medium in the analytical model ($E_{em} = 68$ MPa, $v = 0.4$). The plastic responses of the shell elements employed in the FE calculations are detailed in Table 2.1. They include cases of perfect plasticity as well as linear hardening. In one case, the linear-hardening law was augmented with a linear-softening portion, with softening modulus $\tilde{h}$, starting at an equivalent strain of 0.15 (coinciding approximately with the point at which dilatation was observed in the experiments). The latter scenario was intended to represent the effect of damage, as manifested in volumetric expansion (Figure 2.5).

Bonding between adjacent laminae was treated using the cohesive behavior within the contact algorithm available in Abaqus [32]. The behavior was modeled as a linear traction law with normal and shear tractions defined by:

$$\begin{bmatrix} t_x \\ t_y \\ t_z \end{bmatrix} = \begin{bmatrix} K_x & 0 & 0 \\ 0 & K_y & 0 \\ 0 & 0 & K_z \end{bmatrix} \cdot \begin{bmatrix} \delta_x \\ \delta_y \\ \delta_z \end{bmatrix} \tag{2.25}$$

where t_i are surface tractions in the global coordinate system, K_i are stiffness cooefficients and δ_i are the nodal separations. In this formulation, normal and shear components are decoupled; that is, normal separation does not give rise to shear tractions, and vice-versa. This description of normal tractions was only applied to tension; compressive forces between shell elements were treated with the general contact algorithm using "hard" contact.

Most of the FE calculations were performed using stiffness coefficients that reflect the response of the effective medium elements: notably, $K_x=K_y=G_{em}/H$ and $K_z=E_{em}/H$ where H is element thickness. In some cases, the stiffnesses were reduced by a factor of 10, in an effort to assess the sensitivity of the macroscopic response to these parameter values. In yet others, cohesion between the plies was removed, such that the 45° and -45° plies were uncoupled from one another. The latter represents the limiting case in which all plies have delaminated. The pertinent property values are summarized in Table 2.1.

2.5.3 FEA results

FEA results of the spatial variations in $\tilde{\varepsilon}_{yy}$ and $\tilde{\varepsilon}_{zz}$ for the cases denoted FEA-2 and FEA-3 (distinguished from one another by the cohesive stiffness values, Table 2.1) are plotted in Figure 9 and compared with the corresponding experimental measurements.

Evidently the mean values of the transverse strains are well captured by the FEA. The curves from FEA exhibit the "up-turns" near the specimen edges, similar to those seen experimentally. However, the magnitude of the up-turn is slightly underpredicted by the FEA. Furthermore, it increases as the stiffness of the interlaminar cohesive law is decreased. These comparisons suggest that edge effects associated with inelastic interlaminar shear are likely operative. No further efforts were made to capture such effects quantitatively.

The average values of $\tilde{\varepsilon}_{yy}$ and $\tilde{\varepsilon}_{zz}$ obtained for these two cases are plotted in Figure 2.5. The variations in $\tilde{\varepsilon}_{yy}$ with $\tilde{\varepsilon}_{xx}$ are virtually identical in the two cases (FEA-2 and FEA-3) and closely match those from the experiments and from the analytical model. The variations of $\tilde{\varepsilon}_{zz}$ with $\tilde{\varepsilon}_{xx}$ are also almost identical to one another but, as for the case of the analytical model, underpredict the measurements, especially at strains beyond 0.1. The results of FEA-1 (where the effective medium is perfectly plastic) are also shown. These agree exceedingly well with the corresponding analytical predictions for the same set of constituent properties. Yet another set of results, for FEA-4, where the plies are de-coupled from one another, exhibit a strong underprediction of the magnitudes of the strains. This result is qualitatively consistent with the relatively small amounts of interply delamination seen in the optical micrographs of the fractured test specimens, especially away from the fracture location (Figure 2.6).

The computed stress-strain curves are compared with the experimental measurements in Figure 2.10. For FEA-2 and FEA-3, the curves initially coincide with the measured ones (to a strain of about 0.15) but overestimate the strength at higher strains.

The slight difference between the two computed curves is a manifestation of the different cohesive stiffnesses (Table 2.1). In contrast, the response computed for the case in which the plies are uncoupled (FEA-4) lies well below the measurements. Here the fibers undergo minimal rotation and the hardening closely mimics that of the effective medium alone. The differences further illustrate the important effect of fiber rotations on the high apparent hardening rate of the composite.

The final set of computed results from both the analytical model and FE for the case in which the effective medium undergoes softening beyond a strain of 0.15 are plotted in Figure 2.11. For the selection $\tilde{h} = -3$ MPa, the analytical and FE results are in close agreement with one another and correlate extremely well with the measurements over the entire loading history. In addition to matching the plastic response, the predicted curve exhibits a load maximum at a strain of about 0.37: virtually identical to the measured failure strain. These correlations imply that microstructural damage does indeed play an important role in the plastic response of the composite at large strains. Despite this correlation, we acknowledge that the assumed softening response employed in this set of computations is *ad hoc* and lacks a sound mechanistic basis. Further study of the damage mechanisms at the microscopic level is clearly needed in order to fully capture the shear-dominated stress-strain response of Dyneema® composites at the highest plastic strains.

2.6 Discussion

In this chapter, an analytical constitutive model has been presented for the shear-dominated behavior of Dyneema® composites in 2D loading – as manifested in the in-plane tensile response of [±45°] cross-ply laminates – and compared with the predictions to both FE results and experimental measurements. In this regard, the binary representation of the constituent phases proves to be a useful basis for modeling the composite response. For all cases examined here, the analytical predictions are in excellent agreement with the FE results.

The results demonstrate that the rapid hardening in the stress-strain curve is attributable to fiber rotations and the associated changes in stress state. With realistic estimates of the pertinent constituent properties, the hardening rate is captured well by the analytical model up to moderate plastic strains. The model also yields a realistic bound on the limiting tensile failure strain. Although some edge effects are obtained in the strain distributions (likely caused by interlaminar shear), their spatial extent appears to be small in comparison to the specimen dimensions employed in the present tests. At larger plastic strains, corresponding to the onset of dilatation, the theoretical models over-predict the measured stresses. The discrepancies are likely due to microstructural damage. A phenomenological description of the softening caused by damage within the effective medium elements appears to capture the salient features of the stress-strain response and the strain at fracture, though additional work is needed to identify the

underlying mechanisms. The model also underestimates the out-of-plane strains associated with this damage. Further work in the cohesive zone representation of the inter-laminar behavior is necessary to capture these effects.

Having established the utility of a binary model representation of Dyneema® laminates, the FE model presented here is adapted to simulate the response of the laminates under more complex loadings, both quasi-static and dynamic. The details are presented in the following chapter.

Table 2.1: Constitutive laws employed in FEA

Designation	σ_o (MPa)	h (MPa)	$K_{x=}K_y$ (GN/m^3)	K_z (GN/m^3)	Comments
FEA-1	2	0	240	680	
FEA-2	2	20	240	680	
FEA-3	2	20	24	68	
FEA-4	2	20	0	0	
FEA-5	2	20	240	680	Softening after strain of 0.15

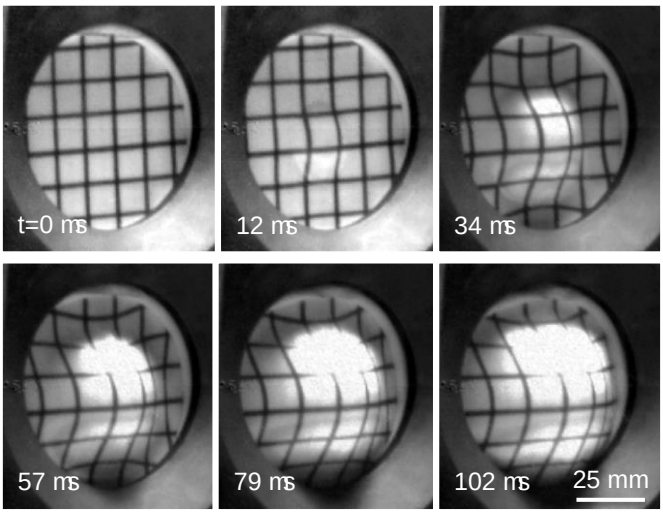

(a) During impact

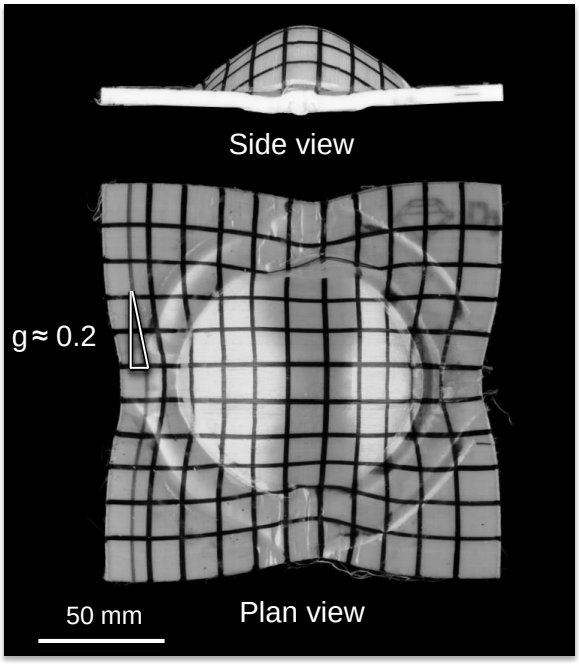

(b) After impact

Figure 2.1: Deformation of an HB26 plate situated behind a 6 mm-thick target plate upon impact with a 7.6 mm-diameter steel sphere at a velocity of 1195 m/s (E.A. Gamble, O. Nazarian, F.W. Zok, unpublished).

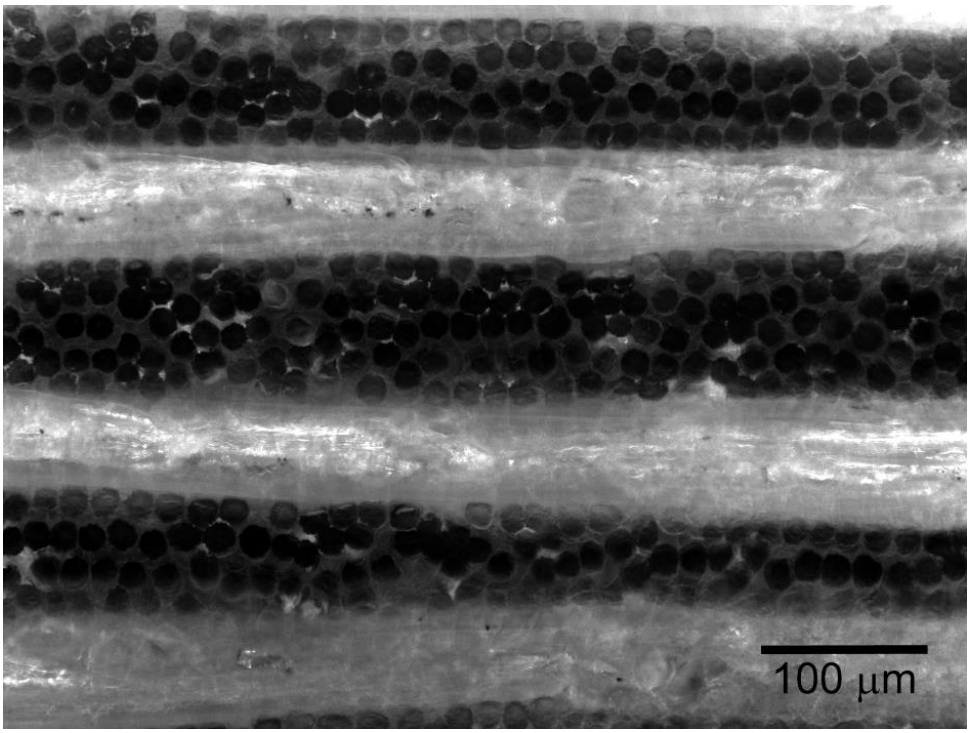

Figure 2.2: Dark-field optical micrograph showing the cross-ply architecture of HB26 laminate.

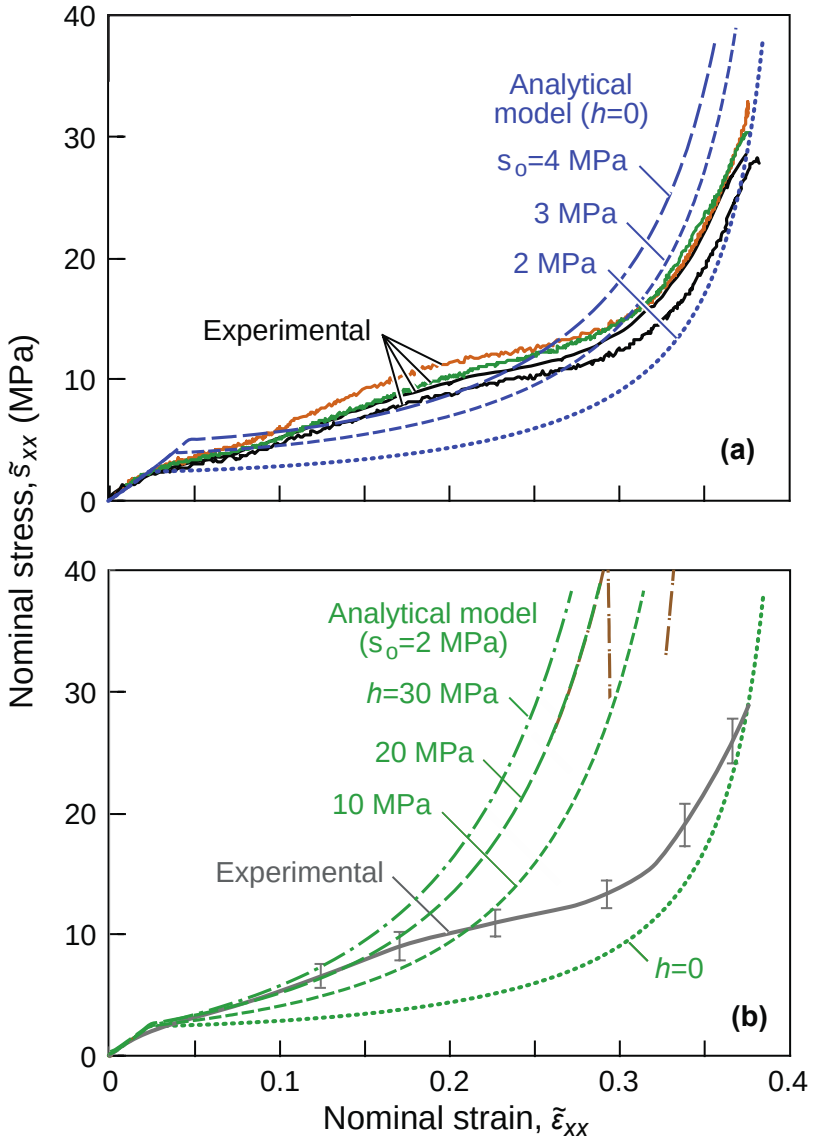

Figure 2.3: (a) Nominal tensile stress-strain response of HB26 laminate in the $[\pm 45°]$ orientation obtained from several tensile tests. Comparisons between experimental results and theory, showing effects of (a) the yield strength of the effective medium for an elastic-perfectly plastic material and (b) the effective medium tangent modulus in the post-yielding domain. The experimental curve in (b) represent average values; the error bars represent the full range from the measurements.

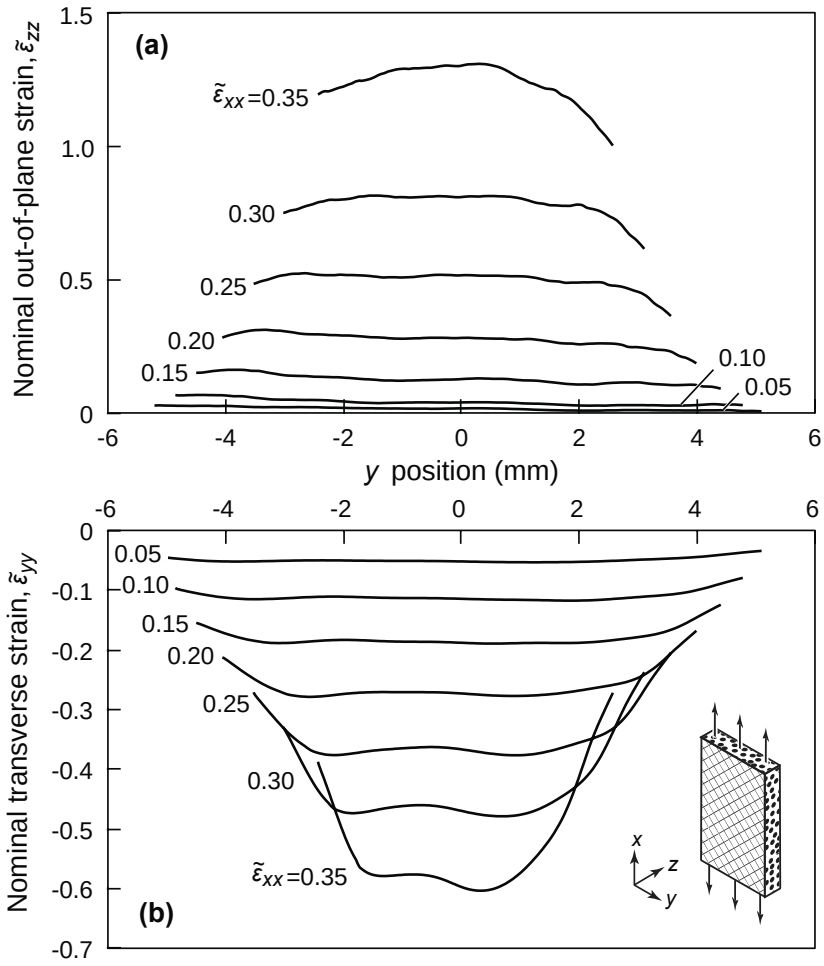

Figure 2.4: Transverse line scans of (a) out-of-plane and (b) in-plane transverse strains at various levels of applied axial strain.

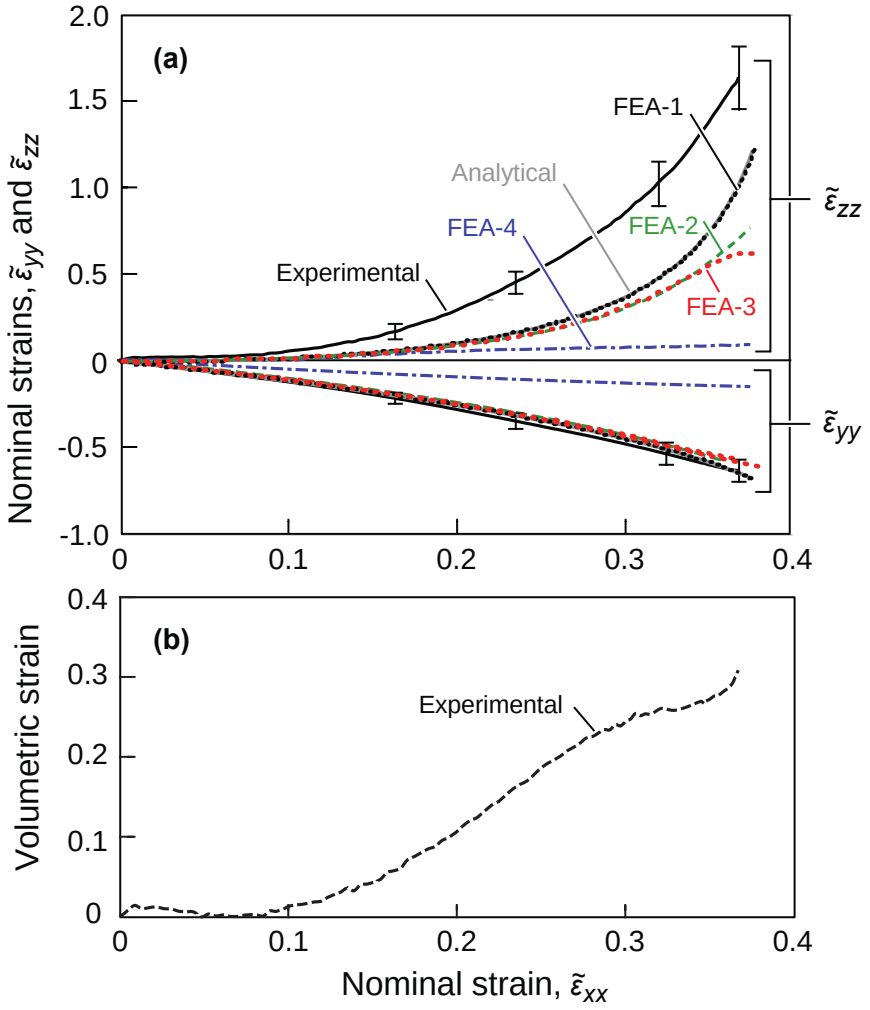

Figure 2.5: Evolution of (a) the two transverse strains and (b) the volumetric strain with nominal axial strain. The error bars in (a) represent the full range from the experimental measurements.

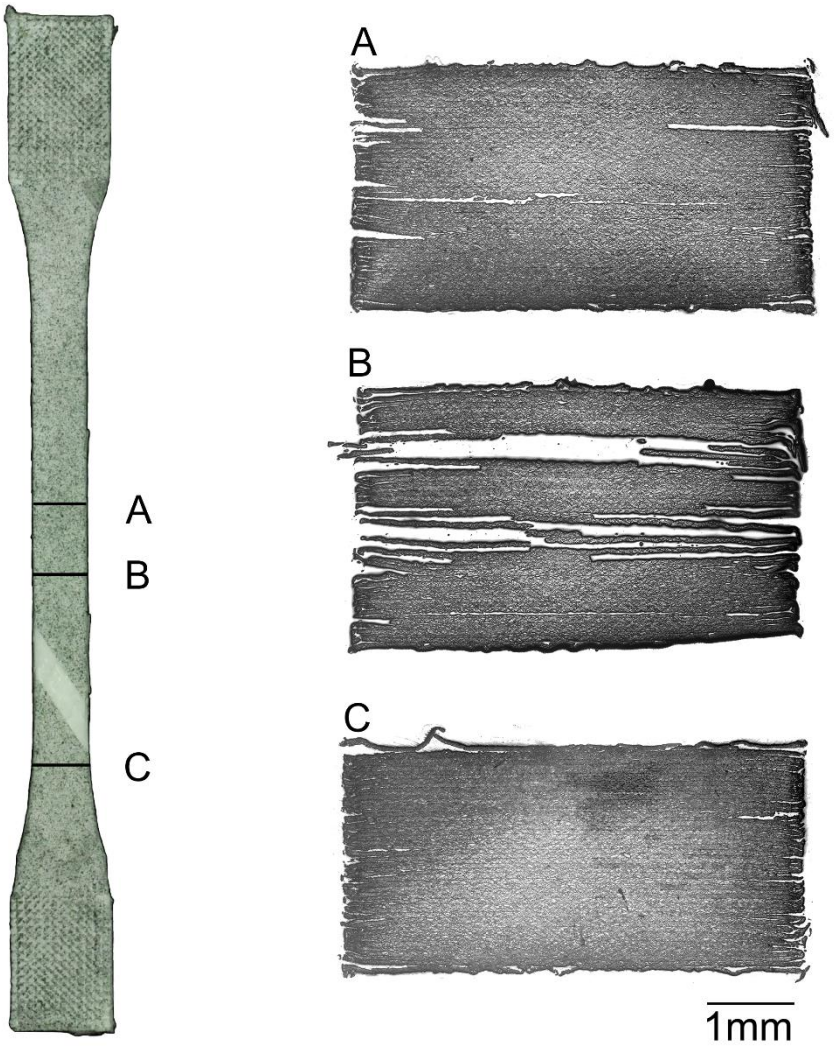

Figure 2.6: Photograph of fractured test coupon and optical images of transverse cross-sections at the indicated locations. Although not evident in the test coupon (on the left), the section at B is essentially *at* the fracture location.

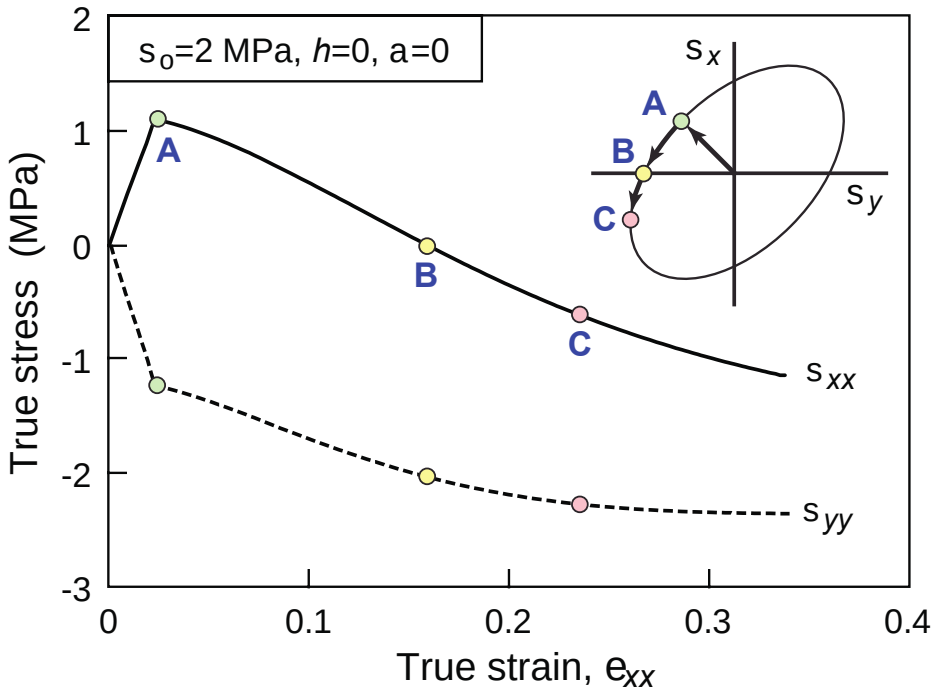

Figure 2.7: Evolution of effective medium in-plane stresses with axial strain for an elastic-perfectly plastic Mises-type material. Results are from analytical model. Inset shows the evolution of the stress path.

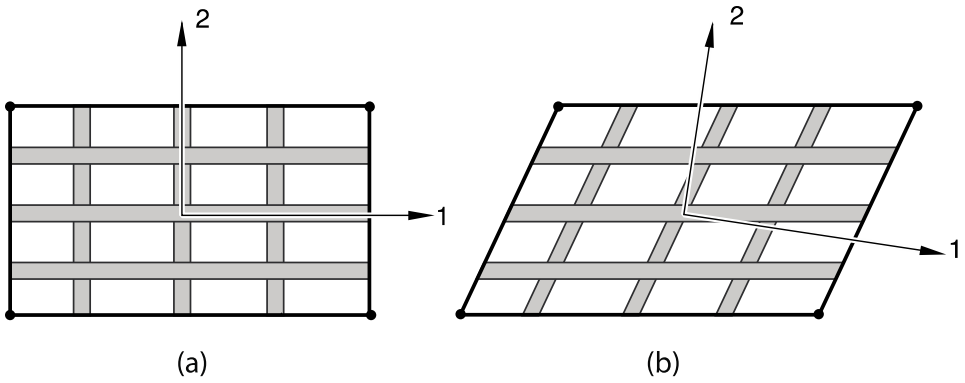

Figure 2.8: Schematics showing (a) rebar reinforcement in a first-order element, with the two sets of rebars initially aligned with the element isoparametric directions; and (b) the same element after large pure shear deformation. Here the rebars remain aligned with the element isoparametric directions. If the problem were modeled using an anisotropic yield condition, the principal material directions would rotate, as illustrated by the coordinate axes in (b). (Adapted from [32])

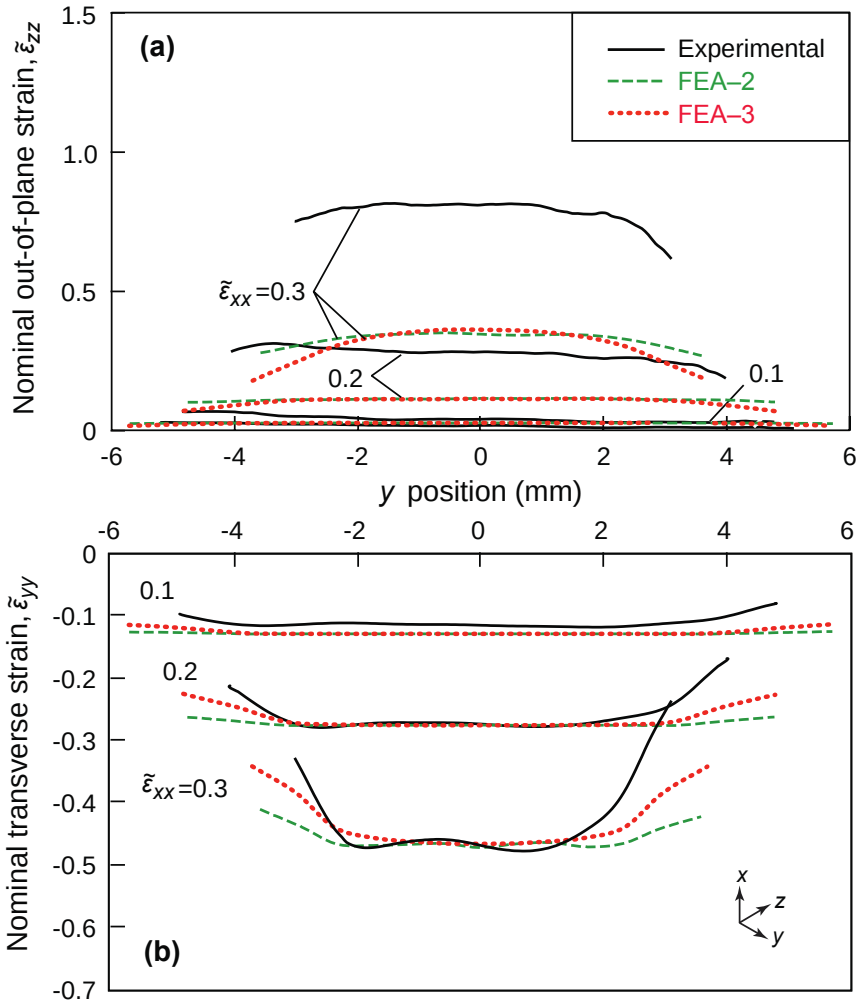

Figure 2.9: Spatial distributions of the two transverse strains from experimental measurements and finite element predictions as functions of axial strain.

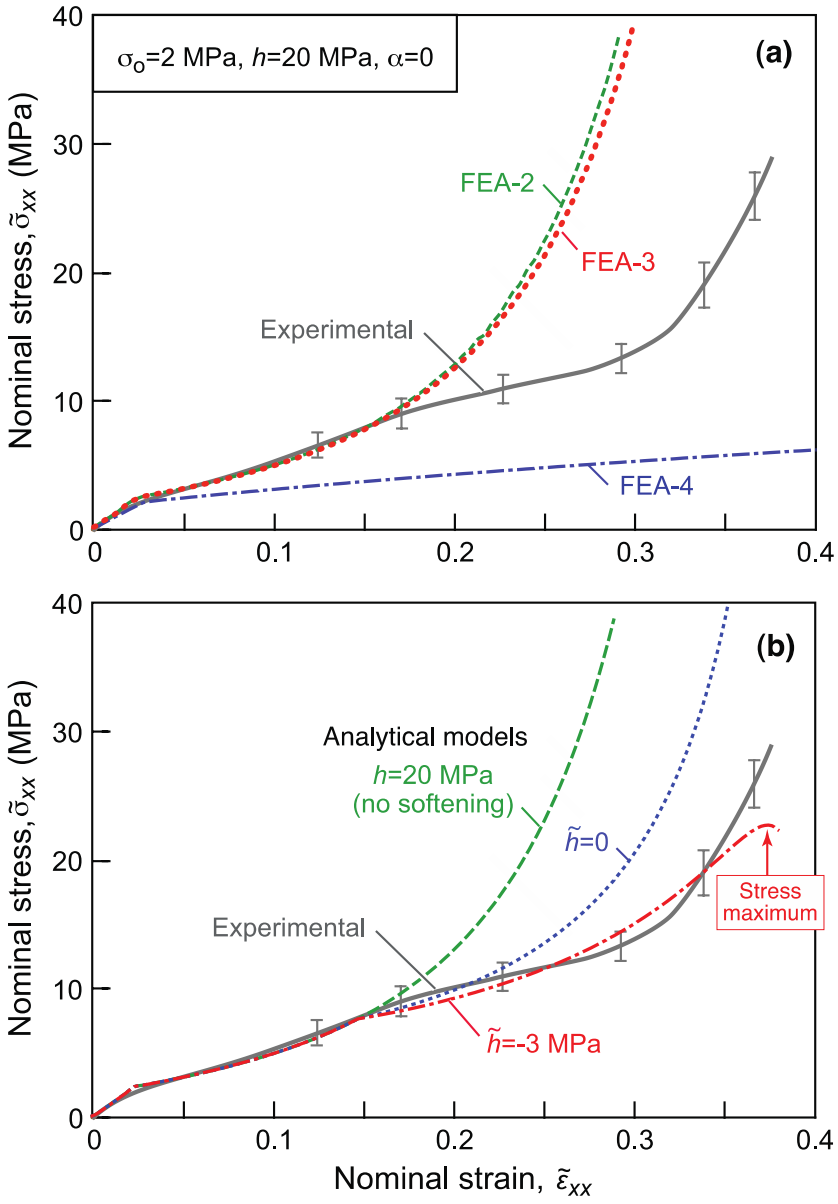

Figure 2.10: Comparisons of FEA and analytical model predictions with experimental measurements of tensile stress-strain response.

Chapter 3

Soft-impact response of Dyneema® composite plates

3.1 Introduction

In Chapter 3, a finite element model for predicting the behavior of Dyneema® composites in uniaxial tension was established. The pertinent FE material input parameters (i.e. E_{em}, v, σ_o and h) were calibrated from experimental tension tests with fibers oriented $\pm 45°$ to the loading axis [33]. The present chapter focuses on the dynamic response of Dyneema® plates in threat protection systems, where the stress state in the composite is multi-axial. In addition to this complexity, the yield strength and modulus of the composite have been shown to exhibit strain-rate sensitivity [25–27]. For these reasons, additional tests and modeling tools are necessary. The objective of this chapter is to extend the current form of the finite element (FE) model (as presented in Chapter 2) to incorporate the effects of dynamic loading, and to evaluate the efficacy of the model as a design tool for predicting the behavior of Dyneema® composites in armor systems.

The experimental portion of the chapter centers on the quasi-static and dynamic response of Dyneema® HB26 plates. Quasi-static punch tests are used to validate the choice of material parameters taken from a previous study [33]. The boundary condition in these tests are varied to study the role of the initial clamping pressure, P_o, on the load-displacement response. In parallel, dynamic experiments are performed by firing metal foam projectiles at plates of the composite material. These tests are designed to simulate the distributed pressure loads exerted on a catch-plate in armor systems. The impulse exerted on the samples is varied by changing the impact speed of the projectiles, and in-situ observations are made by utilizing high-speed video. The results of the experimental tests are presented in Section 3.2. Details of the finite element constitutive law is presented in Section 3.3. The rate sensitivity of the effective medium is studied by varying the elastic modulus, E_{em}, and the yield strength, σ_o, parametrically. The predictive capability of the model is assessed through comparisons with experimental observations. The key results are summarized in Section 3.4.

3.2 Experiments

3.2.1 Materials and test methods

All tests were performed on samples cut from $[0°/90°]_{48}$ cross-ply panels of Dyneema® HB26 (provided by DSM Dyneema, The Netherlands), identical to the material used in the study described in Chapter 2.

3.2.2 Quasi-static punch tests

The test configuration for the punch tests is illustrated in Figure 3.2(a). It was designed to simulate, in a highly idealized manner, the response of a spall shield located on the back face of a ballistic protection system containing a hard face material (e.g. ceramic) and secured in some fashion around its periphery. As demonstrated by the subsequent results, the test probes not only the effects of a distributed pressure but also the effects of boundary conditions as material is drawn in from the plate edges. The plate dimensions were $100\ mm\ x\ 100\ mm\ x\ 3.3\ mm$. The plates had been cut to size using a band saw with precautions taken to minimize fraying at the specimen edges. They were mounted between two precision-ground steel annular (washer-like) rings with $60\ mm$ inner diameter and $80\ mm$ outer diameter. The assembly (specimen and annular rings) was then placed in a mechanical test machine and loaded in compression to a specified pressure, P_o, between 1.3 and $12\ MPa$. Once the appropriate load had been attained, eight securing bolts passing through the annular rings were tightened uniformly until the machine force was reduced to zero. Subsequently, a torque wrench was used on each bolt to verify that the appropriate clamping pressure had been achieved. The samples were then loaded at the center-point of the front face using a $38\ mm$ diameter spherical punch at a rate of $1.2\ mm/min$. Most tests were performed until a load maximum had been reached and structural softening had commenced; this typically occurred at about $30 - 35\ mm$ of punch displacement. In one case, the sample was unloaded before the peak, for the purpose of comparing the surface appearances in the region of sliding between the samples and the clamping rings.

3.2.3 Dynamic loading

Impact tests were performed using the same specimen types in the same test fixture within a single-stage gas gun. The initial clamping pressure for these tests was $1\ MPa$. Tests were performed by firing cylindrical Al foam (Alporas®) projectiles at the center of the front face of the specimen. The projectiles had been prepared by electro-discharge machining (EDM). They had a diameter of 44 mm and a length of $53\ mm$. The foam density was approximately $\rho = 230\ kg/m^3$ and its relative density was 8.5%. Projectile velocities were measured using magnetic intervalometers (Physics Applications Inc.). Some tests were performed on the foam alone and high-speed photography was used to confirm the velocity measurements obtained from the intervalometers. The initial velocities ranged from 150 to $300\ m/s$. The reported velocities are estimated to have an error of no more than $\pm 5\%$. The dynamic displacement of the center point on the distal (back) face of the composite panel was monitored using a high-speed camera (Phantom v7, Vision Research Inc.). The surface was viewed at an angle of approximately $45°$. The precise orientation relationship between the two was obtained before each test from images taken of a scale that had been mounted normal to the specimen surface.

3.2.4 Experimental results

Representative load-displacement curves from the quasi-static punch tests are shown in Figure 3.3. Each curve is characterized by: (i) an initial nearly-linear rise, to

a displacement of about $10\ mm$, (ii) a secondary regime in which the load increases more rapidly, to a displacement of about $30\ mm$; and (iii) attainment of a load maximum followed by softening. The peak corresponds to the point at which the sample edges had been pulled through the annular rings and the total contact area between the rings and the sample had begun to decrease with increasing displacement. The loads increase only slightly with clamp pressure; over the range $Po = 1.3–12\ MPa$, the load at a specified deflection increases by about 15%.

Photographs of the tested samples at clamping pressures of 1.3, 4.0 and $12\ MPa$ are shown in Figure 3.4. To provide a frame of reference, the initial size of the plate is indicated by the dashed squares superimposed on the photographs. Also shown are the inner and outer diameters of the clamping ring: the area between the two indicating the region in which sliding had occurred between the sample and the rings. The samples exhibit significant pull-in from the distal regions of the plate, mainly along the two principal fiber directions (aligned with the sample edges). The pull-in is accommodated by shear deformation parallel to the fiber directions, as manifested in rotations of fiducial lines that were initially oriented parallel to the fiber directions. There is also some evidence of near-surface damage of the samples where they have slid past the clamping rings, especially at the highest clamping pressure. The damage involves delamination of thin layers of the composite. Based on numerical simulations presented in a subsequent section, this damage occurs when the interfacial stresses reach the interlaminar shear strength of the composite [26,27].

Figure 3.5 shows a sequence of images of the back face of a typical sample impacted by a foam projectile, at an impact velocity $v_o = 210\ m/s$. The displacement-time histories based on measurements from such images for this and other tests are plotted in Figure 3.6. Photographs of samples after testing at three different velocities are shown in Figure 3.7. The deformed shape is similar to that obtained in the quasi-static punch tests (Figure 3.4). Here, again, the bulging is accommodated by pull-in of material along the two fiber directions and the accompanying shear deformation. For impact velocities exceeding 300 m/s, the samples were pulled through the clamping rings on one half whereas the other half remained attached to the assembly.

3.3 Finite element model

3.3.1 Representation of Dyneema® HB26

For the purpose of the finite element calculations, the composite is represented by a binary model of the constituent phases, similar to the method described in Chapter 2. In the same fashion, the fibers are represented by an array of one-dimensional line-spring rebar elements. These elements are embedded within a three-dimensional continuum that represents an *effective medium*. However, several key modifications have been made in the current formulation. The details are described below.

The fiber architecture was modeled as a collection of 16 sheets of first-order surface elements with reduced integration. Each sheet contained unidirectionally-aligned rebar elements with a [0°/90°] layup. To reiterate from Chapter 2, this selection was based

on the understanding that, under large shear deformations, rebar elements are able to rotate and remain aligned with the element's isoparametric directions, as illustrated in Figure 3.8. Other approaches for modeling anisotropic materials, such as that based on the Hill yield condition, fail to properly capture such rotations and retain the correct orientation relationships. The properties of the rebar layer are smeared uniformly across an effective thickness. Operationally, this is done by assigning a rebar cross-sectional area, A_R, and a spacing, S_R, between rebar elements, with the effective thickness of a surface element then defined by $t_R = A_R/S_R$. The values were chosen to be representative of the fiber volume fraction V_f such that $t_R = V_f \cdot t_h$, where t_h is the thickness of the host element.

The effective medium was modeled with three-dimensional first-order continuum elements with reduced integration. A Mises-type constitutive law was employed. The material response was taken to be elastic-plastic with linear hardening after yield [33]. The surface elements were embedded into this effective medium and a kinematic constraint was used to enforce alignment of the element edges. This ensured that the in-plane deformations of both constituents was the same. The mass density of the composite was assigned entirely to the effective medium. In doing so, the embedded line elements only contribute additional stiffness to the host elements in the direction of the rebar. The modulus, E_{em}, yield strength, σ_o, post-yield hardening rate, h, and Poisson's ratio, v, of the effective medium were obtained by fitting tensile tests that had been performed in the $\pm 45°$ orientation (as described in Chapter 2 [33]). The curve fit is shown in Figure 9. The inferred property values are: $E_{em} = 80\ MPa$, $v = 0.4$, $\sigma_o =$

$2\ MPa$ and $h = 20\ MPa$. These properties are identical to the properties determined from the analytical analysis presented in Chapter 2. The finite element calculations in present study do not incorporate softening in the effective medium, ($\tilde{h} = h = 20\ MPa$), since the source of the softening in the tension tests remains uncertain.

For the impact calculations, the effect of strain rate $\dot{\varepsilon}$ on the yield stress $\sigma(\dot{\varepsilon})$ of the effective medium was modeled using a power-law of the form:

$$\frac{\sigma(\dot{\varepsilon})}{\sigma(\dot{\varepsilon}_o)} = \left(\frac{\dot{\varepsilon}}{\dot{\varepsilon_o}}\right)^k \tag{3.1}$$

where $\dot{\varepsilon_o}$ is a reference strain rate (chosen to be $10^{-3}\ s^{-1}$) and k is the power-law exponent. The limited available data on rate sensitivity, obtained from tension tests in the $\pm 45°$ orientation [25], indicate that $k \approx 0.08$. This value is used in the initial FE simulations; other values are also considered in order to assess the sensitivity of the results to this selection.

As demonstrated by the subsequent comparisons of the numerical and experimental results, the modulus of the effective medium also exhibits a rate sensitivity. Although this rate sensitivity is not explicitly modeled in the present study, a parametric study is performed to infer the modulus from comparisons to one impact test. Indeed, as expected, this modulus is considerably higher than the corresponding quasi-static value. Subsequently, this value is used to predict the behavior of the composite in the remaining experiments.

The in-plane element dimensions of the laminate were chosen following a mesh-sensitivity study. The study entailed varying the element width from $0.5\ mm$ to $2\ mm$

and the element thickness from $0.1\ mm$ to $0.8\ mm$. The computed stresses and strains for elements $1\ mm$ and $0.5\ mm$ wide were indistinguishable from one another and thus all subsequent calculations were performed using the higher value ($1\ mm$). In a similar fashion, the through-thickness dimension was chosen to be $0.2\ mm$.

3.3.2 Foam constitutive model

The projectile was modeled as a three-dimensional solid continuum using first-order elements with reduced integration and hourglass control. Each element had in-plane dimensions nominally $0.75\ mm$ x $0.75\ mm$ and a thickness of $0.2\ mm$. The choice of element thickness was selected to ensure that densification of the foam was accurately captured [34].

The material properties of the foam were characterized using the Deshpande-Fleck crushable foam model in ABAQUS. A non-associated flow potential was used, with parameters selected to be consistent with a plastic Poisson's ratio of 0. Consequently, the ratio of yield strengths in hydrostatic compression and uniaxial compression was taken to be $\sqrt{3}$. The uniaxial compressive response of the foam was represented by an analytical model developed by Gibson and Ashby [35]. The response has three domains: (i) elastic, characterized by a Young's modulus E_{fm} and a Poisson's ratio ν_{fm}; (ii) perfectly-plastic crushing at a plateau stress, σ_{pl}, and with a plastic Poisson's ratio of zero; and (iii) a hardening domain at strains beyond a critical value, given by $\varepsilon_D(1 - 1/D)$ where ε_D is the densification strain and D is a fitting parameter (selected

to be 2.5). The plastic response in the latter (hardening) domain is described by:

$$\frac{\sigma_{fm}}{\sigma_{fm}^{pl}} = \frac{1}{D}\left(\frac{\varepsilon_D}{\varepsilon_D - \varepsilon_{fm}}\right)^m \tag{3.2}$$

where σ_{fm} and ε_{fm} are the axial stress and strain, respectively, and m is a fitting parameter (taken to be 1). Based on previous measurements of the mechanical properties, the elastic modulus and plateau stress of the foam were taken to be $\sigma_{fm}^{pl} = 1.35\ MPa$ and $E_{fm} = 1.1\ GPa$, respectively. The density of the foam was chosen to match the weight of the projectile in each experiment, approximately $\rho_{fm} = 235 \pm 10\ kg/m^3$.

The strain rate sensitivity of the composite response in the dynamic domain was prescribed by a power-law of the form:

$$\dot{\varepsilon} = D\ (R-1)^n \tag{3.3}$$

$$R = \frac{\sigma_{fm}^{pl}(\dot{\varepsilon})}{\sigma_{fm}^{pl}(\dot{\varepsilon}_o)} \tag{3.4}$$

Here $\dot{\varepsilon}$ is the strain rate, $\dot{\varepsilon}_o$ is a reference strain rate ($10^{-3}\ s^{-1}$), and R is the strength ratio at the two strain rates, $\dot{\varepsilon}$ and $\dot{\varepsilon}_o$. The coefficient D and exponent n are determined by the initial projectile velocity and the material properties of the foam. The foam is assumed to be linear-viscous with viscosity, μ, defined by [34]:

$$\mu = \left(\rho_{fm} \cdot c \cdot l\right) \tag{3.5}$$

where c is the shock propagation speed in the foam and l is the width of the shock front. Since the material is assumed to be essentially rigid beyond the densification strain, the

shock speed can be expressed as $c = v_o/\varepsilon_D$, where v_o is the initial velocity of the projectile and is taken to be equivalent to the change in velocity across the shock front. Since momentum is conserved across the shock, the difference in the yield stress on either side of the shock front is:

$$\sigma_{fm}^{pl}(\dot{\varepsilon}) - \sigma_{fm}^{pl}(\dot{\varepsilon}_o) = \rho_{fm}\, c\, v_o = \frac{\rho_{fm}\, v_o^2}{\varepsilon_D} \tag{3.6}$$

This can be rewritten in terms of R and l, yielding:

$$R - 1 = \frac{\mu\ v_o}{\sigma_{fm}^{pl}(\dot{\varepsilon}_o)\, l} \tag{3.7}$$

Since we are interested in the elevation in stress due to viscous effects, the relevant strain rate is simply the one at the shock front, and is given by:

$$\dot{\varepsilon} = v_o/l = \frac{\sigma_{fm}^{pl}(\dot{\varepsilon}_o)}{\mu} \cdot (R - 1) \tag{3.8}$$

Upon comparison with Eqn. (3.3), the coefficient $D = \sigma_{fm}^{pl}(\dot{\varepsilon}_o)/\mu$ and $n = 1$.

3.3.3 Model definition

For computational efficiency, only one-quarter of the assembly was modeled (Figure 3.2(b)). Appropriate displacement and rotational boundary conditions were prescribed on the axes of symmetry. The bolts and outer assembly were not explicitly modeled. Instead, the contact pressure at the interface between the sample and the annular rings was achieved by implementing a displacement boundary condition between the sample and the two ring surfaces. In the initial step of the calculation, the two rings

were brought into contact with the composite panel to achieve the desired clamping pressure. Thereafter, the positions of the rings were held fixed.

For simulations of the quasi-static punch tests, the spherical punch was modeled with elastic, first-order continuum elements with an average element length of $0.5\ mm$. The elements within the punch were assigned a constant displacement rate, in accord with that used in the experiments. In the dynamic calculations, an initial velocity was assigned to all material points in the projectile.

All contact surfaces were modeled using the "surface-to-surface" contact algorithm in Abaqus [32]. Contact normal to element surfaces was treated as being "hard" and the tangential response was modeled using a penalty formulation. A friction coefficient μ_o was assigned to adjust the penalty. The friction coefficient between the annular rings and the composite was determined experimentally. This was accomplished by placing one of the annular rings on a sheet of the composite, applying a dead-load on top of the ring, and then measuring the force required to move the ring across the laminate at a constant rate. The tests were performed with several different weights. In all cases, the friction coefficient was $\mu_o = 0.1 \pm 02$.

3.4 Results of finite element simulations

3.4.1 Quasi-static punch tests

FEA results of the load-displacement curves for the quasi-static punch tests are compared with the corresponding experimental measurements in Figure 3.3. Each pair

of curves represents the results for a different value of the initial clamping pressure, P_o. The mechanical response of the samples tested at the two lower values of P_o is captured well by the simulations over most of the loading history. The results begin to diverge only at high displacements ($\delta \geq 25\ mm$). Thereafter, the measured response exhibits larger displacements and lower peak load than that emerging from the simulations. At higher clamp pressures ($P_o = 12\ MPa$), the simulated results deviate from the experimental ones earlier, at a penetration depth of about $10\ mm$.

To gain some further insights into limitations of the numerical model and the underlying assumptions, the average contact shear stress τ_μ due to friction beneath the annular rings was also calculated. The variation in this stress with penetration depth is plotted in Figure 3.9(b). Each curve starts at a value of $\mu_o P_o$ but then rises when the displacement exceeds $10-15\ mm$. Also indicated on these curves are the points at which the finite element predictions deviate from the experimental measurements by more than 10%. In each case, the deviation initiates at a shear stress $\tau_\mu \approx 1.5\ MPa$. This value coincides closely with the interlaminar shear strength ($\approx 1.7\ MPa$) measured by Karthikeyan et al. on essentially the same composite material [26,27]. Furthermore, the relatively small damage amount of surface damage on the specimen clamped with a pressure of $1.3\ MPa$ and unloaded before the peak load (at a displacement of $24\ mm$) can be attributed to the fact that the interfacial shear stress ($1.0\ MPa$) had not achieved a sufficiently high value to initiate delamination. The conclusion is that the model in its current form (based on the assumption of frictional sliding at the sam-

ple/ring interface) begins to break down once the interfacial stresses exceed the inter-laminar shear strength. The critical point at which this occurs depends on both the clamping pressure and the amount of displacement.

3.4.2 Foam impact tests

Comparisons of the computed and measured back-face deflection histories of samples impacted by foam projectiles are presented in Figure 3.6. Here all parameter values were the same as those in the quasi-static punch tests. However, the strain rate sensitivity of the effective medium modulus and yield strength have been incorporated into the model. To achieve good agreement between the predictions and the measurements, this modulus was calibrated to one impact test ($v_o = 210\ m/s$), and was determined to be $260\ MPa$ (higher than the quasi-static value of $80\ MPa$). The power law exponent was determined from experiments in the literature, and taken to be $k = 0.08$. With this fixed set of material properties, the measured curves across all of the experiments are well-matched by the simulated results. The only exception is for the test conducted at the highest impact velocity (305 m/s) wherein the sample is penetrated by the foam projectile.

Additional simulations showing the effects of the modulus on the predictions for one particular case (v_o=210 m/s) are shown in Figure 3.11(a). (Here all other material properties were unchanged.)). Reductions or elevations in E_{em} by 50% (relative to the baseline case $E_{em} = 260\ MPa$) yield a $9.25 \pm 3.5\%$ change in the plateau displacement.

In light of the fact that only a small amount of data on the strain rate sensitivity of the effective medium is available [25], additional parametric studies were performed to assess the effects of k. The results are shown in Figure 3.11(b). In this case, reductions or elevations in k by 50% (relative to the baseline case $k = 0.08$) yield only about a $15 \pm 3.5\%$ change in the plateau displacement. Additionally, changes in E_{em} and k have no effect on the intial (rising portion) of the deflection-time curve.

3.5 Discussion

A finite element model for the shear-dominated behavior of Dyneema® composites based on a binary representation of the composite constituents has been developed. The pertinent quasi-static material properties in the model (notably E_{em}, v, σ_o and h) have been calibrated from results of ±45° uniaxial tension tests [33]. Using the the quasi-static material properties coupled with an independent measurement of μ_o , the resulting predictions of the punch response agree very well with the measurements, with the exception of that near the load maximum. In the latter regime, the simulations yield over-estimates of the loads: a discrepancy attributable to the damage done during pull-in of the specimens past the ring clamps and the resulting reduction in the frictional sliding resistance. Observations of tested samples and FE simulations suggest that the damage initiates at a critical value of interfacial shear stresses, given approximately by the interlaminar shear strength of the composite. Finally, using the quasi-static material properties coupled with a value of k from other studies [25] and parameteric numerical

studies in E_{em}, the dynamic response of clamped samples during impact by foam projectiles was shown to be predicted equally well. In order to advance the model from its current form, a critical assessment of the strain rate dependent behavior is necessary.

Chapters 2 and 3 have discussed the utility of fiber composites in threat-protection systems, and have outlined modeling techniques for predicting their behavior in a regime characterized by very high deformation rates ($\dot{\varepsilon}\sim 1000\ s^{-1}$). The following two chapters present an analysis of material systems designed for protection in the low-velocity impact of a human head with the interior walls of a vehicle.

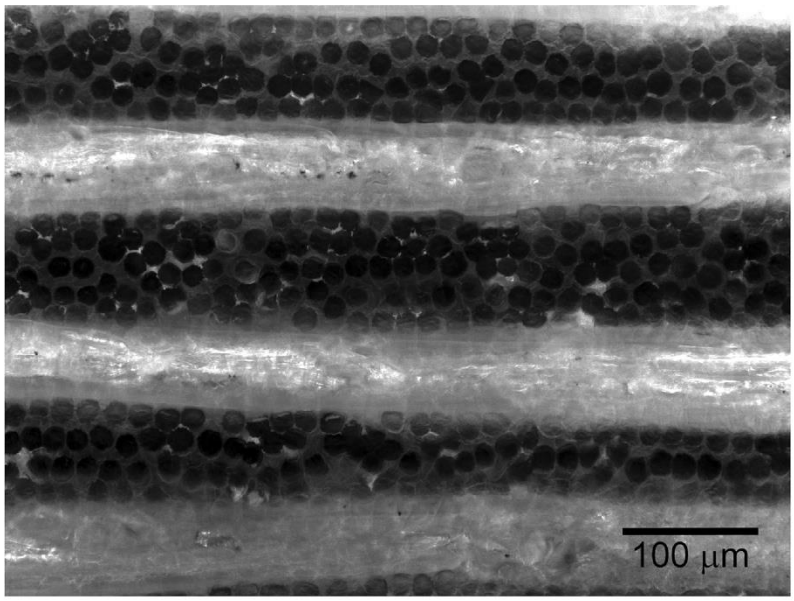

Figure 3.1: Dark-field optical micrograph showing the fiber architecture of Dyneema® HB26.

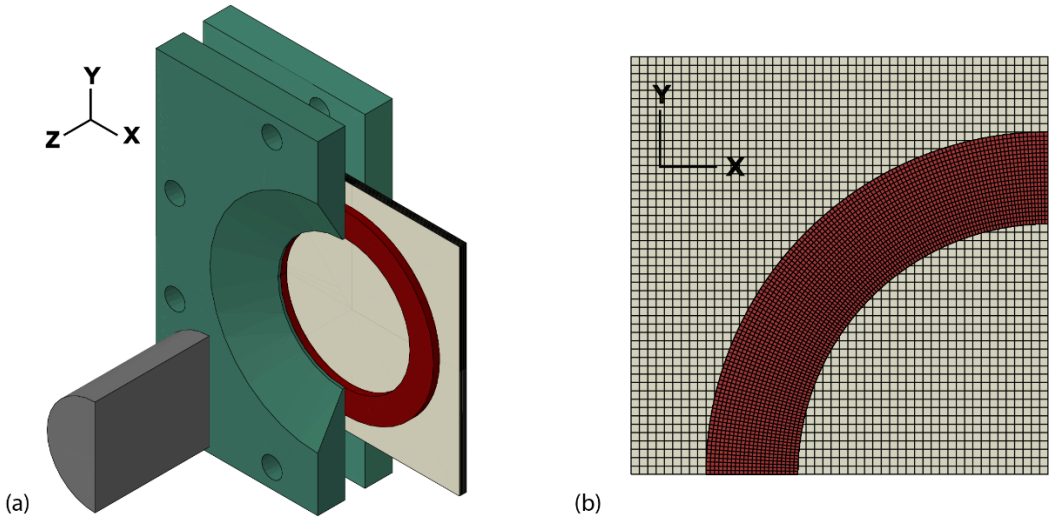

Figure 3.2: (a) Schematic of one half of the assembly used for foam impact tests. (b) The finite element geometry and mesh of the sample in plan-view.

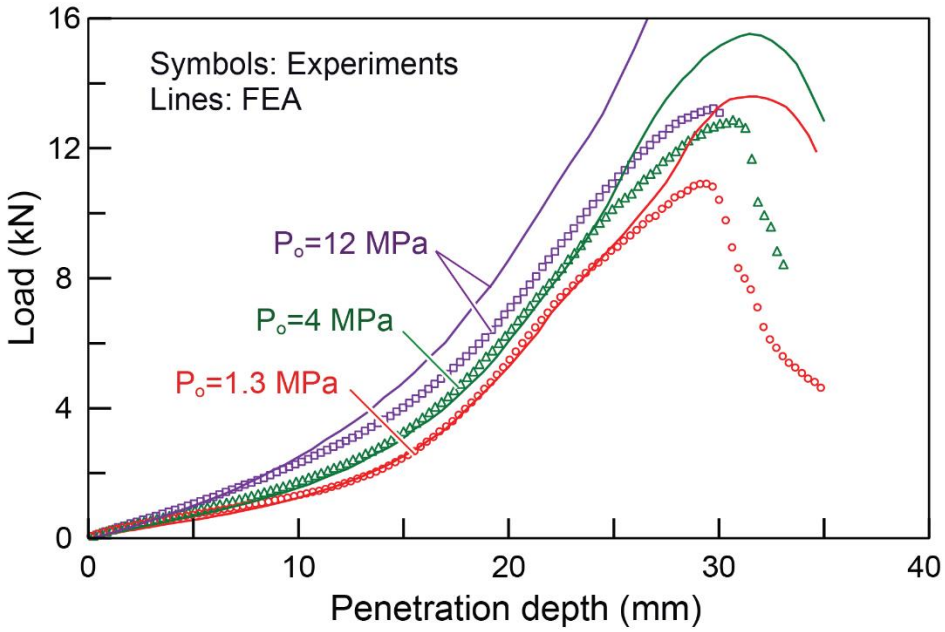

Figure 3.3: Experimental measurements and finite element predictions of the quasi-static punch tests.

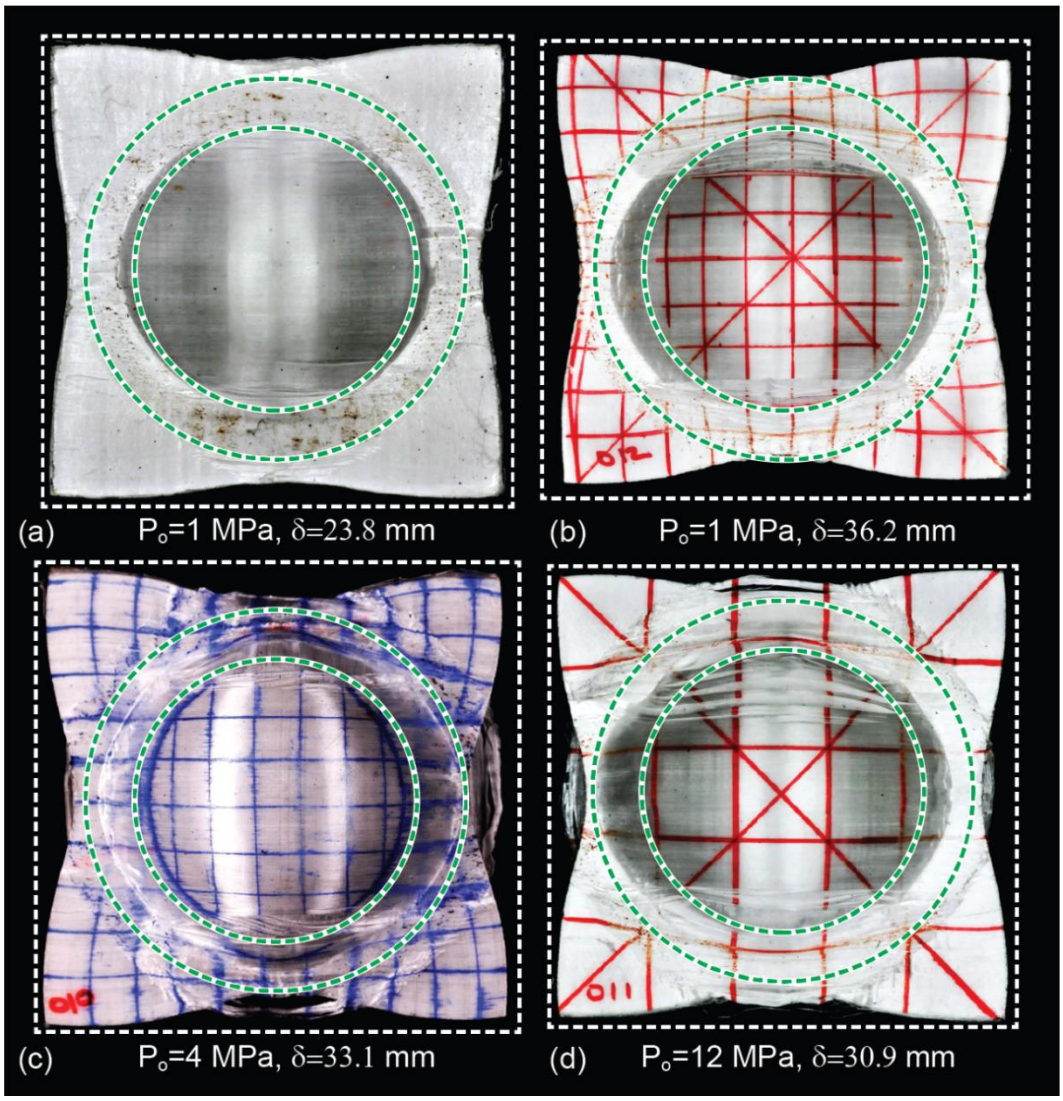

Figure 3.4: Photographs of test samples after punch tests, showing (a,b) effects of peak displacement on the surface appearance of samples tested with a clamping pressure of 1.3 MPa, and (c,d) effects of clamping pressure (indicated on the images).

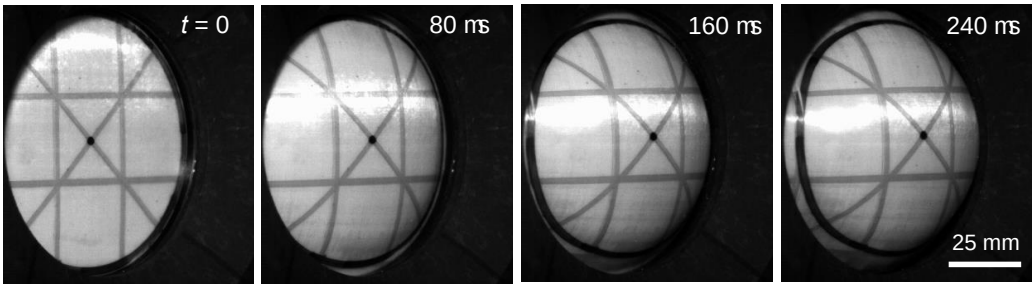

Figure 3.5: Sequence of images showing the back-face response of a sample upon impact with a foam projectile at 210 m/s.

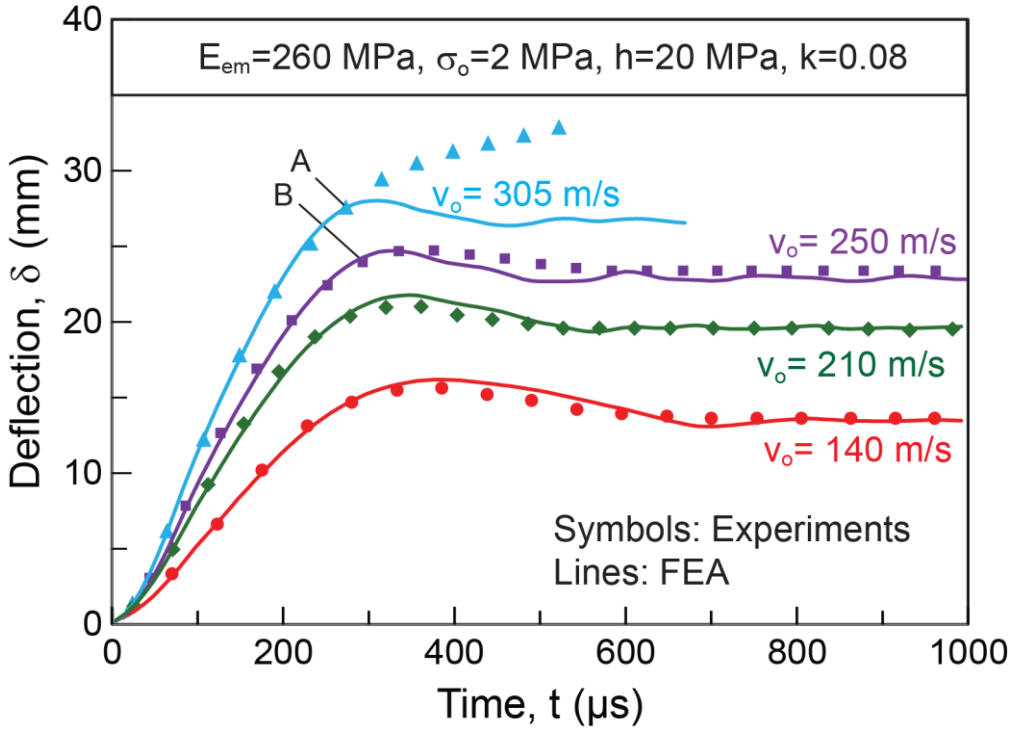

Figure 3.6: Experimental measurements and finite element predictions of the temporal evolution of the center-point back-face deflection.

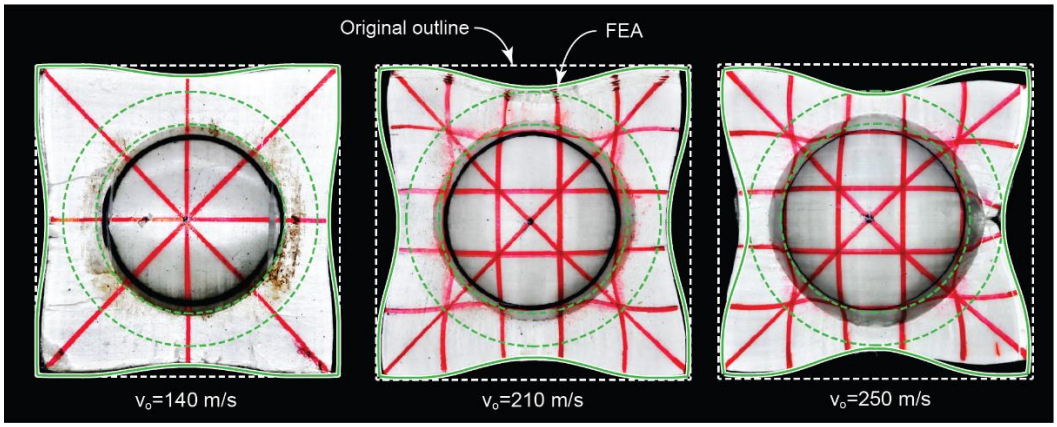

Figure 3.7: Photographs of test specimens after foam impact tests at three different velocities.

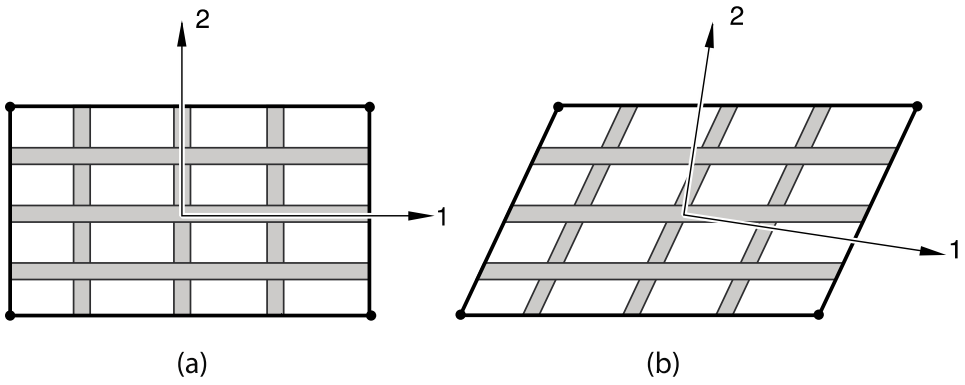

Figure 3.8: Schematics showing (a) rebar reinforcement in a first-order element, with the two sets of rebars initially aligned with the element isoparametric directions; and (b) the same element after large pure shear deformation. Here the rebars remain aligned with the element isoparametric directions. If the problem were modeled using an anisotropic yield condition, the principal material directions would rotate, as illustrated by the coordinate axes in (b). (Adapted from ABAQUS FEA Manual [32])

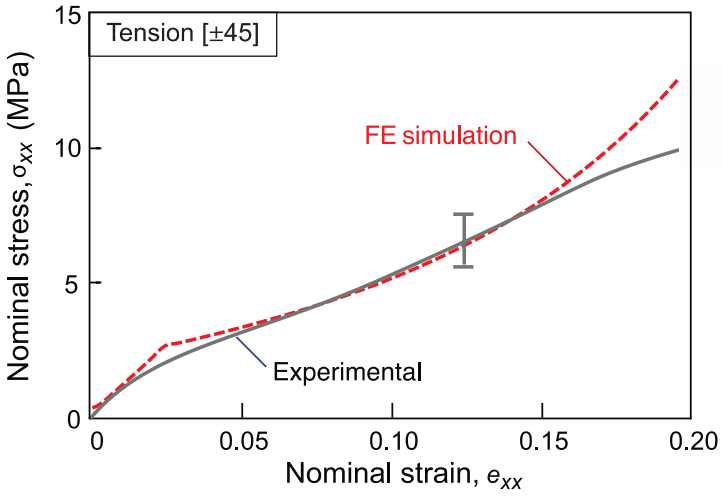

Figure 3.9: Quasi-static tensile response of the composite in the ±45° orientation and the FE simulations used to infer the pertinent elastic constants of the effective medium elements.

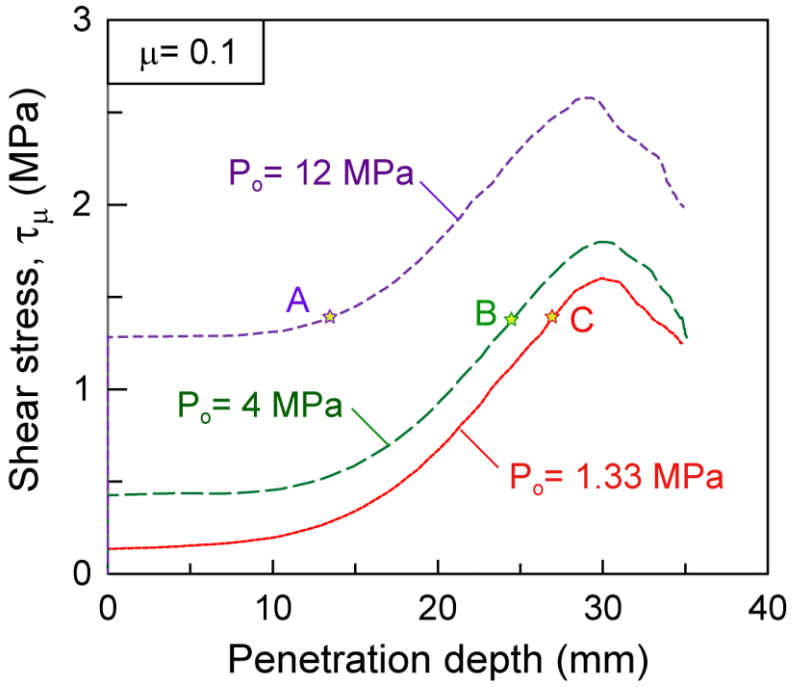

Figure 3.10: Computed variation in the average shear stress at the sample/ring interface during quasi-static punch tests with varying clamping pressures. Points A, B, and C correspond to the displacements at which the finite element predictions (on Figure 3.3) deviate from experimental measurements by more than 10%.

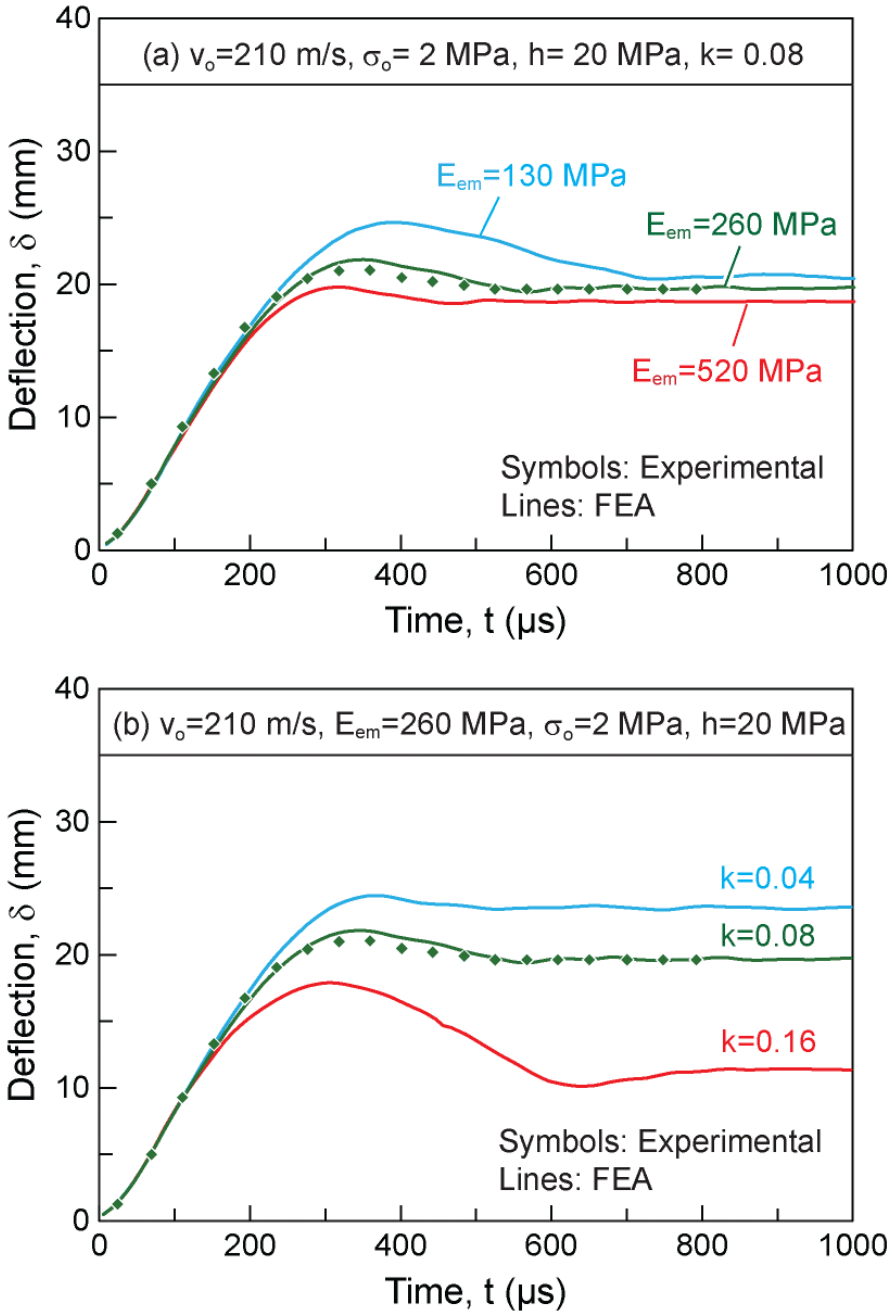

Figure 3.11: Effects of (a) effective medium modulus and (b) strain rate sensitivity parameter k on the evolution of back-face deflection for impact at 210 m/s. Also shown for comparison are the corresponding experimental measurements.

Chapter 4

Analysis of protective materials for mitigating head injury

4.1 Introduction

The prior two chapters have focused on the intrinsic properties of Dyneema® laminates and the development of a framework for modeling the behavior of these composites in threat protection systems. This chapter concentrates on an analysis of materials that are used to mitigate the secondary effects of a blast event, wherein occupants of a vehicle are susceptible to head injuries resulting from collisions with the cabin interior. As discussed in Chapter 1, the physiological mechanisms of head injury remain to be fully elucidated. However, there have been countless studies conducted on this topic [10,12,14,19,36–38]. The culmination of this research has led to the Head Injury Criterion (HIC), an empirical parameter that correlates the accelerations imparted to the human head during impact to the severity of injury. To reiterate from Chapter 1, the HIC is defined by [13]:

$$HIC = \max_{t_1,t_2}\left\{\left[\frac{\int_{t_1}^{t_2} a(t)dt}{t_2-t_1}\right]^{5/2}(t_2-t_1)\right\} \tag{4.1}$$

where $a(t)$ is the acceleration imparted to the head, and the quantity $(t_2 - t_1)$ defines an interval that maximizes the HIC. It should be noted that the predictive capability of the HIC parameter is limited to severe head injuries, where the criterion is skull fracture. Therefore, the term "head injury" in this study refers to damage in the form of skull fracture, rather than brain injury.

The principal objective of this chapter is to present an analytical framework for selecting protective materials that minimize the HIC subject to constraints on allowable thickness. The scope is restricted to impacts with initial velocities in the range of about $1-10\ m/s$ and duration times in the range of $1-30\ ms$. These encompass the majority of events associated with the secondary impact of a vehicle occupant with the interior structure in blast impact scenarios. It is also relevant to impacts commonly encountered in sporting events and typical automobile accidents [4,5,7,9,18,20,22,36,39]. In this velocity–time domain, impact is essentially quasi-static in the sense that there is ample time for stress waves to travel over distances comparable to the dimensions of the human skull and thus a quasi-equilibrium state is attained[2].

[2] The elastic wave speed in the human skull is in the range 2500–2900 m/s. Thus the time required for stress waves to travel a characteristic distance of 0.2 m (roughly the diameter of the human head) is about 70 μs. This time scale is about two orders of magnitude smaller than the impact duration times of present interest. Thus, for the purpose on analyzing head motion, details of stress wave propagation can be neglected.

The framework presented here is based on an idealization of the form and the properties of the constituents. Specifically, the head is represented by a rigid spherical mass and the target is a flat foam plate supported on a rigid foundation. The foam is treated as a rate-independent, rigid-perfectly plastic material. The analytical results are presented in Section 4.2. A critical assessment of the predictive capability of the model is made through comparisons with a series of experimental measurements from impacts of an instrumented headform with three different commercial foams. The experimental results are presented in Section 4.3. Additional comparisons are made with the results of finite element simulations that take into account the elasticity of the foam as well as its hardening during densification (also in Section 4.3). Despite its seeming simplicity, the analytical model is found to predict the acceleration-time histories and the HIC values to within $5-10\%$ of the values measured experimentally or obtained from finite element simulations.

4.2 Analytical model of impact

As a model problem, consider the impact of a spherical body of radius R, mass m and initial velocity v_o with a flat crushable foam pad, thickness H_o, mounted on a rigid foundation (Figure 4.3(a)). The foam is assumed to be rigid/perfectly-plastic with a crushing stress σ_o up to the densification strain ε_D. Thereafter, at higher strains, the foam behaves as a rigid solid. The foam pad is further assumed to be sufficiently thick (defined below) so that full densification does not occur before the mass arrests. (The

pad thickness inherently acts as a constraint, since thicker pads of softer materials will always lower the HIC value but introduce impractical solutions.) Additionally, the penetration depth of the spherical body into the foam pad is assumed to be small compared to R. A derivation of the equations of motion of the spherical body during the impact event follows.

For small displacements ($x << R$), the contact area A is given by $A \approx 2\pi Rx$ and thus the contact force is $F = 2\pi R\sigma_o x$. Here the foam acts effectively as a linear *inelastic* spring with stiffness $k \equiv 2\pi R\sigma_o$. The equation of motion of the sphere is thus given by:

$$m\ddot{x} + kx = 0 \tag{4.2}$$

Provided arrest precedes densification, the full solution to Eqn. (4.2) is:

$$x(t) = v_o\sqrt{\frac{m}{k}}\,\sin\sqrt{\frac{k}{m}}\,t \tag{4.3}$$

$$v(t) = v_o\,\cos\sqrt{\frac{k}{m}}\,t \tag{4.4}$$

$$a(t) = \frac{-\ddot{x}}{g} = \frac{v_o}{g}\sqrt{\frac{k}{m}}\,\sin\sqrt{\frac{k}{m}}\,t \tag{4.5}$$

over the time domain

$$0 \le t \le t_o = \frac{\pi}{2}\sqrt{\frac{m}{k}} = \frac{1}{2}\sqrt{\frac{\pi m}{2R\sigma_o}} \tag{4.6}$$

Thereafter, for $t \ge t_o$, $x(t) = v_o\sqrt{m/k}$, $v(t) = 0$ and $a(t) = 0$ (Figure 4.3(b)). Thus, the peak acceleration and peak displacement, obtained at $t = t_o$, are

$$a_{max} = \frac{v_o}{g}\sqrt{\frac{k}{m}} = \frac{v_o}{g}\sqrt{\frac{2\pi R\sigma_o}{m}} \tag{4.7}$$

and

$$x_{max} = v_o\sqrt{\frac{m}{k}} = v_o\sqrt{\frac{m}{2\pi R\sigma_o}} \tag{4.8}$$

In order for arrest to precede densification, the foam thickness must exceed a critical value, given by

$$H_o = \frac{x_{max}}{\varepsilon_D} = \frac{v_o}{\varepsilon_D}\sqrt{\frac{m}{k}} \tag{4.9}$$

The HIC value is evaluated using Eqn. (4.1). Here $t_2 = t_o$ and t_1 is obtained by maximizing the quantity within $\{...\}$ in Eqn. (4.1). It has the solution

$$t_1 = 0.518\sqrt{\frac{m}{k}} \tag{4.10}$$

The corresponding time interval over which the integration is performed is

$$t_2 - t_1 = 1.05\sqrt{\frac{m}{k}} \tag{4.11}$$

Combining Eqns. (4.1), (4.5), (4.6) and (4.10) yields

$$HIC = 0.651\left(\frac{k}{m}\right)^{3/4}\left(\frac{v_o}{g}\right)^{5/2} \tag{4.12}$$

Imposing the time restriction $t_2 - t_1 \leq t_c$ we find that the solution in (4.12) is valid for:

$$HIC \geq 0.651\left(\frac{1}{t_c}\right)^{3/2}\left(\frac{v_o}{g}\right)^{5/2} \tag{4.13}$$

The minimum value of the *HIC* is obtained when the foam thickness is equal to its minimum critical value. From Eqns. (4.9) and (4.12), the minimum HIC is:

$$HIC_{min} = \frac{1.84\, v_o^4}{(2H_o\varepsilon_D)^{3/2} g^{5/2}} \tag{4.14}$$

It is attained when the foam strength is:

$$\sigma_o^{opt} = \frac{m\, v_o^2}{2\pi R\, (H_o\varepsilon_D)^2} \tag{4.15}$$

The results in Eqns. (4.14) and (4.15) have been used to construct a "design map", shown in Figure 4.4. The axes are HIC_{min} and σ_o^{opt}. Contours are plotted for constant values of two parameters: (i) the impact velocity v_o and (ii) the maximum allowable penetration depth, given by the product of the foam thickness and the densification strain, $H_o\varepsilon_D$. (The latter product constitutes a minimum effective foam thickness). The other parameter values are $R = 0.1\ m$ and $m = 4.5\ kg$ (representative approximately of the human head). Its use is demonstrated by way of the following examples.

Consider first a scenario in which the maximum allowable head motion following impact is $15\ mm$ and the anticipated maximum impact velocity is $6\ m/s$ (point **A** in Figure 4.4). Under these conditions the best-case scenario would lead to a HIC value of 1520; it would require use of a foam with a strength of $1.14\ MPa$. Use of a harder foam would lead to a reduced amount of head travel with higher accelerations imparted to the head and hence an increase in HIC. Use of a softer foam would potentially be much worse. It would lead to full densification of the foam and a rapid rise in acceleration in the final stages of impact. If, on the other hand, the constraint on allowable

head motion were increased to $20\,mm$, the lowest HIC value at the same impact velocity would be reduced to 990 (point **B)**. This would require use of a different foam – one with a strength of $0.64\,MPa$. A further increase in allowable head travel to $25\,mm$ would reduce the HIC further, to 720, for a foam with strength of $0.41\,MPa$ (point **C**).

An alternative scenario would be one in which the allowable travel is rigidly set at a prescribed value, say $15\,mm$, and a maximum allowable HIC value, say 700, is prescribed to prevent a specified level of head injury. In this case, the requisite protection would be achieved only up to velocities of $5\,m/s$, using a foam with strength of $0.8\,MPa$ (point **D**). Using either harder or softer foams would lead to an increase in HIC.

Also shown on Figure 4.4 is the domain in which the computed HIC violates the time restriction $t_2 - t_1 \leq t_c$. This domain occupies a very small area in the bottom left corner of the design space. It has no substantive effect on the results for parameter values of present interest.

4.3 Model assessment

The fidelity of the preceding analytical model has been assessed through a combination of impact experiments on commercial foams and corresponding finite element simulations. Details of the materials and the test procedures are presented in Section 4.3.1. The finite element methods are described in Section 4.3.2. Results from both the experiments and the FEA are compared with the model predictions in Section 4.3.3.

4.3.1 Materials and test methods

Tests were conducted on three PVC-polyurethane foams (DivinyCell®). The materials are designated H45, H100 and H200 (the numerical values indicating the approximate mass density in kg/m^3). Their key properties are summarized in Table 4.1. The materials were procured as plates with thickness of either $25.7\,mm$ (H45) or $19.6\,mm$ (H100, H200). Square samples ($250\,mm\,x\,250\,mm$) were cut from the plates using a precision table saw.

Impact experiments were conducted using a standard instrumented head-form [21] mounted in a tripod drop system (Triax 2010, Alpha Automation Inc). The head-form was a hemi-spherical Aluminum body with $4.65\,kg$ mass and radius of $83\,mm$. An image of the tripod drop system and headform is shown in Figure 4.9. A 3-axis accelerometer in the head-form was used to measure acceleration-time histories during the impact event. The head-form was attached to the tripod using a flexible cable at prescribed heights above the sample surface. Three heights were used: $0.2, 0.82$ and $1.85\,m$, yielding impact velocities of $2, 4$ and $6\,m/s$, respectively. An electro-magnetic release mechanism was employed to allow smooth (rotation-free) release from the tripod. The samples were held fixed at the periphery using a steel picture-frame assembly. Side view high-speed video footage was taken with a Phantom video camera (Vision Research®) placed at a height level with the top of the foam. The videos were used to corroborate the accelerometer data. Either 2 or 3 tests were performed on each foam at each impact velocity. The test results proved to be highly reproducible.

In order to calibrate the material model for use in the FEA, the three foams were subjected to uniaxial compression tests at strain rates varying from $10^{-4}s^{-1}$ to $1\ s^{-1}$. The data were augmented by test results reported by Tagarielli *et al* [40] for some of the same foams at strain rates as high as $10^{4}\ s^{-1}$. The compression samples were square in cross-section with dimensions $50\ mm\ x\ 50\ mm$. The samples were compressed between two platens using a mechanical test frame (MTS®) at a fixed nominal strain rate.

For incorporation of the test data into the FE simulations, the uniaxial compressive properties of the foams were fit using the Gibson-Ashby model presented in Chapter 2 [35]. The plastic response in the hardening domain is again described by:

$$\frac{\sigma_f}{\sigma_{pl}} = \frac{1}{D}\left(\frac{\varepsilon_D}{\varepsilon_D - \varepsilon_f}\right)^m \tag{4.16}$$

where σ_f is the current axial stress, ε_f is the current axial strain and *m* is another fitting parameter (taken to be 1). The strain rate dependence of the plateau stress was fit to a power-law of the form:

$$\frac{\sigma_{pl}}{\sigma_o} = \left(\frac{\dot{\varepsilon}}{\dot{\varepsilon_o}}\right)^n \tag{4.17}$$

where $\dot{\varepsilon}$ is the strain rate, σ_o is a reference stress corresponding to at reference strain rate, $\dot{\varepsilon_o}$ (the latter chosen to be $10^{-2}\ s^{-1}$), and n is the power law exponent determined from the compression tests.

Representative results from the compression tests are plotted in Figure 4.5(a). Each of the three foams exhibits the three expected domains of behavior: elastic, perfectly-

plastic and strain hardening. The modulus and the plateau stress increase with foam density whereas the densification strain decreases. The foam strength varies by as a factor of 6.5 (from softest to hardest). The strain rate sensitivity data, plotted in Figure 4.5(b), show that the plateau stress for each of the three foams (normalized accordingly) follows the same (weak) rate sensitivity, characterized by a hardening exponent $n = 0.03$.

4.3.2 Finite element analysis

Finite element simulations of the impact tests were performed using explicit time-integration with the ABAQUS code [32]. All simulations were run with 4-noded bilinear axisymmetric quadrilateral elements (CAX4R) with reduced integration and hourglass control. A mesh sensitivity study was conducted in which the size of the elements was varied over a range of $100\ \mu m$ to $1\ mm$. Each simulation yielded nominally identical results. The pertinent parameter values of the impacting sphere and the foam are summarized in Table 4.1. The foam was represented by the Fleck-Deshpande crushable foam model as presented in Chapter 3 (with rate dependent behavior), and was implemented as a user material in the Abaqus code [32,34]. In order to attain a plastic Poisson's ratio of 0, the ratio of yield strengths in hydrostatic compression and uniaxial compression was taken to be $\sqrt{3}$. A non-associated flow potential was used, with parameters selected to also be consistent with a plastic Poisson's ratio of 0. The hardening of the foam was described by Eqn. (4.16) and its rate-dependence by Eqn. (4.17). The geometry of the finite element mesh was designed to match the test samples. The foam

was placed against a rigid backing plate with frictionless contact in the tangential direction and "hard" normal contact. Contact between the head-form and the foam was "hard" in the normal direction; tangential motion was allowed subject to a friction penalty coefficient $\mu_o = 0.2$. (Select simulations run with frictionless contact yielded virtually equivalent results). The initial velocity of the sphere was prescribed to match one of the three values employed in the experiments.

4.3.3 Blunt impact test results

Representative acceleration-time histories measured on each of the three foams at each of the three velocities are plotted in Figure 4.6. Repeat tests showed high reproducibility (the curves lying essentially within the thickness of the lines on Figure 4.6). The results exhibit the following trends. First, the peak acceleration for each foam increases approximately three-fold as the velocity is increased threefold (from 2 to 6 m/s). This proportional scaling is consistent with the prediction of Eqn (4.5). Second, the duration of impact for each foam is essentially independent of impact velocity, consistent with Eqn. (4.6). Third, the peak acceleration and the corresponding time follow the predicted scalings (in agreement with prior work [41]): $a_{max} \propto \sqrt{\sigma_o}$ and $t \propto 1/\sqrt{\sigma_o}$. That is, the ratio of peak accelerations of the hardest and the softest foams is about 2.6 (the predicted ratio being $\sqrt{6} \approx 2.5$). The duration time scales by the same amount.

Also shown on Figure 4.6 are the acceleration-time histories predicted by Eqn. (4.5), using foam strengths at a characteristic strain rate of $\dot{\varepsilon}_o = v_o/H_o$ s^{-1}, as well as the results of the finite element simulations. The agreement between the analytical model (based on the rigid-perfectly plastic representation of the foam response) and the FE results is excellent for the rising portions of all curves. The implication is that the effects of elasticity and rate dependence (weak in the present materials) are insignificant. The one discrepancy pertains to the post-peak response; the analytical model predicts a sudden drop to zero whereas the FE simulations show a more gradual drop during the rebound phase of the impact.

The agreement between the FEA simulations and the experimental results is excellent for the softest foam (H45) for all velocities. The shapes of the curves for the other foams show almost equally good agreement, though there appears to be a slight time-offset between the curves (about $0.5\ ms$). That is, shifting the FE curves to the right by about $1\ ms$ brings them into close agreement with the measured curves.

The HIC values obtained from the experiments (computed in accordance with Eqn. (4.1)) and both the analytical model and the numerical simulations are plotted in Figure 4.7. The agreement between FEA and the experiments is, again, very good (to within about 3%). The analytical model is almost as accurate as the FEA, though it underestimates the measured HIC values by $5-10\%$. This discrepancy is attributable to the absence of elastic deformation in the model and hence the inability of the model to capture the rebound phase of the impact event.

Some insights into the effects of elastic rebound on the HIC can be gleaned from comparisons of the times (t_1, t_2) bounding the HIC calculation with the time t_* at which the headform velocity reaches zero and thus the headform begins its rebound. (A representative set of these times are shown for one of the curves in Figure 4.6(b)). The expectation is that, if the latter event occurs outside the pertinent interval (notably, $t_* > t_2$), the rebound phase would have no effect on the HIC. Otherwise, if $t_1 < t_* < t_2$, an assessment of the relative time within the HIC interval occupied by the rebound phase can be characterized by a non-dimensional time parameter, τ_E, defined by:

$$\tau_E = \frac{t_2 - t_*}{t_2 - t_1} \tag{4.18}$$

Figure 4.8 shows the values of τ_E obtained from the experiments. (Here t_* was computed by integrating the measured acceleration-time histories.) The results show that τ_E increases with foam density – from about 0.15 for H45 to about 0.3 for H200 – and appears to be only weakly dependent on velocity. The cases in which the lowest values of τ_E are obtained are also those for which the error in the predicted HIC is lowest, and vice versa. This trend is consistent with the notion that the slight discrepancies between predicted and measured HIC values is associated with absence of elasticity in the model.

4.4 Discussion

In this chapter, an analytical framework has been developed to assess the efficacy of crushable foams in mitigating risk of serious head injury during blunt impact. During

such an impact, the contact area increases approximately linearly with penetration distance. This causes the acceleration to vary approximately sinusoidally with time up to its peak value. The model also predicts that the acceleration will drop precipitously from the peak to zero. Despite its seeming simplicity, the model predicts the acceleration-time histories and the HIC values to within 10% for the three foams tested in this study. The experimental results are better represented by the finite element simulations, where the elasticity effects have been naturally incorporated.

The slight underestimate of the predicted HIC has been attributed to the elasticity of the foams and the resulting rebound of the headform. The time scale associated with rebound within the interval used for calculating the HIC has been identified for the three foams of present interest and characterized by a non-dimensional time parameter. This parameter increases with increasing foam density: consistent with the trend of increasing errors in predicted HIC values.

In addition to guiding the selection of foams for optimal head protection during impact, the present model can be used to glean insights into composite systems that could be employed to further reduce the HIC relative to the present "optimized" values. This topic is discussed in Chapter 5.

Table 4.1: Material properties for Divinycell® foams

	Density $\left({}^{kg}/_{m^3}\right)$	Modulus (MPa)	Strength (MPa)	Poisson's Ratio ν
DivinyCell H45	48	25	0.63	0.33
DivinyCell H100	100	70	2.04	0.33
DivinyCell H200	200	135	4.09	0.33
Impact Sphere	2700	68,000	240	0.3

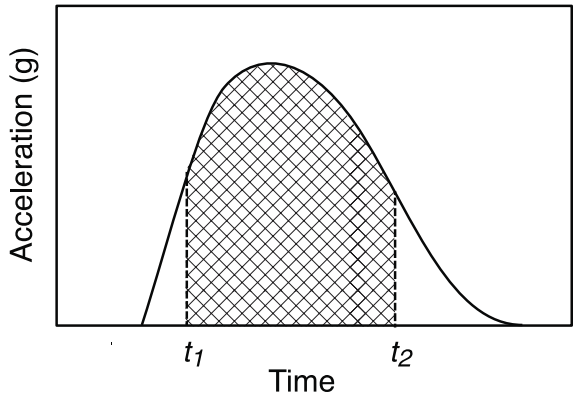

Figure 4.1: Schematic of acceleration-time profile and the two times bounding the calculation of the *HIC*.

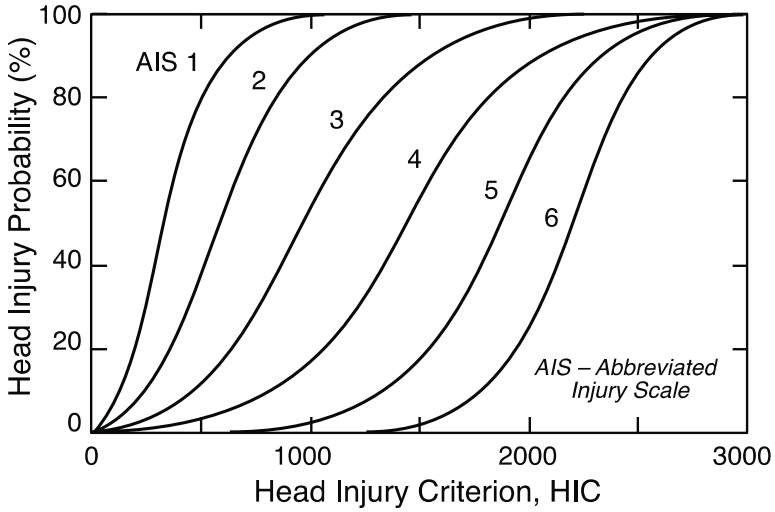

Figure 4.2: Effects of HIC on probability of sustaining head injuries of varying severity (from 1 to 6 on the Abbreviated Injury Scale). The Abbreviated Injury Scale was developed by the Association for the Advancement of Automotive Medicine. On this scale, 1 is minor and 6 is fatal. (Adapted from [8])

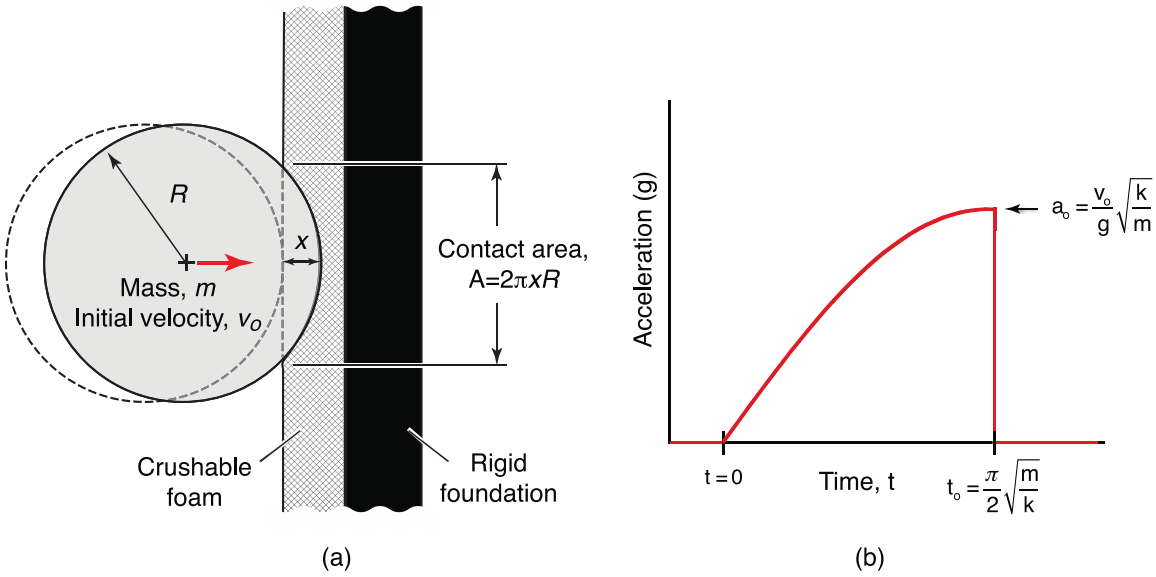

Figure 4.3: Schematic of impact of a spherical body onto a flat foam plate supported by a rigid foundation. (b) The predicted response for a rigid-perfectly plastic foam before densification.

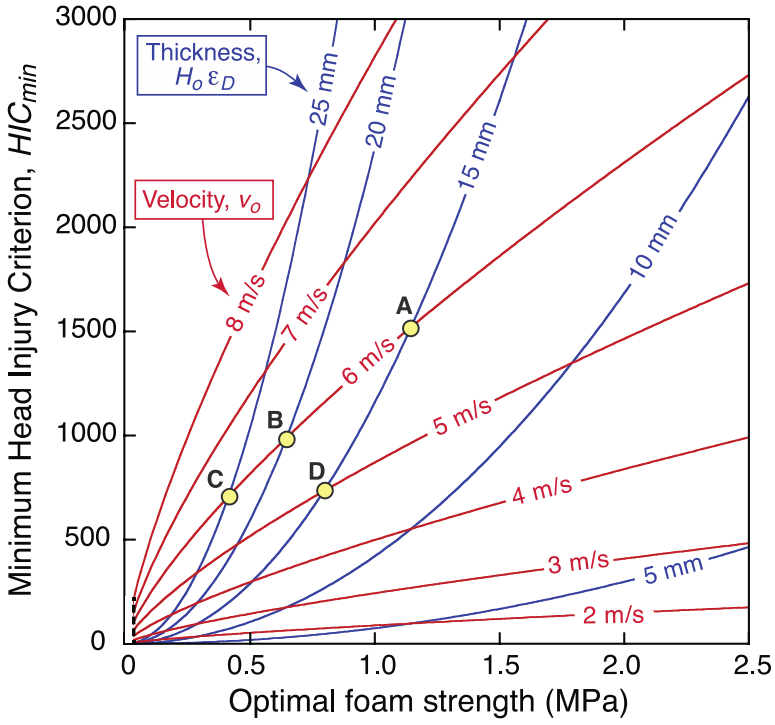

Figure 4.4: Design map showing the optimal foam thickness and foam strength needed to minimize the *HIC* for specified velocity (R=0.1 m, m=4.5 kg). Points **A**–**D** are described in the text. The dashed line in the lower left region marks the boundary beyond which the HIC calculation violates the time restriction $t_2 - t_1 \pounds t_c$.

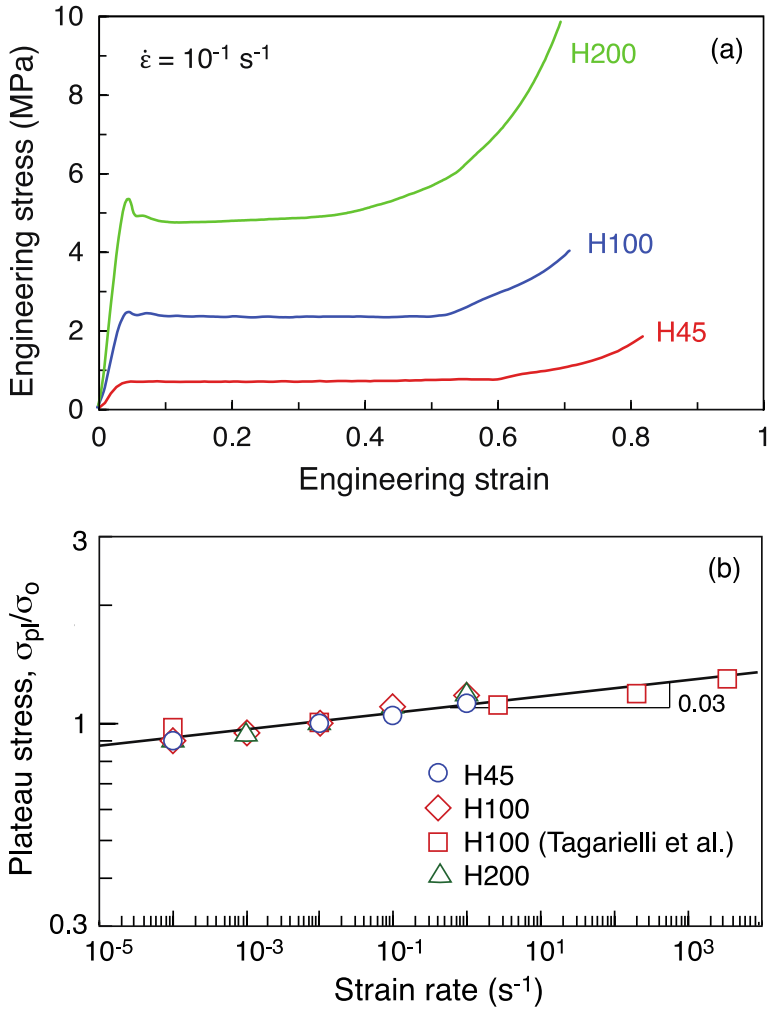

Figure 4.5: (a) Representative compressive stress-strain curves for DivinyCell® foams at one strain rate. (b) Effects of strain rate on the plateau (crushing) stress. Plateau stresses have been normalized by their respective values at $\dot{\varepsilon}_o = 10^{-2}\ s^{-1}$.

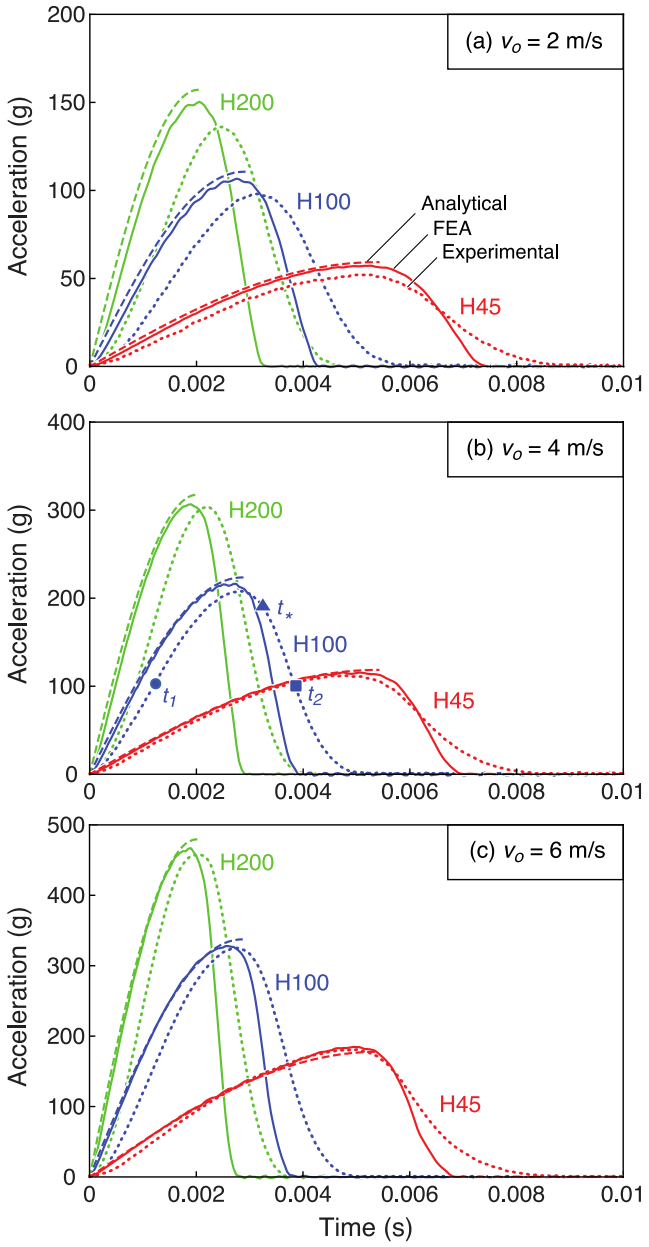

Figure 4.6: Acceleration-time histories for impact of all foams at three impact velocities. Dotted lines – experimental measurements; dashed lines – analytical model; solid lines – FEA. (Note the different acceleration scales on the three graphs.)

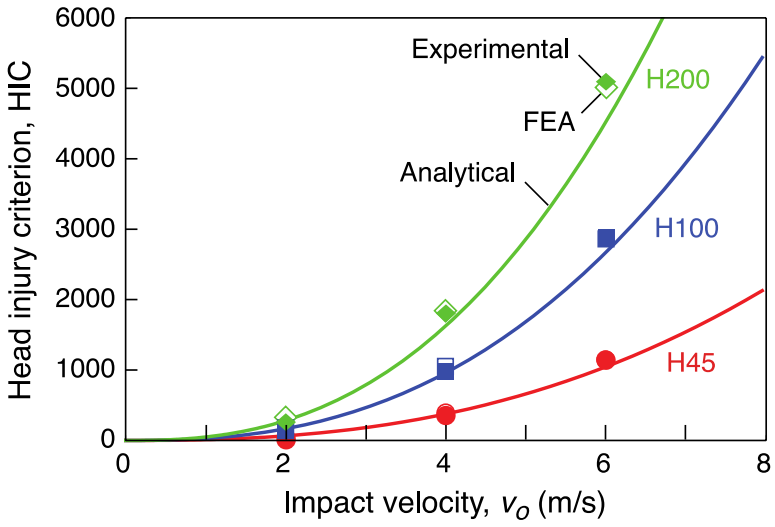

Figure 4.7: Measured and predicted HIC values for impact on DivinyCell® foams. Solid symbols – experimental measurements; solid lines – analytical model; open symbols – FEA.

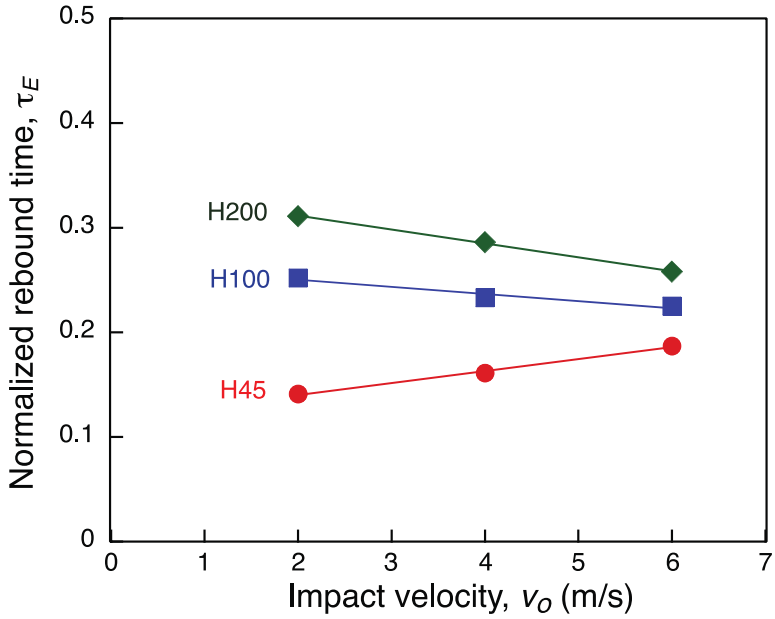

Figure 4.8: Fractional time within the HIC interval spent in rebound.

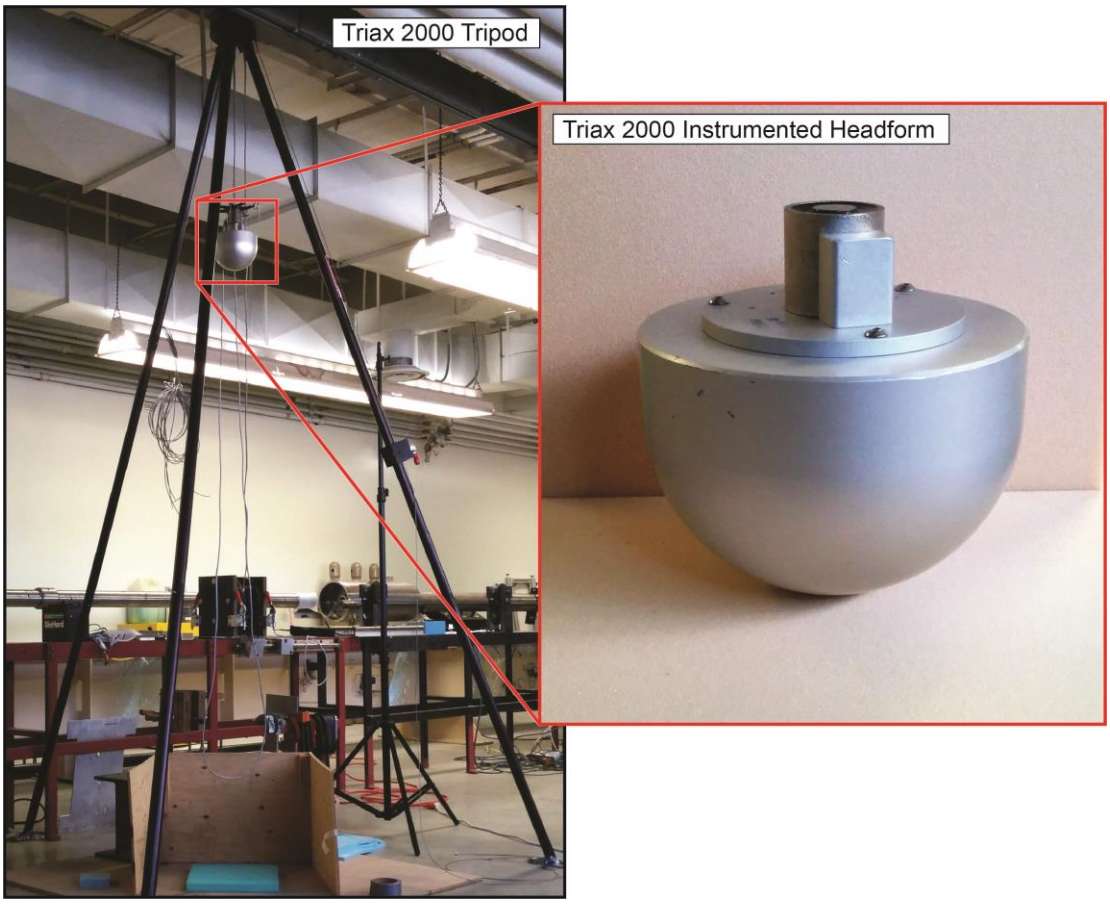

Figure 4.9: Triax 2000 surface impact test setup (left) and instrumented headform (right).

Chapter 5

Composite material systems for mitigating head injury

5.1 Introduction

In Chapter 4, a model was presented to guide the selection of foams for mitigating head injury. The optimum foam strength, σ_o^{opt}, that minimizes the HIC was ascertained for given constraints on the maximum allowable foam thickness (H_o) and impact velocity (v_o). This chapter explores composite systems for reducing the HIC relative to systems containing foams alone.

In the prior analysis, contact between the impacting "head" and the target was assumed to be spherical, as shown in Figure 5.1(b). This leads to acceleration-time profiles that are approximately sinusoidal in shape (Figure 5.2(b)). In light of the fact that the HIC is far more sensitive to acceleration than to impact duration, it follows that the HIC could be reduced further by transforming the sinusoidal acceleration-time history into one with a "top hat" profile (ie with acceleration being constant), as shown in

Figure 5.2(a). Theoretically, this could be achieved by tailoring the compressive properties of the foam to yield high peak crushing stress followed by strain softening, as described elsewhere [24]. Alternatively, it could be achieved through the addition of thin stiff sheets to the foams, configured to spread the load laterally during the impact event. The simplest example is a system in which a stiff faceplate is adhered onto the impact face of the foam. Assuming that plate bending is negligible, the impact load would be spread essentially uniformly in the foam over the area defined by the plate dimensions. This problem is analogous to a cylindrical slug impacting a foam that is mounted on a rigid plate (Figure 5.1(a)). The expectation then is that the stress resisting impact and the corresponding acceleration would be essentially constant over the duration of the event.

The principal objective of this chapter is to assess the benefits of composite materials systems over foam-only structures in reducing the HIC. The scope is restricted to impacts with an initial velocity $v_o = 6.7\ m/s$. This represents the approximate speeds during the secondary impact of a vehicle occupant with the cabin interior in blast impact scenarios. An analytical model for the impact of a cylindrical mass on a foam is developed in Section 5.2. This model sets a theoretical bound for the reduction in HIC by utilizing a "plate-on-foam" design. Experimental results of impact tests are presented in Section 5.3, with comparisons to the theoretical limits predicted by the analytical model.

5.2 Analytical model of impact

The potential benefit of the plate-on-foam strategy can be readily ascertained through an analysis closely analogous to that presented in Section 4.2. The analysis begins with a one-dimensional analysis of impact of a flat-ended cylindrical body of radius *R* and mass *m* and a flat crushable foam pad mounted on a rigid support (Figure 5.1(a)). The foam is assumed to either be rigid/perfectly-plastic with a crushing stress σ_o up to the densification strain, ε_D. Thereafter, at higher strains, the foam behaves again as a rigid solid. The foam pad is further assumed to be sufficiently thick (defined below) so that full densification does not occur before the mass arrests. As stated in Chapter 4, the pad thickness inherently acts as a constraint, since thicker pads of softer materials will always lower the HIC value but introduce impractical solutions. In this case, the solution to the equation of motion is simply:

$$a = a_o = \frac{-\ddot{x}}{g} = \frac{\sigma_o \pi R^2}{mg} \tag{5.1}$$

over the time interval

$$0 \le t \le t_o = \frac{m v_o}{\sigma_o \pi R^2} \tag{5.2}$$

In order for arrest to precede densification, the thickness of the foam pad must exceed a critical value, given by

$$H_o = \frac{x_{max}}{\varepsilon_D} = \frac{m v_o^2}{2\sigma_o \pi R^2 \varepsilon_D} \tag{5.3}$$

The two times that maximize HIC are $t_1 = 0$ and $t_2 = t_o$. Integrating Eqn. (4.1) yields:

$$HIC = \left(\frac{\sigma_o \pi R^2}{mg}\right)^{3/2} \left(\frac{v_o}{g}\right) \tag{5.4}$$

The HIC decreases monotonically with decreasing foam strength, but this comes at the expense of an increasing minimum thickness. The minimum value of the HIC is obtained when the foam thickness is *at* its minimum critical value:

$$HIC_{min} = \left(\frac{{v_o}^4}{(2H_o\varepsilon_D)^{3/2}\, g^{5/2}}\right) \tag{5.5}$$

It is attained when the foam crushing stress is at its optimal value, given by:

$$\sigma_o^{opt} = \left(\frac{m{v_o}^2}{2\pi R^2 H_o \varepsilon_D}\right) \tag{5.6}$$

Comparison with Eqn (4.14) reveals that the HIC in Eqn (5.5) is reduced by a factor of $1/1.84 \approx 0.54$. Reductions of this magnitude in head protection systems would have very significant benefits in reducing the risk of serious head injury during impact.

An analogous solution exists for the impact of a spherical body on a composite system incorporating a rigid plate. Here, the plate is bonded to the foam such that the contact geometry is altered from the spherical case, presented in Chapter 4, to that of the cylindrical analysis presented above. The analysis remains unchanged, but now the contact area of the cylindrical slug is replaced by the area of the rigid plate, A_p. Equations 5.4 and 5.6 can now be rewritten in terms of A_p:

$$HIC = \left(\frac{\sigma_o A_p}{mg}\right)^{3/2} \left(\frac{v_o}{g}\right) \tag{5.7}$$

and

$$\sigma_o^{opt} = \left(\frac{m{v_o}^2}{2A_p H_o \varepsilon_D}\right) \tag{5.8}$$

It is important to note that Eqn. 5.5, defining the minimum HIC that is attainable, remains unchanged.

5.3 Experiments

The preceding model has been assessed through impact experiments on several commercial foams and composites systems. Details of the materials and the test procedures are presented in Section 5.3.1. Results from experiments are compared with the model predictions in Section 5.3.2.

5.3.1 Materials and test methods

Tests were conducted on four viscoelastic polyurethane foams (SunMate®). The materials are designated Firm, XFirm, XXFirm, and T50E. The density of all of the foams is approximately 88 kg/m^3, and their key properties are summarized in Table 5.1. The quasi-static compressive stress-strain response of the foams is shown in Figure 5.3. The materials were procured as plates with a thickness of 38.1 mm . This choice was made on the basis that, in many protective systems, the foam thickness is likely larger than 25 mm, but limited to 50 mm. Thus, an average value of 38.1 mm was used for the present study. Square plates of varying sizes ($75 - 150\ mm\ x\ 75 - 150\ mm$) were cut from the plates using a precision table saw. Square plates of equal

size were cut from panels of Dyneema® HB26 and carbon fiber reinforced plastic (CFRP). Both the Dyneema® and CFRP plates were approximately 3.3 mm in thickness. For tests conducted on samples comprising plates and foams, the plates were adhered to the foam using a commercial off-the-shelf epoxy resin (Devcon®).

Impact experiments were conducted in a method identical to the procedure described in Chapter 4 using an instrumented head-form mounted in a tripod drop system (Triax 2010, Alpha Automation Inc). The head-form was dropped from a height of 2.3 m, yielding impact velocities of approximately 6.7 m/s. This velocity is representative of impact velocities observed in most automobile collisions. An electro-magnetic release mechanism was employed to allow smooth (rotation-free) release from the tripod. The samples were held fixed at the periphery using duct-tape. Side view high-speed video footage was taken with a Phantom video camera (Vision Research®) placed at a height level with the top of the foam. The videos were used to corroborate the accelerometer data. Either 2 or 3 tests were performed on each foam and plate-on-foam composite. The results were found to be very reproducible, yielding HIC values that were within $5-10\%$ of one another.

A series of preliminary tests was conducted to identify the appropriate sizes of the composite specimens. From Eqn. (5.8), the optimal tile area is expected to scale inversely with foam strength. This led to the selection of smaller tiles for the stronger foams and vice-versa. Specifically, tile dimensions of 150 $mm\ x$ 150 mm were used with both the Firm and the XFirm foams, 100 $mm\ x$ 100 mm for both the XFirm and XXFirm foams, and $75mm\ x$ 75 mm for both the XXFirm and T50E foams. (These

combinations are also summarized in the legend inset in Figure 5.8.) (Because the models presented here are rather rudimentary – neglecting effects of face-sheet bending, elastic recovery and strain rate sensitivity – they are used only to *guide* the design. Optimization would require more rigorous analysis of the impact.)

5.3.2 Blunt impact test results

Representative acceleration-time and displacement-time histories measured on three of the foams are shown in Figure 5.4. The displacements (measured relative to the point of initial contact) are normalized by the thickness of the foam pad and thus represent the maximum nominal strain beneath the contact site. The results exhibit the following characteristics.

(i) The initial rise of the acceleration-time curve scales approximately linearly with the quasi-static foam strength, in accordance with Eqn. (5.5). (ii) For the softest foam, the initial nearly-linear rise is followed by a rapid upturn in acceleration, to a peak value of almost $290g$. The upturn is attributable to full densification of the foam and "bottoming out" of the head-form, as evidenced by a peak displacement $x_{max}/H_o \approx 0.83$. (iii) The foam of intermediate strength does not exhibit an upturn in acceleration rate, consistent with the peak displacement being less (albeit only slightly) than that needed for full densification ($x_{max}/H_o \approx 0.7$). Consequently, the peak acceleration is reduced to about $160g$ and the HIC reduced from 1500 to 900. Furthermore, the curve shape (up to the peak) is broadly consistent with that predicted by Eqn. (5.5) and plotted in

Figure 5.2(a). (iv) The response of the strongest foam is similar to that of the intermediate foam, with the exception of a brief plateau shortly after contact. Its shape is attributable to the strain softening of the foam after yielding, as evident in Figure 5.3. Further reductions are obtained in both the peak acceleration, to $130g$, and the HIC, to 700.

The acceleration- and displacement-time histories measured on three CFRP-foam systems are shown in Figure 5.5. All behave in a similar manner. The acceleration rises sharply to a plateau and then gradually increases to the peak. The peak accelerations and HIC values are lower than those of the foam alone. The effects are most pronounced for the softest foam: the acceleration dropping from $290g$ to $120g$ and the HIC dropping from 1500 to 750. Here again the peak displacements are maintained below the levels needed for significant densification.

Figure 5.6 shows the results for the Dyneema®/XXFirm foam composites. To provide direct comparison, the results for the XXFirm foam alone and the CFRP/XXFirm foam composite are reproduced on this figure. The curves for the two composite systems are very similar to one another and produce nearly-equivalent HIC values. Additionally, both systems yield lower HIC values than that of the foam alone (750 vs. 950).

Figure 5.11 shows the impact and rebound process for impact with the XXFirm and Firm foams at equivalent time intervals. At $t = 24\ ms$, the headform has achieved a higher rebound height after impact with the Firm foam (Figure 5.11(b)). Some insights into the effects of elastic rebound on the HIC can be gleaned from comparisons of the

times (t_1, t_2) bounding the HIC calculation with the time t_* at which the headform velocity reaches zero and thus the headform begins its rebound. The expectation is that, if the latter event occurs outside the pertinent interval (notably, $t_* > t_2$), the rebound phase would have no effect on the HIC. Otherwise, if $t_1 < t_* < t_2$, an assessment of the relative time within the HIC interval occupied by the rebound phase can be characterized by a non-dimensional time parameter, τ_E, defined by:

$$\tau_E = \frac{t_2 - t_*}{t_2 - t_1} \tag{5.9}$$

Figure 5.7 shows the variation of τ_E with the quasi-static (QS) foam strength. Here τ_E decreases with the increasing foam strength, from about 0.25 for the Firm foam to about 0.12 for the T50E foam. These values indicate that the rebound plays only a small (though perhaps not insubstantial) role in the HIC value. They are further consistent with the asymmetry of the acceleration-time histories (Figures 5.4-5.6); if foam elasticity dominated the impact response, the acceleration-time histories would be perfectly symmetric about the peak. The addition of a face-sheet alters τ_E by only a small amount ($\leq$0.05). Adhering a CFRP plate to the foams increases τ_E, whereas coupling with a plate of Dyneema® HB26 reduces the value (relative to the XXFirm foam alone). Lastly, signs of (macroscopic) failure via matrix cracking is observed in the CFRP plates after multiple impacts, as shown in Figure 5.10(b). The operative failure mode in the Dyneema® plates is separation of the laminae at the boundary of the plate, with significant plastic deformation after a single impact test (Figure 5.10(a)). In this

regard, the CFRP plates may be better suited for systems that require multi-hit capability.

The HIC values for the foams alone and the foam/face-sheet composites are plotted in Figure 5.8(a) and (b), respectively. Also shown are the predictions of the analytical models: Eqn. (4.12) for the foams alone and Eqn. (5.7) for the face-sheet/foam composites. The model predictions are shown only in the domain in which full densification (taken as the point at which the strain reaches 0.8) does not occur. Full densification and head-form "bottoming out" at low foam strengths leads to an increase in HIC: a feature not captured by the present models.

The experimentally-measured HIC for the foams decreases with increasing foam strength and appears to approach a minimum for the hardest foam. This minimum coincides closely with the minimum predicted HIC, albeit the predicted minimum occurs at a slightly higher foam strength. The latter difference can be attributed in part to the strain rate sensitivity of the foam response. That is, the pertinent foam strength for comparing the measurements with the model predictions should be the one at the average strain rate obtained in the impact tests (about 200 s^{-1} in the present experiments[3]). The trend in the experimental measurements is associated with the larger strains obtained under the impact site for the softer foams and hence the increasing propensity for bottoming out of the head-form. A further inference is that, upon increasing the

[3] Taking the strain rate dependence of the foam strength to follow a power law with an exponent typical of viscoelastic foams (0.05–0.1), the predicted strength at $200s^{-1}$ becomes about twice that measured quasi-statically (at 0.01 s^{-1}). A two-fold shift in the foam strengths in Figure 8(a) would bring the measured HIC for the T50E foam in close correspondence with the minimum point predicted by the model.

foam strength beyond that of the T50E, the HIC would again start to rise. It would thus appear that the T50E is nearly optimal for the present loadings (ie. mass, radius and velocity of head-form) and the selected foam thickness.

Qualitatively similar trends are obtained for the measurements on the foam/face-sheet composites, with additional effects arising from the tile size. Here, again, the *HIC* initially decreases with increasing foam strength. Furthermore, the HIC decreases with increasing tile size. Presumably it, too, will reach a minimum value at higher foam strengths, given by Eqn. (5.5) and indicated by the dashed black line in Figure 5.8(b). The difference between the lowest measured value of HIC (650) and the predicted minimum (420) suggests room for further improvement, through a combination of increasing foam strength and/or increasing tile size.

5.4 Discussion

In this chapter, a new concept that has the potential for reducing the severity of head injury during blunt impact has been presented. The efficacy of the concept has been assessed by comparing measured *HIC* values for several commercial foams and several foam/face-sheet composites, at an impact velocity relevant to vehicle occupants in automobile collisions. A rudimentary model of the acceleration-time history has also been presented. The model serves as the motivation for the experimental study and provides context for the experimental measurements. The key conclusions follow.

(i) Among the foams considered here, the T50E performs best and its *HIC* appears to be close to the theoretical minimum for the prescribed foam thickness (38 mm).

(ii) The addition of stiff face-sheets to the foams leads to a predicted potential reduction in *HIC* of almost a factor of two. Although comparable reductions in *HIC* have indeed been obtained in some instances, comparisons between the measurements and the predictions suggest further room for improvement.

(iii) The effects of elastic rebound on the HIC measurements appear to be relatively small, in the sense that the rebound phase comprises only a small part of the pertinent duration of the impact event and that the rebound velocity is only a small fraction of the incident velocity.

(iv) Although the correspondence between the experimental measurements and the theoretical predictions appears reasonable, there remains a need to develop more rigorous models that account for higher-order effects, including the strain rate sensitivity of the foam strength, the finite strain hardening of the foams at strains approaching densification, and the effects of elastic bending and rebound of the face-sheets.

The analytical framework presented in this chapter can be used to construct design maps based on the foam strength, foam thickness, impact velocity, and plate dimensions. Two such maps, showing the variation in HIC with foam strength, were presented in Figure 5.8. Yet another is shown in Figure 5.9, wherein the foam strength and thickness have been held constant at realistic values ($\sigma_o = 0.6\,MPa, H_o\varepsilon_D =$

31.4 mm). This design map shows the analytical predictions of the variation in HIC with impact velocity for spherical impact and planar impact for three plate sizes. The HIC varies linearly with impact velocity in the planar contact model. For spherical contact, however, the HIC is much more sensitive to the impact velocity, with $HIC \propto {v_o}^{2.5}$. The dashed segments represent the maximum velocities for each system that prevent full densification in the foam. This map demonstrates the range of impact velocities for which a chosen plate size yields reductions in HIC relative the foam alone. For example, at an impact velocity of 7 m/s, only a marginal reduction in the HIC can be achieved by coupling the foam with a 100 $mm\ x$ 100 mm plate. However, it increases the maximum impact velocity from 8.17 m/s to 9.17 m/s. In contrast, a 90 $mm\ x$ 90 mm plate leads to a 30% reduction in the HIC, but limits the maximum impact velocity to 8.12 m/s.

Table 5.1: Material properties for SunMate® foams

	Density $\left({}^{kg\ m}/_{s^2}\right)$	Modulus (MPa)	Strength (MPa)	Poisson's Ratio ν
SunMate® Firm	88	0.6	0.015	0.33
SunMate® XFirm	88	1.1	0.025	0.33
SunMate® XXFirm	88	2	0.069	0.33
SunMate® T50E	88	6	0.196	0.33

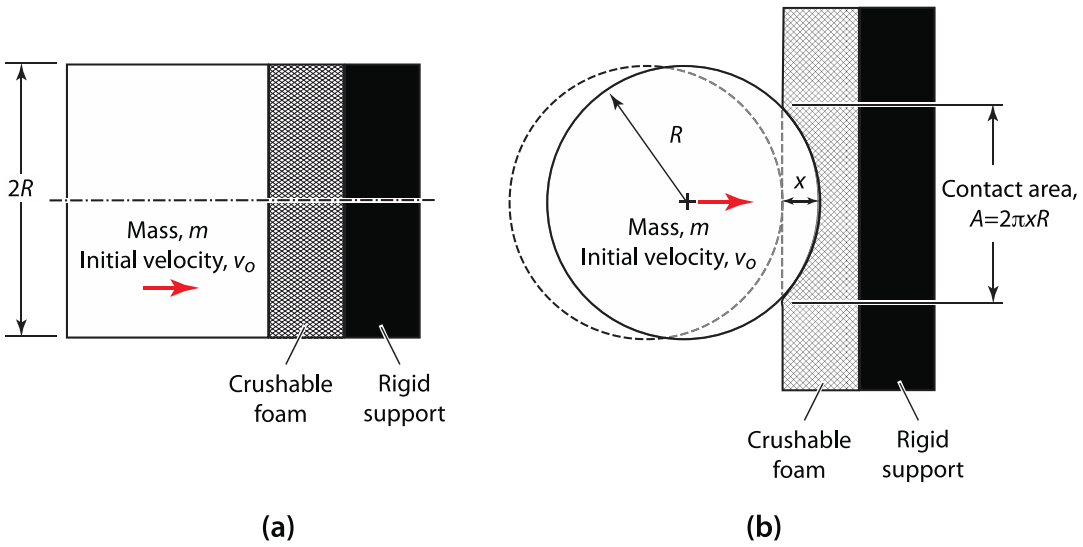

Figure 5.1: Two impact idealizations: (a) a flat-ended cylindrical slug and (b) a spherical mass, impacted onto a crushable foam pad mounted on a rigid flat support.

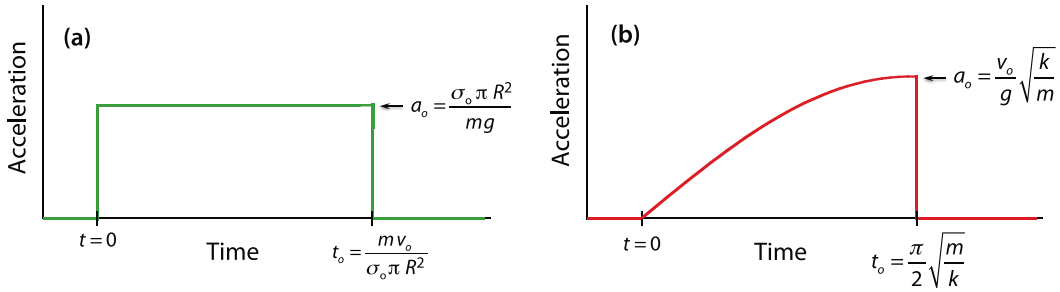

Figure 5.2: Acceleration-time profiles for (a) flat contact and (b) sphere impact, subject to the assumption that arrest precedes densification.

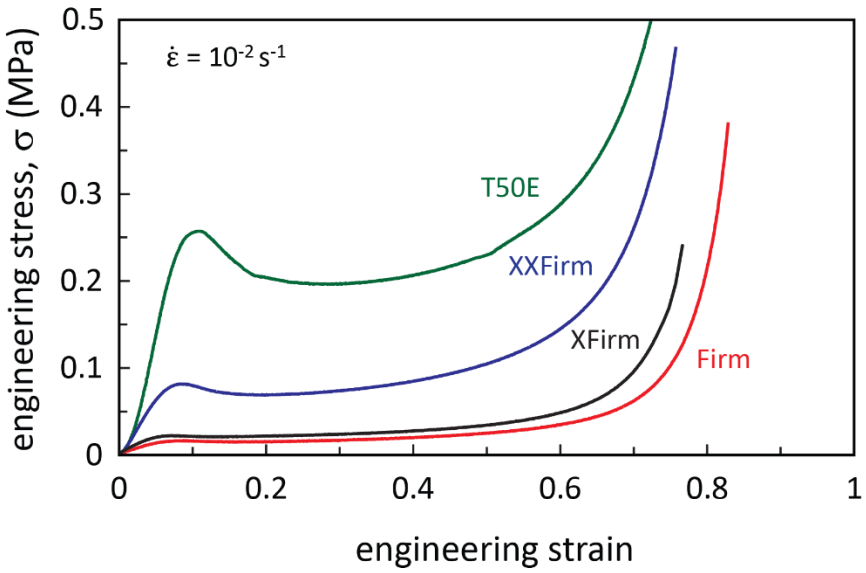

Figure 5.3: Representative compressive stress-strain curves for SunMate® foams under quasi-static loading rates ($\dot{\varepsilon} = 10^{-2}s^{-1}$).

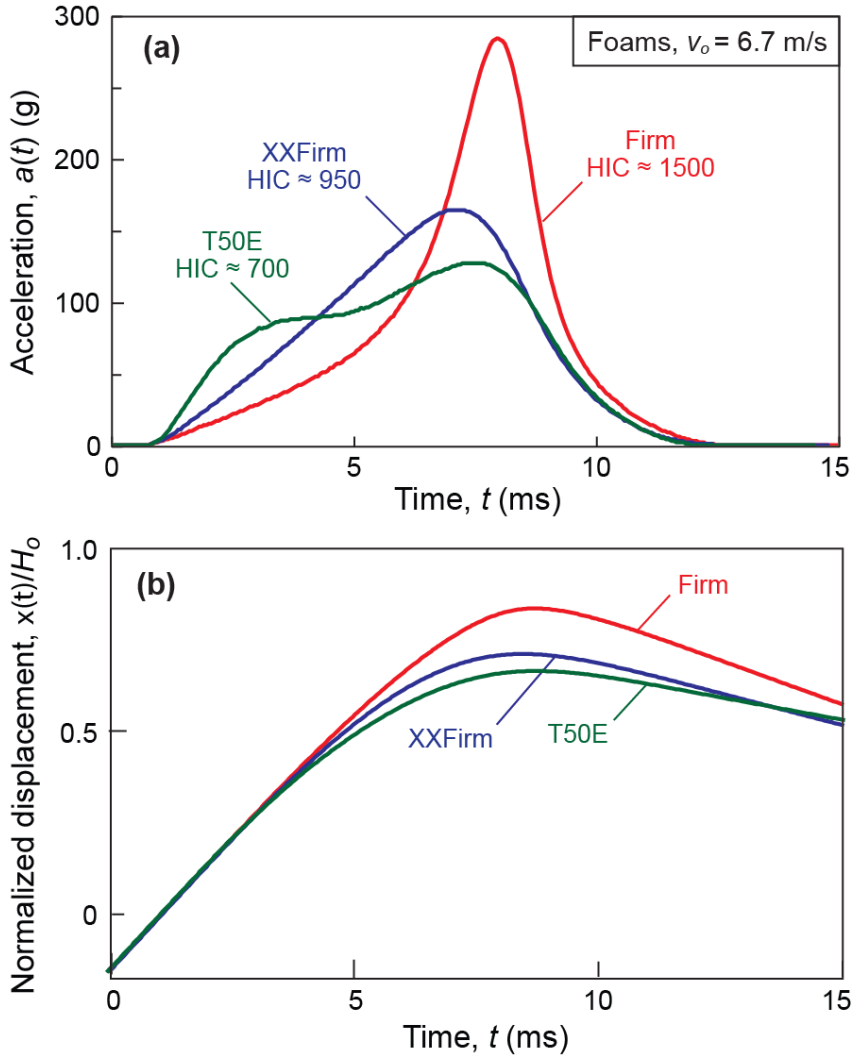

Figure 5.4: Experimental measurements of acceleration- and displacement-time histories at an impact velocity $v_o = 6.7\ m/s$ for three SunMate® foams.

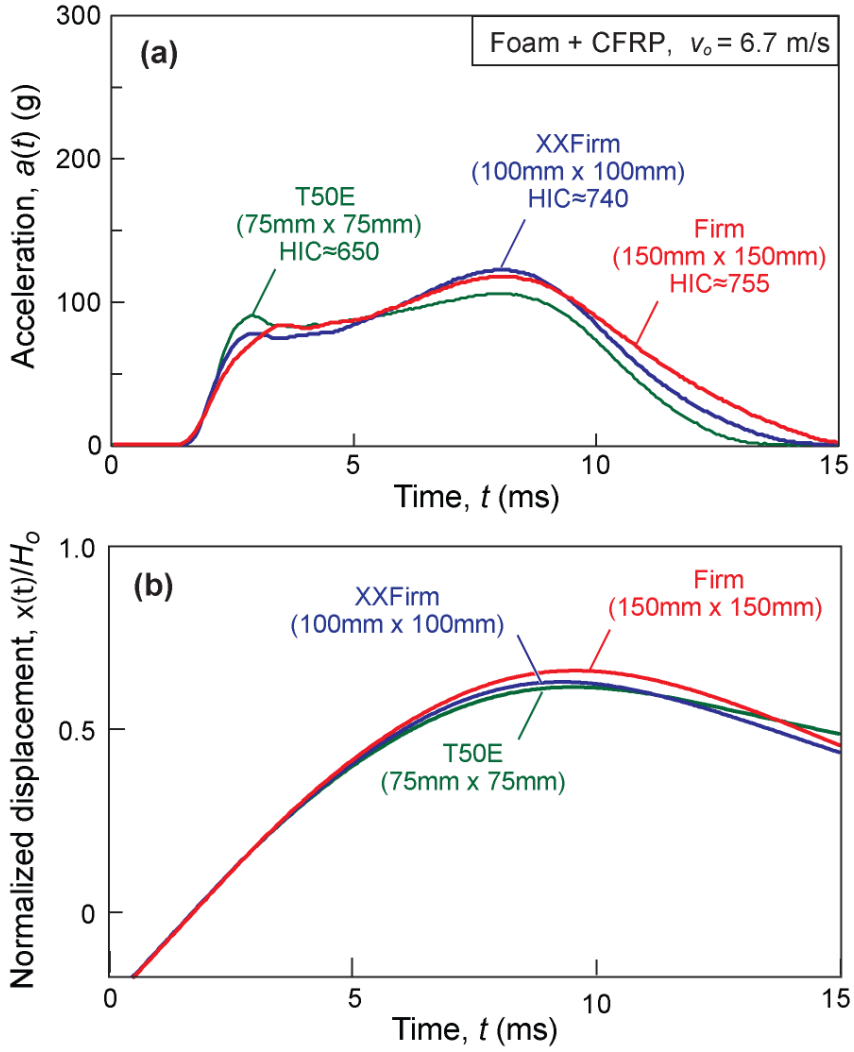

Figure 5.5: Experimental measurements of acceleration- and displacement-time histories at an impact velocity $v_o = 6.7\ m/s$ for three CFRP/foam (SunMate®) composites.

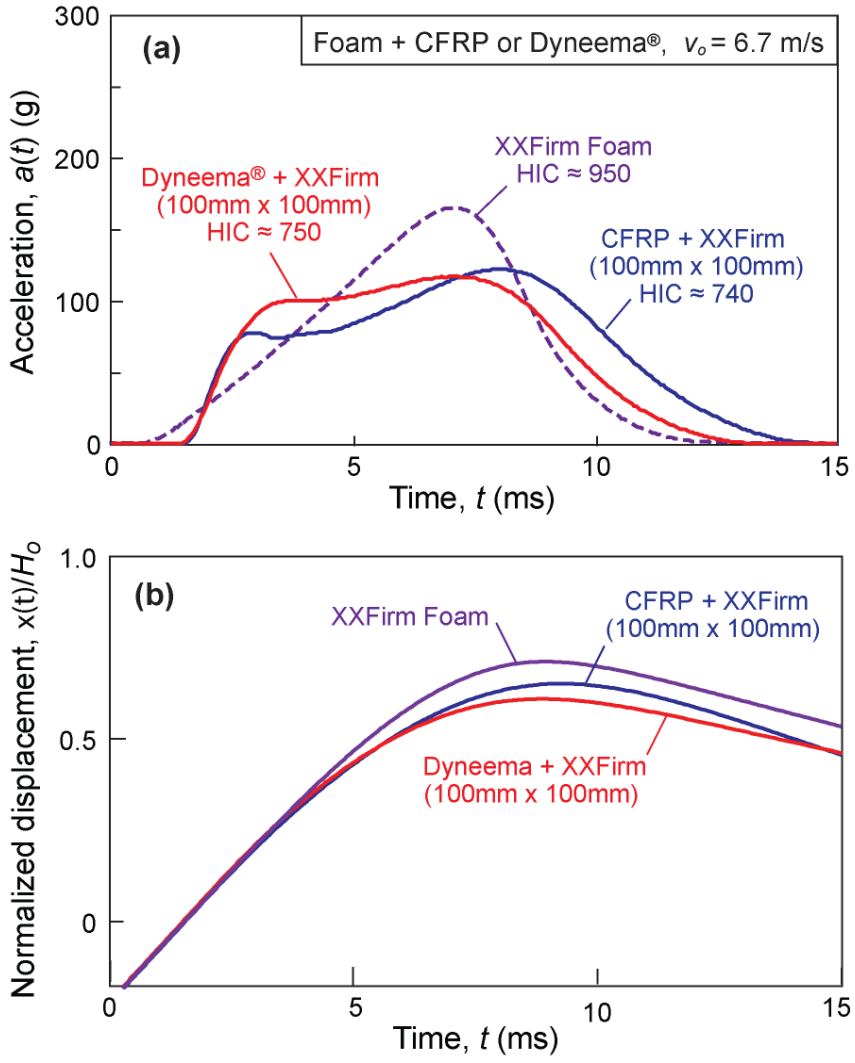

Figure 5.6: Effects of face-sheet material – Dyneem® vs. CFRP – on impact test results: acceleration- and displacement-time histories at an impact velocity $v_o = 6.7\ m/s$.

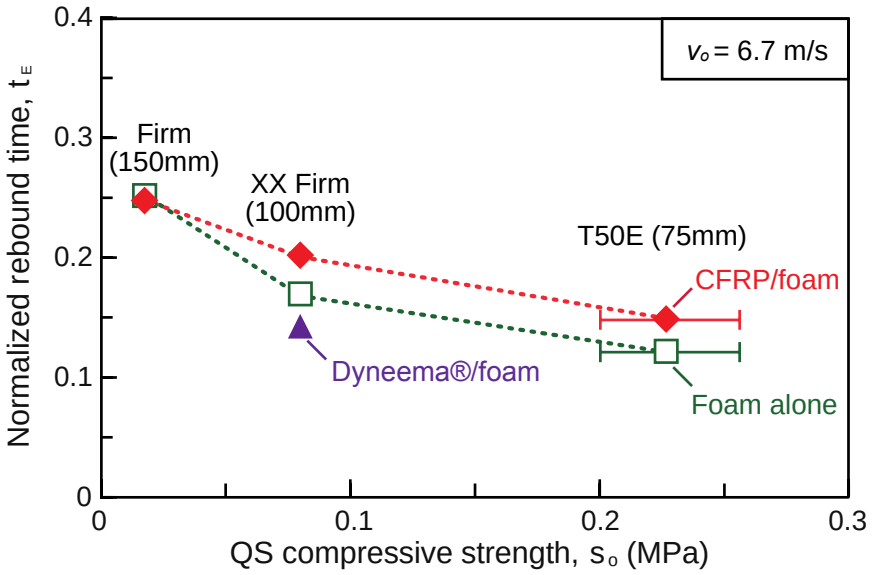

Figure 5.7: Effects of elastic rebound: fractional time within the HIC interval spent in the rebound phase. (The error bars for T50E represent the range of crushing strengths from the initial peak to the subsequent plateau, at a strain $\varepsilon = 0.2$, as seen in Figure 5.3)

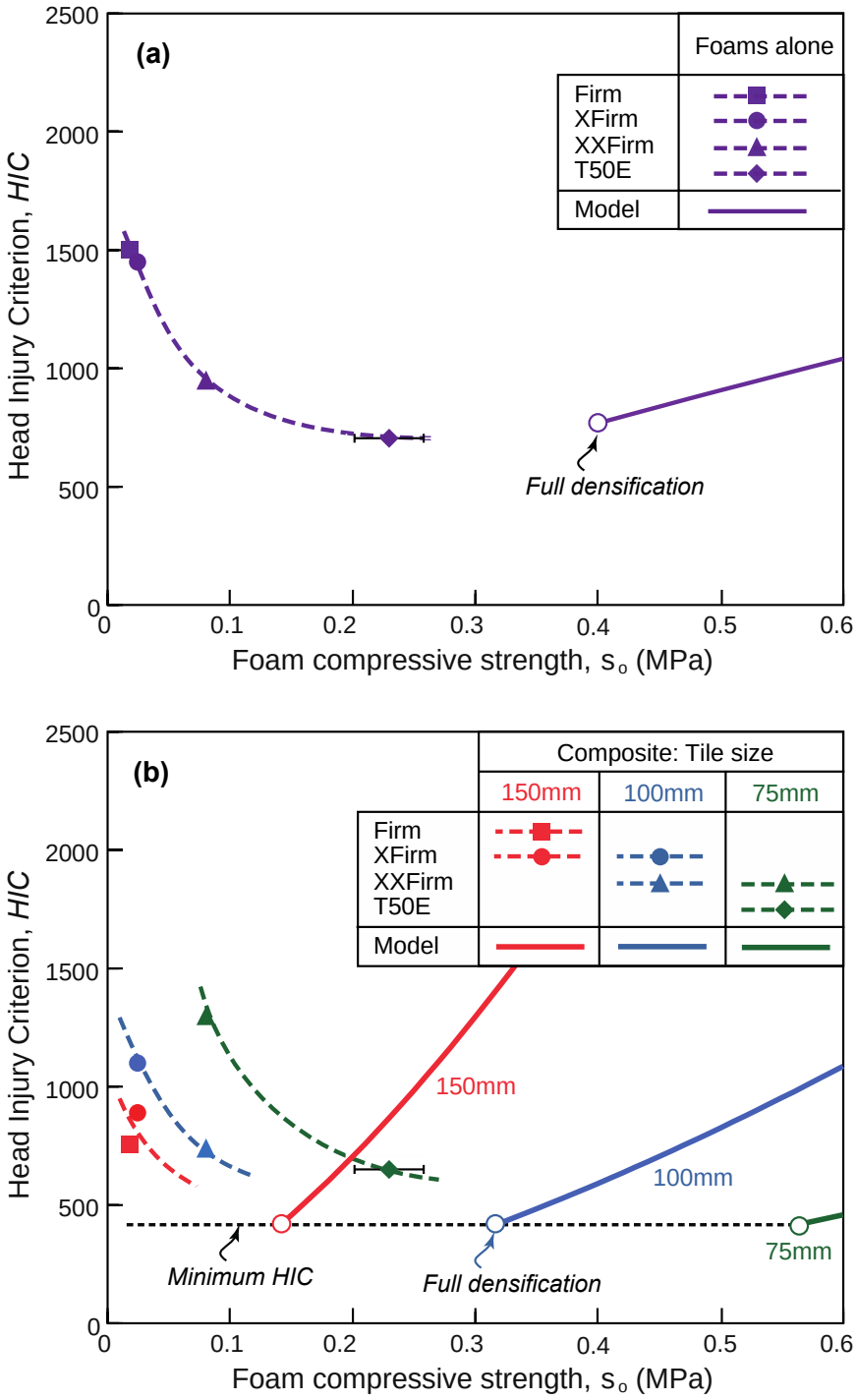

Figure 5.8: Variation in *HIC* with foam strength for (a) foams alone and (b) foam/face-sheet composites, from experimental measurements (filled symbols) and model predictions (solid lines).

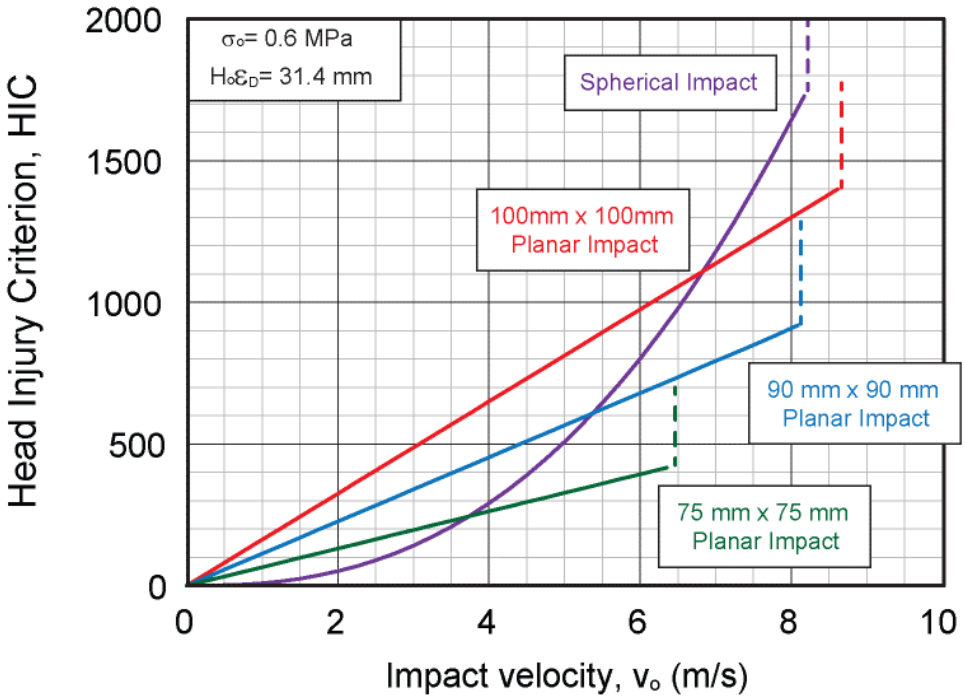

Figure 5.9: Analytical predictions of the variation in HIC with impact velocity for planar and spherical contact geometries.

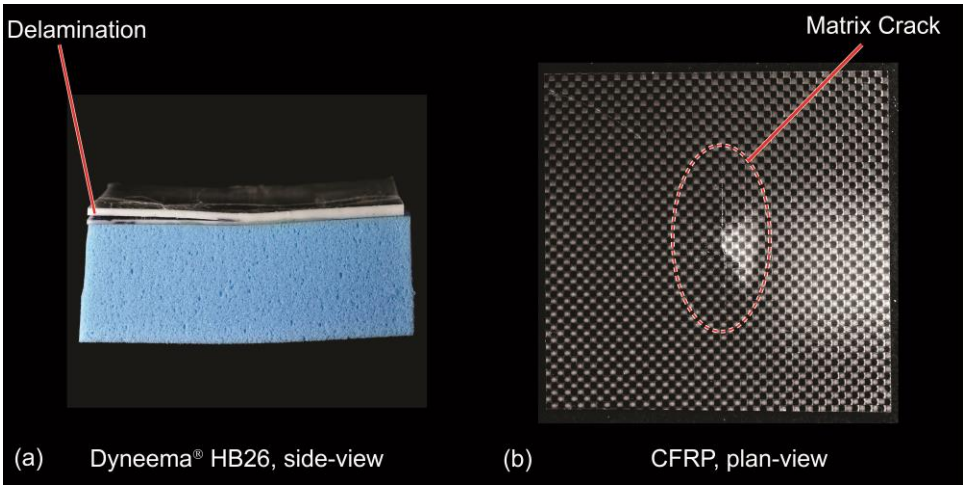

Figure 5.10: Images showing damage in the composite plates due to bending: (a) delamination at the boundary of the Dyneema® HB26 plate and (b) matrix cracking at the center of the back face in the CFRP plate.

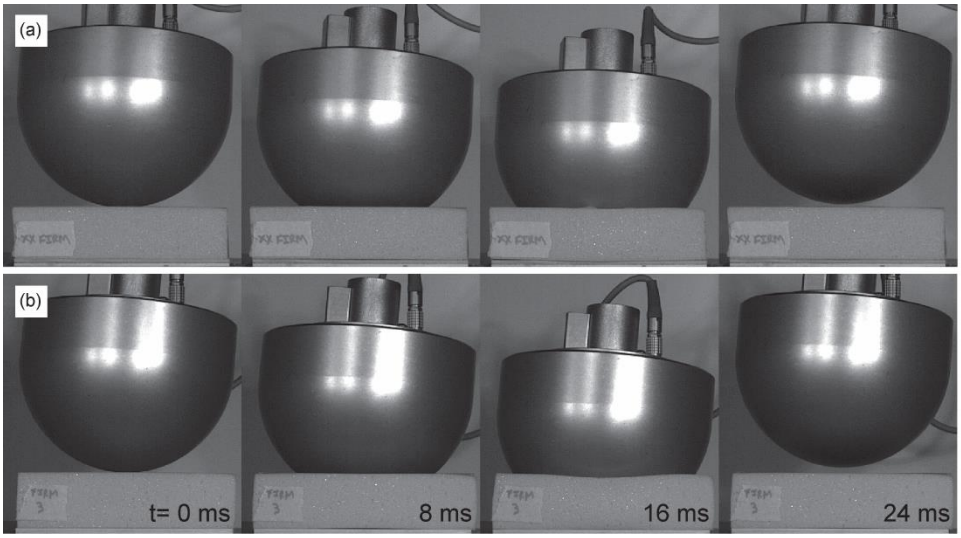

Figure 5.11: Image sequence showing the impact and rebound process for (a) XX firm and (b) Firm foams at equivalent time intervals.

Chapter 6

Conclusions and future work

6.1 Summary of work and conclusions

A binary representation of the constituent phases has proven to be useful for modeling the composite response of cross-ply Dyneema® HB26 composites, especially under loading conditions that elicit the off-axis response. Specifically, an analytical model for the ±45° tensile response of the composite based on the binary representation has been developed and found to be in excellent agreement with the predictions of corresponding finite element simulations. Furthermore, following a straightforward calibration of the elastic/plastic properties of the effective medium, both sets of predictions agree well with the experimental measurements. One key conclusion drawn from this part of the study is that the strain-state of the composite is controlled largely by the rotation of essentially inextensible fibers. In turn, this rotation governs the macroscopic hardening of the composite and its tensile strain limit. Although the model adequately predicts the measured stresses and out-of-plane strains over much of the loading history, it overestimates the stresses at the highest strains. These discrepancies are likely

due to microstructural damage. One area of future research lies in the development of experiments to illuminate the mechanisms for the observed softening behavior and in the implementation of an appropriate damage model.

The results of the quasi-static finite element simulations of the quasi-static punch response of clamped plates of these composites based on the same binary model also agree well with experimental measurements. The simulations begin to break down only once the shear sliding stress at the interface between the plate and the clamps exceeds the interlaminar shear strength of the composite. In this case, since the model assumes purely frictional sliding without interlaminar deformation or damage, pull-in of the composite plate past the clamp surfaces is predicted to occur at a higher shear stress relative to that obtained experimentally. The model works similarly well for predicting the dynamic response of clamped plates subject to impact by foam projectiles. Both the back-face deflection-time history and the final plate profile (especially the changes caused by fiber pull-in) are captured with remarkable accuracy. Discrepancies arise once the contact area between the plates and the clamps begins to diminish and the plate deformation begins to exhibit some asymmetry. Since the present version of the model used in the numerical simulations is based on one-quarter of the entire plate with symmetry boundary conditions imposed, the model cannot predict the real (asymmetric) plate response in this domain. Some additional refinements to the model could be made by characterizing more rigorously the strain rate-sensitivity of the matrix response.

An analytical framework has been developed to assess the efficacy of crushable foams in mitigating risk of serious head injury. The model predicts that the contact area grows approximately linearly with penetration distance, resulting in accelerations that vary sinusoidally with time. The model also predicts that the acceleration will drop precipitously from the peak to zero. The model underestimates the HIC values of the three Divinycell® foams tested in this study, attributed to the elasticity of the foams and the resulting rebound of the headform, but is still accurate to within 10%. The time scale associated with rebound within the HIC interval has been characterized by a non-dimensional time parameter. It increases with increasing foam density, which was found to be consistent with the trend of increasing errors in predicted HIC values. Finite element simulations, where the elasticity had been naturally incorporated, provided marginal improvements on the predictions of the HIC. Thus, the errors associated with the rigid-plastic approximation of the foam response in the analytical model are insignificant.

An analytical framework has been presented to predict the reduction in HIC that is attainable by adhering stiff composite plates to viscoelastic crushable foams. The model predicts that the shape of the acceleration-time history is transformed from sinusoidal to square in shape, with reductions of up to 46% in the HIC. Experimental results have shown that, for the viscoelastic foams (SunMate®) tested in this study, significant reductions in the HIC are indeed obtained by adhering a stiff composite plate on top of the foams. The model predicts the HIC to within 10% for both the composite plate-foam systems and the foams alone, provided that the headform is

brought to arrest prior to densification in the foam. One of the key conclusions from this work stems from the design maps produced by the analytical models. That is, for any given foam strength, foam thickness, and impact velocity, the HIC can always be reduced by adhering a plate to the foam. Furthermore, the plate geometry can be used to tailor the magnitude of the reduction in HIC, and can also be used to increase the maximum impact velocity that prevents densification in the foam. Additional refinements to the model could be made by incorporating the effects elasticity and rate-sensitivity in the foam response, as well as the elastic bending in the plates. As an important note, one must consider the consequences of approaching limits that yield unrealistic outcomes. For instance, if the plate area approaches excessively small values, the forces exerted on the headform approach that of a point-load, and this can have highly undesirable consequences. Additionally, the model predicts that reductions in the HIC can be achieved by increasing the area of the plate to an infinitely large value and coupling that plate with a foam with an infinitesimally low strength, which is an unrealistic scenario. The analytical models presented in this study are merely *guidelines*, and should be used as such.

Select experiments have been conducted to assess the predictive capability of the analytical model and the benefits of the plate-foam design. However, the design space, for the most part, remains uncharted. Perhaps one of the most interesting results of this body of work is the performance of the SunMate® T50E foams. The observed reduction in the HIC, when compared to the other foams in this study, is remarkable. The significant reduction in the HIC has been attributed to the strain-softening after yield.

This result, coupled with the observed damage in both the Dyneema® and CFRP plates, serves as motivation for future research in other composite material systems. Structural geometries could be devised to strain-soften at a prescribed rate to produce a similar "top-hat" shape to the acceleration-time history. As a result, such systems would achieve further reductions in the value of the HIC.

Appendix A

Elastic properties of $\pm 45°$ laminates

The elastic response of a balanced symmetric angle ply laminate under plane stress conditions is given by:

$$\begin{bmatrix}\sigma_{xx}\\ \sigma_{yy}\\ \tau_{xy}\end{bmatrix} = \begin{bmatrix}\overline{Q}_{11} & \overline{Q}_{12} & 0\\ \overline{Q}_{12} & \overline{Q}_{11} & 0\\ 0 & 0 & \overline{Q}_{66}\end{bmatrix} \cdot \begin{bmatrix}\varepsilon_{xx}\\ \varepsilon_{yy}\\ \gamma_{xy}\end{bmatrix} \tag{A1}$$

where $\bar{Q}_{ij}$ are the components of the reduced transformed stiffness matrix for the individual laminae. In general, the latter are:

$$\overline{Q}_{11} = Q_{11} \cdot m^4 + Q_{22} \cdot n^4 + (2Q_{12} + 4Q_{66}) \cdot m^2 n^2 \tag{A2a}$$

$$\overline{Q}_{22} = Q_{11} \cdot n^4 + Q_{22} \cdot m^4 + (2Q_{12} + 4Q_{66}) \cdot m^2 n^2 \tag{A2b}$$

$$\overline{Q}_{12} = Q_{12} \cdot (m^4 + n^4) + (Q_{11} + Q_{22} - 4Q_{66}) \cdot m^2 n^2 \tag{A2c}$$

$$\overline{Q}_{66} = (Q_{11} + Q_{22} - 2Q_{12} - 2Q_{66}) \cdot m^2 n^2 + Q_{66} \cdot (m^4 + n^4) \tag{A2d}$$

where the Q_{ij} terms (without the over-bar) represent the reduced stiffness matrix of an individual lamina (in the coordinate system defined by the fibers, under conditions of plane stress), $m = \cos\theta$ and $n = \sin(\theta)$. For a $[\pm 45°]$ laminate, $m = n = \frac{\sqrt{2}}{2}$. The Q_{ij} terms can be expressed in terms of the engineering elastic constants of the lamina as:

$$Q_{11} = \frac{E_1}{(1-v_{12}{}^2 \mathrm{E}_2/E_1)} \tag{A3a}$$

$$Q_{12} = \frac{v_{12}E_2}{(1-v_{12}{}^2 \mathrm{E}_2/E_1)} \tag{A3b}$$

$$Q_{22} = \frac{E_2}{(1-v_{12}{}^2 \mathrm{E}_2/E_1)} \tag{A3c}$$

$$Q_{66} = G_{12} \tag{A3d}$$

where v_{12} is the in-plane Poisson's ratios and G_{12} is the in-plane shear modulus. Combining (A2) with (A3), $\overline{Q}_{ij}$ becomes:

$$\overline{Q}_{11} = \overline{Q}_{22} = \frac{1}{4}\left[\frac{E_1+(1+2v_{12})\cdot E_2}{1-v_{12}^2\cdot\frac{E_2}{E_1}} + 4G_{12}\right] \tag{A4a}$$

$$\overline{Q}_{12} = \frac{1}{4}\left[\frac{E_1+(1+2v_{12})\cdot E_2}{1-v_{12}^2\cdot\frac{E_2}{E_1}} - 4G_{12}\right] \tag{A4b}$$

$$\overline{Q}_{66} = \frac{1}{4}\left[\frac{E_2(1-v_{12})}{1-v_{12}^2\cdot\frac{E_2}{E_1}} + 2G_{12}\right] \tag{A4c}$$

In the present binary representation of the composite, $G_{12} = G = \frac{E_{em}}{2(1+v)}$, $v_{12} = v$ and E_1 and E_2 are given by (2a) and (2b) in the text. Combining these results with (A4a) yields:

$$\overline{Q}_{11} = \overline{Q}_{22} = \left[\frac{V_f E_f + E_m + (1+2v)\cdot E_{em}}{4\left(1-v^2\cdot\left(\frac{E_{em}}{E_{em}+V_f E_f}\right)\right)} + \frac{E_{em}}{2(1+v)}\right] \tag{A5}$$

Making the assumption that $E_f \gg E_m$, (A5) simplifies to:

$$\overline{Q}_{11} = \overline{Q}_{22} \approx \frac{V_f E_f}{4} + \frac{E_m}{2}\cdot\left[\frac{1}{(1+v)} + (1+v)\right] \tag{A6}$$

Similarly, from (A4b):

$$\overline{Q}_{12} = \frac{V_f E_f}{4} + \frac{E_m}{2} \cdot \left[\frac{2v+v^2}{(1+v)}\right] \tag{A7}$$

Inverting (A1), the strains are expressed in terms of the stresses via:

$$\begin{bmatrix}\varepsilon_{xx}\\ \varepsilon_{yy}\\ \gamma_{xy}\end{bmatrix} = \begin{bmatrix}\frac{\overline{Q}_{11}}{\overline{Q}_{11}^2-\overline{Q}_{12}^2} & -\frac{\overline{Q}_{12}}{\overline{Q}_{11}^2-\overline{Q}_{12}^2} & 0\\ -\frac{\overline{Q}_{12}}{\overline{Q}_{11}^2-\overline{Q}_{12}^2} & \frac{\overline{Q}_{11}}{\overline{Q}_{11}^2-\overline{Q}_{12}^2} & 0\\ 0 & 0 & \overline{Q}_{66}^{-1}\end{bmatrix} \cdot \begin{bmatrix}\sigma_{xx}\\ \sigma_{yy}\\ \tau_{xy}\end{bmatrix} \tag{A8}$$

The tensile modulus of the laminate is thus given by

$$E_x = \frac{\overline{Q}_{11}^2-\overline{Q}_{12}^2}{\overline{Q}_{11}} \tag{A9}$$

which, combined with (A6) and (A7), yields (2.3) in the text.

References

[1] Cunniff PM. Dimensionless parameters for optimization of textile-based body armor systems. Proc 18th Int Symp Ballist 1999.

[2] Phoenix LS, Porwal PK. A new membrane model for the ballistic impact response and V50 performance of multi-ply fibrous systems. Int J Solids Struct 2003;40:6723–65.

[3] O'Masta MR, Deshpande VS, Wadley HNG. Mechanisms of Projectile Penetration in Dyneema® Encapsulated Aluminum Structures. Int J Impact Eng 2014.

[4] Tan L Bin, Tse KM, Lee HP, Tan VBC, Lim SP. Performance of an advanced combat helmet with different interior cushioning systems in ballistic impact: Experiments and finite element simulations. Int J Impact Eng 2012;50:99–112.

[5] Kulkarni SG, Gao X-L, Horner SE, Zheng JQ, David NV. Ballistic helmets – Their design, materials, and performance against traumatic brain injury. Compos Struct 2013;101:313–31.

[6] Zhang L, Makwana R, Sharma S. Brain response to primary blast wave using validated finite element models of human head and advanced combat helmet. Front Neurol 2013;4:88.

[7] Zhang L, Gurao M, Yang KH, King AI. Material characterization and computer model simulation of low density polyurethane foam used in a rodent traumatic brain injury model. J Neurosci Methods 2011;198:93–8.

[8] Forero Rueda M a., Cui L, Gilchrist MD. Optimisation of energy absorbing liner for equestrian helmets. Part I: Layered foam liner. Mater Des 2009;30:3405–13.

[9] Hansen K, Dau N, Feist F, Deck C, Willinger R, Madey SM, et al. Angular Impact Mitigation system for bicycle helmets to reduce head acceleration and risk of traumatic brain injury. Accid Anal Prev 2013;59:109–17.

[10] Gurdjian ES, Lissner HR, Latimerr FR, Haddad BF, Webster JE. Quantitative determination of acceleration and intercranial pressure in experimental head injury. Neurology 1983;3:417–23.

[11] Gadd CW. Use of a weighted-impulse criterion for estimating injury hazard. Proc. 10th Stapp Car Crash Conf., New York: Society of Automotive Engineers; 1966, p. 164–74.

[12] Gurdjian ES, Roberts VL, Thomas LM. Tolerance curves of acceleration and intracranial pressure protective index in experimental head injury. J Trauma 1966;6:600–4.

[13] Versace J. A review of the severity index. Proc. 15th Stapp Car Crash Conf., 1971, p. SAE Paper 710881.

[14] Eiband AM. Human tolerance to rapidly applied accelerations: a summary of the literature. NASA Memo 5-19-59E 1959.

[15] Gennarelli TA, Wodzin E. The Abbreviated Injury Scale. Barrington, IL: Association for the Advancement of Automotive Medicine; 2005.

[16] Mackay M. The increasing importance of the biomechanics of impact trauma. Sadhana 2007;32:397–408.

[17] U.S. Department of Transportation. Federal Motor Vehicle Safety Standards, Standard 208 n.d.

[18] Naunheim RS, Standeven J, Richter C, Lewis LM. Comparison of impact data in hockey, football, and soccer. J Trauma 2000;48:938–41.

[19] Greenwald RM, Gwin JT, Chu JJ, Crisco JJ. Head impact severity measures for evaluating mild traumatic brain injury risk exposure. Neurosurgery 2008;62:789–98.

[20] Lewis LM, Naunheim RS, Standeven J, Naunheim KS. Quantitation of impact attenuation of different playground surfaces under various environmental conditions using a tri-axial accelerometer. J Trauma 1993;35:932–5.

[21] ASTM Standard F1292, Standard Specification for Impact Attenuation of Surfacing Materials within the Use Zone of Playground Equipment. ASTM Int West Conshohocken, PA 2009.

[22] Shields B, Smith GA. The potential for brain injury on selected surfaces used by cheerleaders. J Athl Train 2009;44:595–602.

[23] Zok FW, Nazarian O, Begley MR. Selective protective materials for mitigating head injury during blunt impact. Submitt to J Impact Eng 2013.

[24] Begley MR, Zok FW. Optimal Material Properties for Mitigating Brain Injury During Head Impact. J Appl Mech 2013;81:131014–131014–5.

[25] Russell BP, Kandan K, Deshpande VS, Fleck NA. The high strain rate response of UHMWPE: from fibre to laminate. Submitt to Int J Impact Eng 2012.

[26] Karthikeyan K, Russell BP, Fleck NA, Deshpande VS, Wadley HNG. The effect of shear strength on the ballistic response of laminated composite plates. Submitt to Eur J Mech A/Solids 2013.

[27] Karthikeyan K, Russell B, Fleck N. The soft impact response of composite laminate beams. Int J Impact Eng 2013;In Press.

[28] ASTM Standard D638 2003. Standard test method for tensile properties of plastics. ASTM Int West Conshohocken, PA 2008.

[29] Rajan VP, Rossol MN, Zok FW. Optimization of Digital Image Correlation for High-Resolution Strain Mapping of Ceramic Composites. Exp Mech 2012;52:1407–21.

[30] Flores S, Evans AG, Zok FW, Genet M, Cox B, Marshall D, et al. Treating matrix nonlinearity in the binary model formulation for 3D ceramic composite structures. Compos Part A Appl Sci Manuf 2010;41:222–9.

[31] Hearle JWS. High-performance fibres. Woodhead Publishing Limited; 2001.

[32] Abaqus FEA, ABAQUS Analysis User's Manual. Pawtucket, RI: 2012.

[33] Nazarian O, Zok FW. Constitutive Model for the Shear Response of Dyneema ® Fiber Composites. 2013.

[34] Radford D, Deshpande V, Fleck N. The use of metal foam projectiles to simulate shock loading on a structure. Int J Impact Eng 2005;31:1152–71.

[35] Gibson LJ, Ashby MF. Cellular Solids: Structure and Properties. 2nd ed. Cambridge, UK: Cambridge University Press; 1997.

[36] Zhang L, Yang KH, King AI. A Proposed Injury Threshold for Mild Traumatic Brain Injury. J Biomech Eng 2004;126:226.

[37] Sabet A a, Christoforou E, Zatlin B, Genin GM, Bayly P V. Deformation of the human brain induced by mild angular head acceleration. J Biomech 2008;41:307–15.

[38] Feng Y, Okamoto RJ, Namani R, Genin GM, Bayly P V. Measurements of mechanical anisotropy in brain tissue and implications for transversely isotropic material models of white matter. J Mech Behav Biomed Mater 2013;23:117–32.

[39] Moss WC, King MJ. Impact response of US Army and National Football League helmet pad systems 2011.

[40] Tagarielli VL, Deshpande VS, Fleck NA. The high strain rate response of PVC foams and end-grain balsa wood. Compos Part B Eng 2008;39:83–91.

[41] Hutchinson TP. Dependence of the head injury criterion and maximum acceleration on headform mass and initial velocity in tests simulating pedestrian impacts with vehicles. J Biomed Eng 2013;135:114508–114508–4.